

7-2-2011

Integration of composite nanomaterials into anode and cathode designs

Claudia Wuillma Narvez Villarrubia

Follow this and additional works at: https://digitalrepository.unm.edu/cbe_etds

Recommended Citation

Narvez Villarrubia, Claudia Wuillma. "Integration of composite nanomaterials into anode and cathode designs." (2011).
https://digitalrepository.unm.edu/cbe_etds/52

This Thesis is brought to you for free and open access by the Engineering ETDs at UNM Digital Repository. It has been accepted for inclusion in Chemical and Biological Engineering ETDs by an authorized administrator of UNM Digital Repository. For more information, please contact disc@unm.edu.

Claudia Wuillma Narváez Villarrubia
Candidate


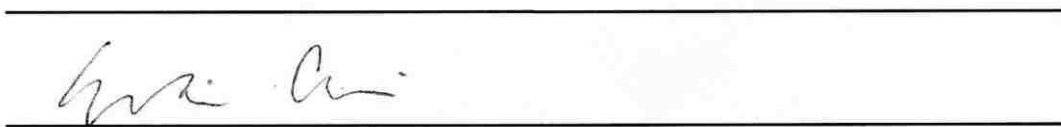
Chemical and Nuclear Engineering
Department

This thesis is approved, and it is acceptable in quality
and form for publication:

Approved by the Thesis Committee:



, Chairperson



**INTEGRATION OF COMPOSITE NANOMATERIALS INTO
ANODE AND CATHODE DESIGNS**

by

CLAUDIA WUILLMA NARVAEZ VILLARRUBIA

**B.S. CHEMICAL ENGINEERING, UNIVERSITY OF NEW
MEXICO, 2009**

THESIS

Submitted in Partial Fulfillment of the
Requirements for the Degree of

Master of Science in Chemical Engineering

The University of New Mexico
Albuquerque, New Mexico

May, 2011

DEDICATION

This work is dedicated to the memory of my dear father, Miguel Narváez, for his encouragement and his words of wisdom “knowledge does not take place but is the only think is going to take you far and help you to help others”. This is also for my mother who has been the most caring and giving person I ever met and the women I admire the most. I dedicate this work to my little brother as well, he is a life warrior because the FOP never defeated him; he never gives up. He is the person from whom I wish to learn to never give up.

ACKNOWLEDGMENTS

I greatly acknowledge Plamen Atanassov, my advisor, for the support he gave me during these years and for giving me the opportunity to work in research.

I would like to thank my committee members, Dr. Carolin Lau and Dr. Eva Chi for their valuable recommendations in the development of this thesis paper. My gratitude is extended to the AFOSR MURI Program in Fundamentals and Bioengineering of Enzymatic Fuel Cells for the funding to pursue this research.

I'm very grateful for the collaboration of Dr. Virginia Davis in the creation of the bucky papers used in my research on the anode design.

I would like to thank to Rosalba Rincón and Akinbayowa Falase for helping me in the lab, for editing my papers and for, the most valuable for me, their friendship. Also, thanks to Jared Roy for making my days in the office more enjoyable. Thanks to Tim Olson, his help in the lab was very valuable for me when I was beginning in working in the lab.

To my editor, my brother Moises Narváez, I do thank him from the bottom of my heart for the time he invested in this work. I thank my brothers and sister, who gave me immeasurable support over the years. I greatly appreciate their love, their encouragement and support.

**INTEGRATION OF COMPOSITE NANOMATERIALS INTO
ANODE AND CATHODE DESIGNS**

by

CLAUDIA WUILLMA NARVAEZ VILLARRUBIA

ABSTRACT OF THESIS

Submitted in Partial Fulfillment of the
Requirements for the Degree of

Master of Science in Chemical Engineering

The University of New Mexico
Albuquerque, New Mexico

May, 2011

Integration of Composite Nanomaterials into Anode and Cathode Designs

by

Claudia Wuillma Narváez Villarrubia

B.S., Chemical Engineering, University of New Mexico, 2009.

ABSTRACT

The relevance of this research lays on the need to develop biofuel cell for portable and implantable devices. To accomplish this, the enzymatic oxidative cascade of reactions for the degradation of carbohydrates observed in the Krebs cycle should be mimicked on the anode. In addition, the oxygen reduction reaction observed in some fungi, plants and bacteria should be mimicked on the cathode. As a consequence, optimum electrodes must be developed to satisfy several competing criteria: high electrical conductivity, significant attractive interactions with enzymes, high surface to volume ratio, and sufficiently large pore size to facilitate mass transport.

The research described in this manuscript introduces the use of “bucky” papers based on SWNTs as anode electrode materials for the oxidation of NADH and L-Malate oxidation. Additionally, it introduces MWNTs-based “buckeye” paper and teflonized carbon-based “toray” papers for the oxygen reduction reaction.

This manuscript introduces the development of an anode that accomplishes satisfactorily one of the steps in the cascade of the Krebs cycle, the oxidation of L-Malate by the NADH-dependent malate dehydrogenase enzyme, making use of composite carbon nanomaterials, the “bucky” papers. SWNTs were used to create an electrode design consisting of high surface area-hierarchically ordered carbon nanomaterials with

controlled surface chemistry. The “bucky” papers were specifically designed for and employed in this research with the objective to overcome the NADH reaction kinetics and NADH/malate dehydrogenase interaction barriers using an electrodeposited mediator, methylene green, on the anode surface. The components of the BP11 and BPMG (SWNTs, IPA and SWNTs, IPA and MG respectively) anode electrodes are well combined to give a conductive-hydrophilic-porous-manageable material for a cavity anode design. The incorporation of methylene green into the material opens the door for improvement and would simplify the manufacturing process of the cavity anode material based in SWNTs.

This research introduces new cathodes designs based on buckeye and toray papers for air-breathing and liquid electrolyte modes. Buckeye and 0.11mm-thick toray papers are used to design the air-breathing cathode by immobilization of Laccase using a non-covalent linking agent. The air-breathing layer shows to satisfactorily allow oxygen mass transport to feed the cell. In the second part of the part of the research, the liquid electrolyte cathode, designed to be applied in implantable devices, consists of 0.28 mm-thick toray paper as conductive material and Bilirubin oxidase, the biocatalyst, immobilized silica-gel. The liquid electrolyte cathode shows good performance for about 10 days in physiological conditions due to stabilization of the enzyme.

This research opens the possibilities to optimize electrode designs based on carbon composite nanomaterials, and enzyme loading and stabilization. The composite nanomaterials and the immobilization techniques utilized in this research would help as departing stage to engineer electrodes designs that meet the criteria required for optimum biofuel cells.

Table of Contents

LIST OF FIGURES	x
LIST OF TABLES	xiii
CHAPTER 1. BIOFUEL CELLS	1
1.1. Types of Bifuel Cells	2
1.2. Principles of Fuel Cell - Performance.....	4
1.3. Principles of Enzymatic Biofuel Cells.....	11
1.3.1 Enzymatic Biofuel Cell Performance	11
1.3.2 Anode Design Precedents	16
1.3.3 Cathode Design Precedents	23
CHAPTER 2. EXPERIMENTS AND METHODS FOR ELECTRODES INTEGRATION	31
2.1. Enzyme Immobilization Techniques	31
2.2. Integration of Composite Nanomaterials for Anode and Cathode Design	35
2.2.1. SWNTs- Integration for Anode Design	35
2.2.2. MWNTs and Teflonized Carbon Fibers Integration for Cathode Design.....	39
2.3. Physical and Electrochemical Characterization Techniques	40
2.3.1. Electrochemical Techniques for Electrode Characterization.....	40
2.3.2. Physical Surface Characterization Techniques	46
CHAPTER 3. SWNTS-BASED ‘BUCKY’ PAPERS INTEGRATED TO ANODE DESIGN	48
3.1. Experimental and Methods for Anode Characterization	49
3.2. Results and Discussion	64

3.3. Conclusion on the Anode Design Performance	68
CHAPTER 4. MWNTS-BASED “BUCKEYE” PAPER AND TEFLONIZED CARBON FIBER- BASED “TORAY” PAPERS INTEGRATED FOR CATHODE DESIGNS.....	70
4.1. Buckeye and Toray Papers Integration for an Air-Breathing Cathode Design	72
4.1.1. Experiments and Methods for Air-Breathing Cathode Characterization.....	73
4.1.2. Results and Discussion	81
4.1.3. Conclusion for the Air-Breathing Cathode.....	84
4.2. Toray Paper Integration for a Liquid Electrolyte Cathode Design	86
4.2.1. Experimental and Methods to Evaluate the Liquid Electrolyte Cathode.....	86
4.2.2. Results and Discussion of the Performance of the Liquid Electrolytic Cathode	92
4.2.3. Conclusion on the Performance of the Liquid Electrolyte Cathode Performance	96
CHAPTER 5. CONCLUSIONS ON THE INDEPENDENT TESTED ANODE AND CATHODES	98
5.1 Bucky Paper-Based Anode Design for the Oxidation of NADH catalyzed by PMG and the L-Malate catalyzed by MDH.....	98
5.2. Multicopper Oxidases- based Cathodes for the O ₂ Reduction to H ₂ O.	100
5.2.1 Buckeye and Toray Paper- Based Air-Breathing Cathodes for ORR catalyzed by Laccase	100
5.2.2. Toray Paper-Based Cathode for ORR Catalyzed by Bilirubin Oxidase	101
REFERENCES	104

List of Figures

Figure 1.1 Enzymatic biofuel cells that use methanol as fuel.....	1
Figure 1.2 Graph of the performance of ideal and actual fuel cell voltage/ current	7
Figure 1.3 Plot of the Tafel equation representing the current on a logarithmic scale in function of its overpotential η and $\beta = 0.5$	8
Figure 1.4 Mechanisms of electron-transfer. (a) Direct electron transfer (tunneling mechanism) from electrode surface to the active site of an enzyme. (b) Electron transfer via redox mediator.....	13
Figure 1.5 Polarization curves depict typical current performances for direct and mediated electron transfer in biofuel cell electrodes for different enzymes.....	14
Figure 1.6 Glucose oxidase tridimensional structure-The flavin type active site (FAD is a cofactor attached to the protein structure) is deep within the shell, far from the protein surface.....	14
Figure 1.7 Three groups of enzymes based on location of enzyme active centre.....	16
Figure 1.8 Krebs Cycle, also called Citric Cycle is methabolic path way for the complete oxidation of pyruvate – The NADH/NAD ⁺ dependent Malate Dehydrogenase enzyme is the last step of the cycle.....	18
Figure 1.9 Malate Dehydrogenase Structure.....	19
Figure 1.10 NAD ⁺ reduction reaction to NADH.....	19
Figure 1.11 Potential of redox couples for dehydrogenase enzymes where NADH/NAD ⁺ is shown to have a potential of -0.584 V at pH 8l.....	20
Figure 1.12 Laccase from <i>Trametes versicolor</i>	25
Figure 1.13 Multicopper Cluster Center- Oxygen Interaction.....	26
Figure 1.14 Multicopper Cluster Center- Oxygen Conformation.....	27
Figure 1.15 a) Laccase-electrode surface interaction, b) Intramolecular electron transfer in Laccase.....	28

Figure 1.16 Activity of native and modified Laccase with oxygen.....	30
Figure 2.1 PBSE interaction with MWNTs surface.....	33
Figure 2.2. Schematic structure of a graphene sheet. The two basis vectors a_1 and a_2 are shown.....	37
Figure 2.3 a) Armchair, b) zigzag, c) chiral configurations in a SWNT.....	37
Figure 2.4 a) Plot of potential vs. time showing a triangular waveform in a CV, b) Cyclic Voltammogram for a reversible redox reaction	42
Figure 2.5 a) Stepped potential in chronoamperometry, b) Faradic current and exponential decay of current as a function of time	43
Figure 2.6 a) Potentiostatic Polarization Curve, working potential of the electrode is found when current approaches steady state behavior, b) Chronoamperometric curve, current vs. time, at a constant potential, the change in current measured is due to the change of the concentration of the reactant in the cell by aliquots added.....	44
Figure 2.7 a) Chronopotentiometric curve, potential as a function of time at a constant applied current, b) Red and Ox species concentration with respect to the distance to the working electrode surface.....	45
Figure 3.1 SEM Images of 1-a) & 1-b) BP11 (SWNTs + IPA) and 2-a) & 2-b) BPMG (SWNTs + IPA + MG) before MG electrodeposition.....	55
Figure 3.2 Electrodeposition of MG at 5 mV/s between -0.35 to 1.3 V on a) BP11 (SWCNTs+IPA), b) BPMG (SWCNTs+IPA+MG). The peak shift indicates the polymerization reaction takes place.....	56
Figure 3.3 SEM images of surface electrodes after MG electrodeposition 1-a) & 1-b) BP11-MG and 2-a) & 2-b) BPMG-MG.....	57
Figure 3.4 EDS spectrum of the surface of BP11-MG Electrode.....	59
Figure 3.5 Hydrodynamic Polarization curves with Sodium Phosphate Buffer, NADH 1 mM and NADH 10 mM on a) BP11-MG Electrode , b) BPMG-MG Electrode and c) BPMG-MG RD Electrode at 1600 rpm.....	60-61
Figure 3.6 Relationship between Current generated and NADH Concentration (mM) on A) BP11-MG, B) BPMG-MG Electrodes found by Chronoamperometry with NADH on a) BP11-MG and b) BPMG-MG Electrodes. The 1 st Fick's Law behavior is observed.....	62

Figure 3.7 Relationship between Current generated and L-Malate Concentration (M) on A) BP11-MG (dashed line), B) BPMG-MG (solid line) Electrodes found by Chronoamperometry with MDH. Michaelis-Menten kinetics, there are neither inhibitors nor competitive processes.....	63
Figure 4.1. a) Air-breathing Cathode Design, b) Air-breathing Stack Cell.....	73
Figure 4.2. a) BEP without surface treatment, b) BEP treated with PBSE.....	74
Figure 4.3. BEP without farther treatment.....	75
Figure 4.4. BEP, PBSE and Laccase deposited on the surface forming a film.....	76
Figure 4.5. TP30/BEP setup for stack cell. BEP was previously treated with PBSE and Laccase was deposited overnight.....	76
Figure 4.6. Laccase immobilization on BEP, a) PBSE/BEP interaction, b) Curvature of the interacting surface , c) BEP SEM Image.....	77
Figure 4.7. TP30, 60% Teflonized Carbon Fiber, 0.11 mm Thickness. The porosity of the material allows for a three phase interface interaction.....	78
Open Circuit Voltage for a)Ni/XC50/BEP/PBSE/Laccase cathode, b) TP30/BE/PBSE/Laccase and TP90 (called just TP)/BEP/PBSE/Laccase cathodes (ON-Overnight, NO-No Oxygen was supplied to the cell, WO-With Oxygen supplied to the cell). In all cases, except blanks, PBSE was deposited for 1hr and Laccase was deposited overnight.....	79
Figure 4.9. Cyclic Voltammograms for a) Ni/XC50/BEP/PBSE/ Laccase, b) TP30/BEP/PBSE/Laccase and TP90 (called just TP)/BEP/PBSE/Laccase cathodes at a scan rate of 10mV/s in PB at pH 6. (ON-Overnight, NO-No Oxygen is supplied to the cell, WO-With Oxygen supplied to the cell). In all cases, except blanks, PBSE was deposited for 1hr and Laccase was deposited overnight although in some insets it was omitted.....	80
Figure 4.10. Potentiostatic Polarization Curves for a) Ni/XC50/BEP/PBSE/Laccase, b)TP30/BEP/PBSE/Laccase, and TP90 (called jus TP)/BEP/PBSE/Laccase cathodes (ON-Overnight, NO-No Oxygen was supplied to the cell, WO-With Oxygen supplied to the cell) In all cases, except blanks, PBSE was deposited for 1hr and Laccase was deposited overnight.....	81
Figure 4.11. SEM images of TP90, 60% teflonized carbon fiber “Toray” Paper, 0.28 mm Thickness.....	88

Figure 4.12. Chemical Vapor Deposition Chamber for silica-gel formation.....89

Figure 4.13. SEM images of TP90, after enzyme immobilization by Silica-gel entrapment with a time of exposure of the electrode to the precursor (TMOS) of about 10 min at room temperature (~25°C). Silica-gel forms a porous film on the TP90 surface allowing enzyme, electrolytic solution, electrode interaction.....90

Figure 4.14. a) Potentiostatic Polarization Curve for TP90/BOx/SilicaGel cathode, 0.14 NaCl, 0.1M PB pH 7.41, b) Stabilization Curve at 0V.....91

Figure 4.15. Galvanostatic Polarization Curve for TP90/BOx/SilicaGel cathode, 0.14 NaCl, 0.1M PB pH 7.41 (changed axis).....92

Tables

Table 3.1. . EDS data of the surface of BP11-MG electrode, composition of the elements deposited on the carbon SWNT electrode.....58

Table 3.2. . Michaelis-Menten parameters found by chronoamperometry of L-Malate with MDH.....63

Chapter 1. Biofuel Cells

Biofuel cells are power source devices that harvest electric energy generated from the oxidoreduction reactions of organic compounds [1-3]. Biofuel cells and conventional fuel cells work mostly through the same principles. Fuel is oxidized in the anode of the cell releasing electrons toward the cathode through an external circuit while generating electrical energy; simultaneously, protons traverse the electrolyte towards the cathode due to a proton driving force. Electrons from the external circuit combine with oxygen and protons at the cathode surface to produce water (Figure 1). Despite the similarities with conventional fuel cells, biofuel cells employ biological components such as enzymes, microbes and mitochondria as biocatalysts on the electrode surface. Although biofuel cells are called organelle or microbial, the actual catalysts are enzymes; enzymes are located within microbes for microbial biofuel cells, and enzymes are located within mitochondria in mitochondrial biofuel cells. When purified, enzymes are used directly on the electrode, then the biofuel cell is called enzymatic biofuel cell. These power devices emerge as a response to the demand of electrical power devices that can operate in near- neutral pH, physiological condition, and ambient conditions where conventional fuel cells fail. These devices are viewed as potential green technology.

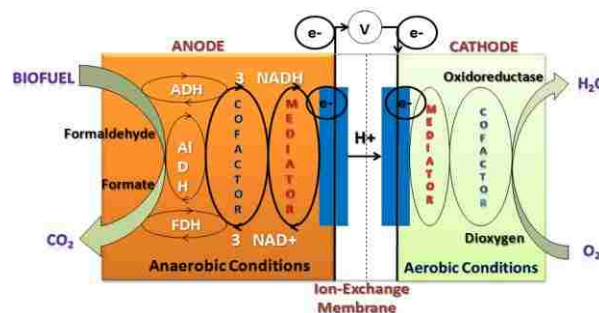


Figure 1.1. Enzymatic Biofuel Cell that use methanol as fuel, Wilkinson

In this research, we endeavor to the optimization of the enzyme-based catalytic layer of the electrodes by integration composite materials. These materials are papers based on SWNTs, MWNTs and Teflonized-Carbon Fibers. The composite nanomaterials have chemical stability and have high surface area to volume ratios that would improve enzyme loading, immobilization and enzyme-electrode interaction.

1.1. Types of Biofuel Cells

Microbial fuel cells are devices capable of catalyzing complete oxidation of organic fuels such as sugars, fatty acids and alcohols. These have higher efficiency in reaction and long lifetimes compared to enzymatic or mitochondrial biofuel cells. Unfortunately, microbial biofuel cells suffer from slow mass transport of the fuel across cellular membranes and low electron/electrode surface interaction due to a biofilm formation, which decreases the total energy density. Microbial fuel cells are used mostly for wastewater treatment while generating electric energy. These electrodes could be very large, yet generate small current and power densities. For example, microbial biofuel cells based on *Shewanella oneidensis* would reduce metals in the anode by transferring electrons to insoluble metals such as Fe^{3+} , Mn^{3+} and Mn^{4+} that work as terminal electron acceptors for the microbe's respiratory pathways [4]. However, due to the different physiological conditions in which bacteria grow, the limitations vary; these depend on the pH of the solution and temperature, among other growth factors. These factors can contribute to low current and power densities of the device.

Minteer et al., has recently developed a mitochondrial biofuel cell that can completely oxidize pyruvate [5-7]. The mitochondria contain all of the enzymes needed

for the oxidation of pyruvate since the entire Krebs cycle, oxidation of pyruvate cycle, occurs within this organelle. Mitochondrial biofuel cell has shown better performance ($\sim 0.203 \text{ mW/cm}^2$) than microbial biofuel cell ($\sim 0.0010\text{--}0.09 \text{ mW/cm}^2$) [5] This is due to the lower fuel transport limitations compared to microbial fuel cells; the lack of a cell membrane in the mitochondrial biofuel cell allows for small diffusion lengths. Interaction between the electrode surface and organelles is improved due to a higher load of organelles or catalytic sites on the surface of the electrode. Mitochondria do not form biofilms that interfere in the electrode/active site interaction; this further increases the mitochondrial biofuel cell efficiency when compared to the microbial. These characteristics help to increase the current and power densities of these devices compared to microbial fuel cells.

Enzymatic biofuel cells usually offer high current and power densities by employing purified enzymes [1-3]. These cells can be employed in nano-microelectronic or portable power sources, biosensors and implantable medical power devices. The high selectivity of enzymes, which make them able to avoid carbon dioxide poisoning (possible with metal catalysts), and their high efficiency in reaction with their substrates make the enzymes highly desirable to be used for biofuel cells. However, enzymatic biofuel cells suffer from limitations due to incomplete fuel oxidation of the biofuel and short lifetimes due to low enzyme stability. Synthesized in the mitochondria, enzymes are proteins that have high catalytic activity toward organic chemical reactions in living organisms. They lower the activation energy of the reaction and accelerate the rate of reactions. As a consequence, the products formed by the reactions approach equilibrium faster than in a non-catalyzed reaction. In enzymatic biofuel cells, metabolic enzymes are

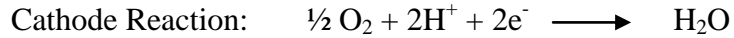
of interest for reproducing biological pathways such as the glycolysis and the Krebs cycle, where the electrons are extracted from an organic compound source into the anode and oxygen is the final electron acceptor in the cathode. The objective of enzymatic biofuel cell design is to recreate these processes by using enzyme-modified electrodes to similarly oxidize biofuels by following conventional fuel cell principles.

1.2. Principles of Fuel Cells -Performance

The cell operation and performance can be explained by a practical thermodynamics analysis relating the biofuel cell design and its performance variables. The understanding of the operation of a fuel cell defines its ideal performance. After the ideal performance of the biofuel cell has been determined, the losses of the cell can be calculated and deducted from the ideal performance to describe the real operation. As in conventional fuels cells, the real operation performance of the biofuel cell is subject to the conditions during operation [8].

The ideal performance of a conventional fuel cell depends on the electrochemical reactions that occur with different fuels and oxygen. In this way, low-temperature fuel cells, which work with hydrogen as the fuel, require noble metals working as electrocatalysts to lower the activation energy of the reactions and achieve practical reaction rates at the anode and cathode. High-temperature fuel cells however have relaxed requirements for catalysts and fuel sources.

As an example, in a Proton Exchange Membrane Cell in acid media, the anode and cathode reaction for hydrogen is as follows:



The Nernst equation defines the ideal performance of a fuel cell as the potential at zero current. The Nernst equation relates the maximum ideal potential ($E_{0, cell}$) of the cell and the equilibrium potential (E_{cell}) of reactants and products at non-standard temperatures and pressures. By knowing the ideal potential at standard conditions ($E^{\circ}_{0, cell}$), the ideal potential at other temperatures and pressures (E_{cell}) can be determined through the use of the equations below.

$$E_{cell} = E_{0, cell} + \frac{RT}{2F} \ln (P_{\text{H}_2} \cdot (P_{\text{O}_2})^{0.5}) \quad \text{Eq.1.1}$$

with

$$E_{0, cell} = E^{\circ}_{0, cell} - k(T - 298K) \quad \text{Eq.1.2}$$

here P is the gas pressure, R is the universal gas constant, T is the absolute temperature, F is Faraday's constant, E_{cell} is the equilibrium or reversible overall potential of the cell, and $E^{\circ}_{0, cell}$ is the potential at 1 atm and 298K or open circuit voltage.

The total Gibbs free energy change (ΔG) due to a change in potential is equal to $nFAE$. The change in Gibbs free energy due to changes in the potential for the cathodic and anodic reactions, for the example above H_2/O_2 , is:

$$\Delta G = \Delta G_o - RT \ln (P_{H_2} \cdot (P_{O_2}^{0.5})) \quad \text{Eq.1.3}$$

The maximum theoretical cell potential is known as the thermodynamic or reversible open circuit potential ($E_{o,cell}$), the open circuit voltage (OCV) or the electromotive force (EMF).

$$E_{o,cell} = \frac{-\Delta G_f}{nF} \quad \text{Eq.1.4}$$

Here, n is the number of electrons exchanged in the reaction and ΔG_f is the Gibbs free energy of formation of anodic and cathodic species. Following the example above, for the H_2/O_2 fuel cell, the ideal standard potential ($E^{\circ}_{o, cell}$) is 1.23 volts when the product is liquid water ($n=2$). The change in energy will represent the change of the potential force for the reaction of hydrogen and oxygen. The change in Gibbs free energy of the cell increases as the temperature decreases and the ideal potential of the cell is proportional to the change in the Gibbs free energy.

$$E_{o, cell} = EMF = \frac{-\Delta G_f}{2F} = 1.23 V (@298 K) \quad \text{Eq.1.5}$$

However, the ideal condition described so far does not demonstrate the behavior of an actual fuel cell; the standard Nernst potential ($E^{\circ}_{o,cell}$) refers to the ideal cell potential at standard conditions neglecting the losses at which a real fuel cell is subjected to.

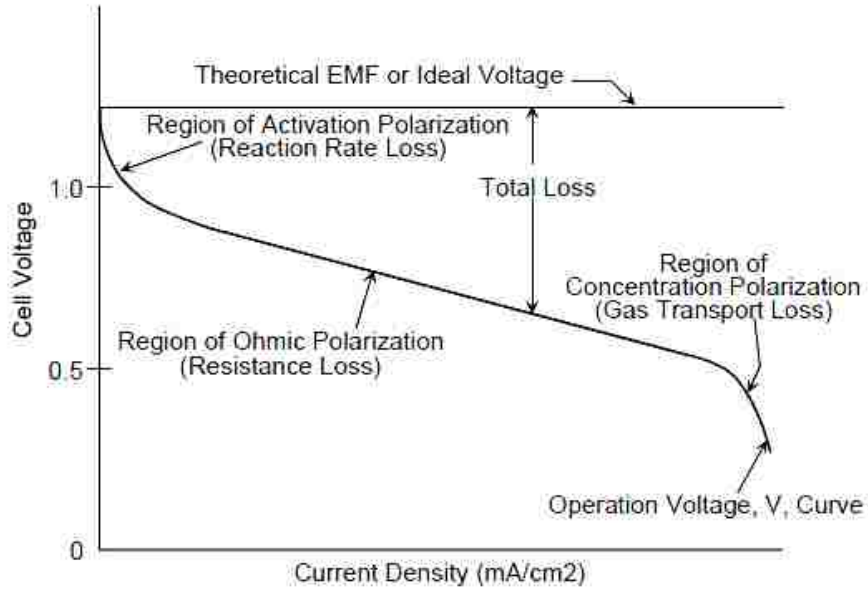


Figure 1.2. Graph of the performance of ideal and actual fuel cell voltage/ current

As the graph above shows, the actual cell potential is lower than its ideal equilibrium potential due to effects of irreversible losses. The losses produce a fuel cell voltage (V) that is lower than its ideal potential E_{cell} ($V = E_{cell}^{\circ} - Losses$). The losses, known as polarization overpotential or polarization overvoltage (η), are produced from three different sources and affect the cell performance at certain current densities regimes (represented in Figure 1.2). At low current densities, the activation or kinetic overpotentials (η_{act}) are observed due to slow rates of reaction or slow reaction kinetics taking place on the surface of the electrode. A portion of the potential generated is lost in driving the reaction. The activation overpotentials are described by the Tafel equation:

$$\eta_{act} = \beta \ln \left(\frac{i}{i_0} \right) \quad \text{Eq.1.6}$$

where i_0 is known as the exchange current density and corresponds to a dynamic equilibrium. This depends on the concentration of electroactive species and the free

energy of reaction at the rest potential with respect to reactants and products. Also, i is the overall current density (i_a+i_c) and β is the Tafel slope obtained by plotting the logarithmic form of the Tafel equation for the reactions in the cathode (a) and anode (b):

$$\ln(i_a) = \ln i_o + \left(\frac{(1-\beta)nF}{RT} \right) \eta \quad (a) \quad \ln(i_c) = \ln i_o + \left(\frac{n\beta F}{RT} \right) \eta \quad (b) \quad \text{Eq.1.7}$$

β is a constant of asymmetry parameter, this expresses the symmetry of the logarithmic current density curve with respect to the overpotential of the electrodes (Figure 1.3).

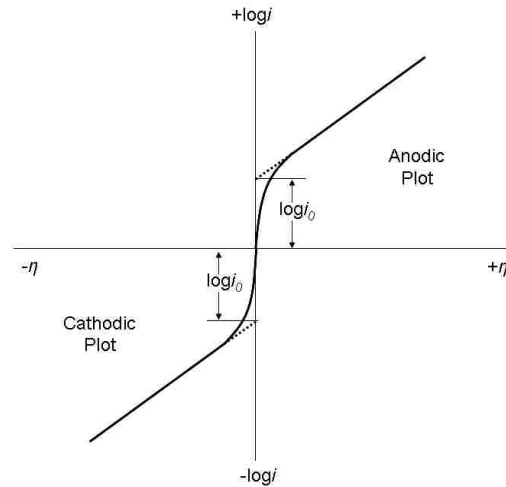


Figure 1.3. Plot of the Tafel equation representing the current on a logarithmic scale in function of its overpotential η and $\beta = 0.5$

For slow reactions, β has a high value describing a high drop of potential. This is a function of the temperature and the electrons transferred:

$$\beta = \frac{RT}{n\alpha F} \quad \text{Eq.1.8}$$

Here, α is the charge transfer coefficient, F is the Faraday constant, R is the ideal gas constant, T the absolute temperature and n is the number of electrons transferred in the oxidation of reduction reaction.

The ohmic or resistive overpotential (η_{ohm}) is observed at intermediate current densities because the electrolyte and the electrode material follow Ohm's law. The ohmic overpotential is linearly proportional to the current densities. The voltage drop is a consequence of electric resistance of the electrode materials and the flow of ions in the electrolyte solution.

$$\eta_{iR} = iR \quad \text{Eq.1.9}$$

where i is the electric current and R is the total resistance of the cell, which includes the electronic, ionic, and contact resistances. Decreasing the separation of the electrodes and enhancing the ionic conductivity of the electrolyte in solution help to decrease the ohmic losses.

At high current densities (Figure 1.2), the limiting factor is the concentration or mass transport overpotential (η_{conc}). The concentrations of the reactants decrease while the oxidoreduction reactions are taking place on the electrode surface. This produces the inability to maintain the sufficient concentration of the fuel close the electrode surface due to slow mass diffusion; the electrode starves. This could be due to the small pore size of the electrode material limiting the accessibility of the reactants to approach the reaction sites, or due to the slow diffusion of the reactants and products to or from the electrode surface or reaction site respectively through the electrolytes in solution.

Generally, the concentration overpotential is affected mostly by the diffusion of the reactants or products to or from the reaction sites. The concentration overpotential is defined as:

$$\eta_{conc} = \frac{RT}{nF} \ln \left(\frac{C_S}{C_B} \right) \quad \text{Eq.1.10}$$

where C_S is the surface concentration on the electrode and C_B is the bulk concentration. According to Fick's First Law and Faraday's Law, the equation above can be written as the Nernst equation:

$$\eta_{conc} = \frac{RT}{nF} \ln \left(\frac{i_{lim} - i}{i_{lim}} \right) \quad \text{Eq.1.11}$$

Where i_{lim} is the limiting current defined in terms of the diffusion coefficient. Rearranging (D), the Nernst diffusion layer (δ), and the bulk concentration (C_S), i_{lim} yields,

$$i_{lim} = nFD \left(\frac{C_S}{\delta} \right) \quad \text{Eq.1.12}$$

Then, the overall fuel cell potential turns to be:

$$\eta_{total} = \eta_{act} + \eta_R + \eta_{conc} \quad \text{Eq.1.14}$$

The activation and concentration overpotentials can exist at both cathode and anode electrodes in a fuel cell. These values can then be added for each electrode to give a total overpotential for the cathode, $\eta_{total,c}$, and a total overpotential for the anode, $\eta_{total,a}$.

$$\eta_{total, c} = \eta_{act, c} + \eta_{conc, c} \quad (a) \qquad \eta_{total, a} = \eta_{act, a} + \eta_{conc, a} \quad (b) \qquad \text{Eq.1.15}$$

These effects of polarization shift the potential of the electrode (E_c and E_a) to new values, V_c and V_a , for cathode and anode respectively:

$$V_c = E_c + \eta_{total, c} \quad (a) \qquad V_a = E_a + \eta_{total, a} \quad (b) \qquad \text{Eq.1.16}$$

Finally, for the overall cell, the cell voltage accounting for overpotential or losses is given by the following equation

$$V_{cell} = V_c - V_a - \eta_{iR} \qquad \text{Eq.1.17}$$

The power output of the fuel cell is then defined as the product of the current density and the overall fuel cell voltage as follows:

$$P = i \cdot V_{cell} \qquad \text{Eq.1.18}$$

1.3. Principles of Enzymatic Biofuel Cell

1.3.1. Enzymatic Biofuel Cell Performance

As stated for fuel cells, the power output of a biofuel cell is determined by the actual cell voltage and the current density of the biofuel cell [8]. For an enzymatic biofuel cell, the cell voltage is governed by the thermodynamic potentials of the enzymes at cathode and the anode, and the mechanism of electron transfer between the electrode

surface and the enzymes [2]. Similarly to conventional fuel cells, the oxidation of the biofuel is catalyzed in the anode and the reduction is catalyzed in the cathode but by action of oxidoreductases enzymes. The enzymes transfer the electrons of the oxidoreduction reactions by interacting with the electrode surface directly or by use of mediators.

Mechanisms of Electron Transfer

The mechanisms of electron transfer to and from the electrode to and from the active sites of the enzymes occur by a direct or mediated electron transfer mechanism [9]. Direct electron transfer requires that the distance of the active site of the enzyme and the surface of the electrode is short enough for electron tunneling (Figure 1.4.a). Here, the active site of the enzyme is close to the surface of the electrode, allowing for direct communication between active site and electrode surface. When the active site is within the enzyme, direct electron transfer is not possible. Exogenous mediators help to overcome this barrier. Mediators work shuttling the electrons from the surface of the electrode to the active site of the enzyme and vice versa (Figure 1.4.b). Although the use of mediators is necessary for those kinds of enzymes, it usually generates losses of electrode potential.

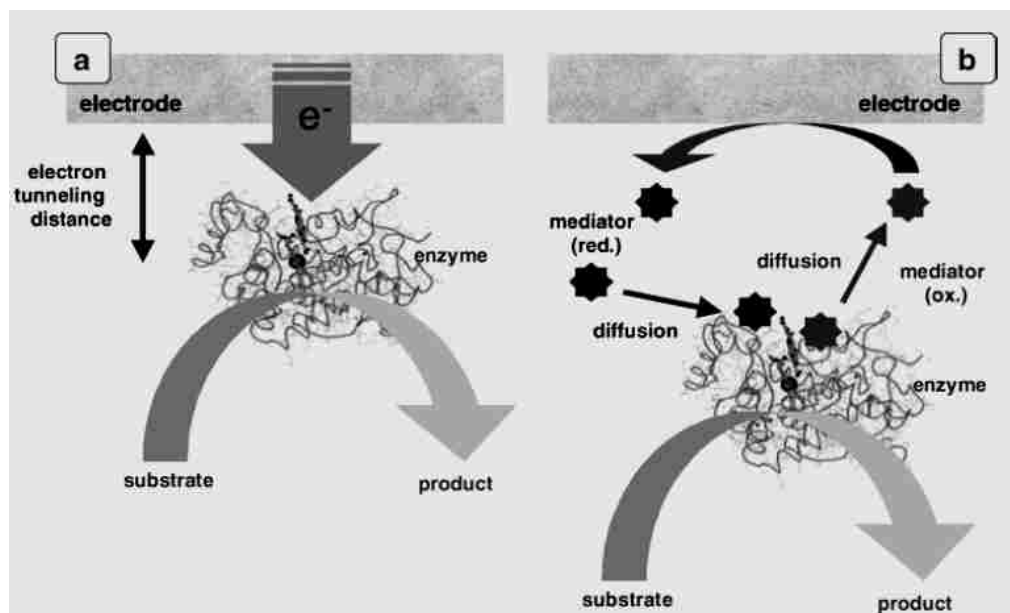


Figure 1.4. Mechanisms of electron-transfer. (a) Direct electron transfer (tunneling mechanism) from electrode surface to the active site of an enzyme. (b) Electron transfer via redox mediator (Barrton et al. Chemical Reviews, 2004, 104, 4867)

An example of mediated electron transfer is the oxidation of glucose by glucose oxidase, a dehydrogenase enzyme which is present in the glycolytic pathway. In Figure 1.5, the polarization curves of an enzymatic biofuel that would work with glucose as the biofuel show the thermodynamic potential of glucose oxidation and oxygen reduction [2]. According to this graph, the thermodynamic potential for the oxidation of glucose cell is 1.24 V. However, the oxidation of glucose through direct electron transfer is impossible because the glucose oxidase enzyme has a flavin type active site which is “buried” very deep in the protein shell of the complex enzyme molecule (Figure 1.6). There is no direct interaction between active site and electrode. From Figure 1.5 it can be observed that the first step in the oxidation of glucose can be performed by different dehydrogenases that are nicotine adenine dinucleotide (NAD^+), flavin adenine dinucleotide (FAD) or pyrroloquinone quinone (PQQ) dependant. Of these cofactors, the NAD^+ dependent glucose dehydrogenase has its thermodynamic potential closer to the glucose

thermodynamic oxidation potential, which allows for generating the maximum cell voltage.

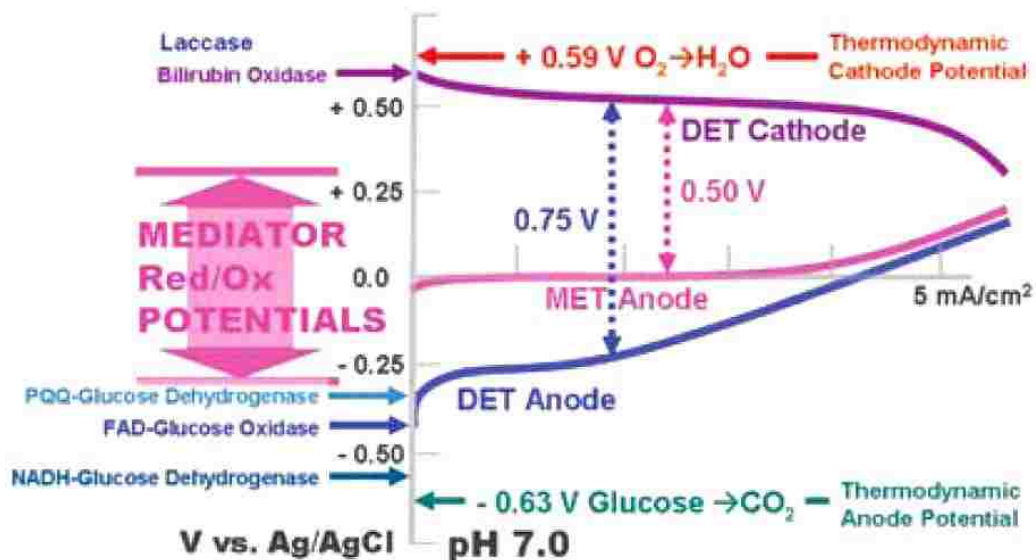


Figure 1.5. Polarization curves depict typical current performances for direct and mediated electron transfer in biofuel cell electrodes for different enzymes (*Atanassov et al. The Electrochemical Society Interface • Summer 2007, 28-31.*).

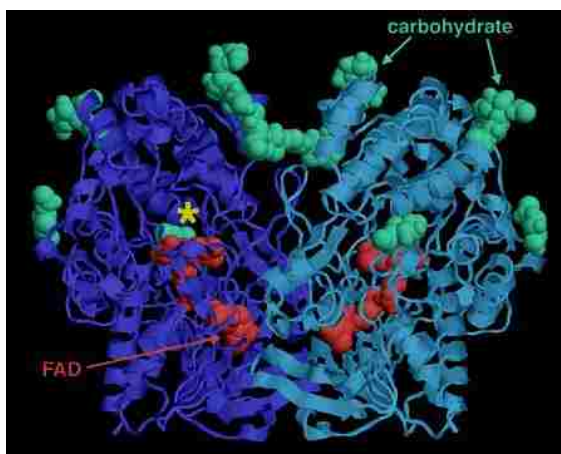


Figure 1.6. Glucose oxidase tridimensional structure-The flavin type active site (FAD is a cofactor attached to the protein structure) is deep within the shell, far from the protein surface (*Protein Data Bank*)

It is thought that a mediator immobilized on the electrode surface, because of its catalytic activity toward a given reaction, may affect the performance of the cell resulting

in the increase of the potential of the cell. This would be affected by moving to more positive values considering that

$$E_m = [(E_a + E_c)/2] \quad \text{Eq. 1.19}$$

where E_a and E_c are anodic and cathodic potentials. In this case, it is suggested that E_m values become more positive as the dimeric/monomeric ratios (d/m) decrease. The dimeric/monomeric ratios behavior could affect the electrocatalytic activity, since the thermodynamic driving force of the reaction can be increased [10]. This would be reflected by displacement of the reaction peaks in a cyclic voltammogram toward positive potentials.

Enzymes

Enzymes used in biofuel cells are biocatalyst proteins that accelerate oxidoreduction reactions. They can be categorized in three groups based in the location of the active site of the enzyme and the method of electron transfer between the active site and the electrode surface (Figure 1.7) [11]. Enzymes with diffusive active center are generally nicotinamide adenine dinucleotide (NADH/NAD⁺ or NAD(P)H/NAD(P)⁺); enzymes that have redox centers weakly bound to the protein enzyme (e.g. glucose and alcohol dehydrogenase) [12]. Enzymes with active sites closer to the shell of the structure have better interaction with the electrode surface (e.g. oxygen reduction multicopper oxidases such as laccase and bilirubin oxidase and peroxidases such as cytochromo c peroxidase). The aforementioned class of enzymes may interact with the electrode surface by a direct electron transfer mechanism. On the other hand, enzymes with the

active site buried deeply into the shell have no interaction directly with the electrode and the electron transfer mechanism is mediated.

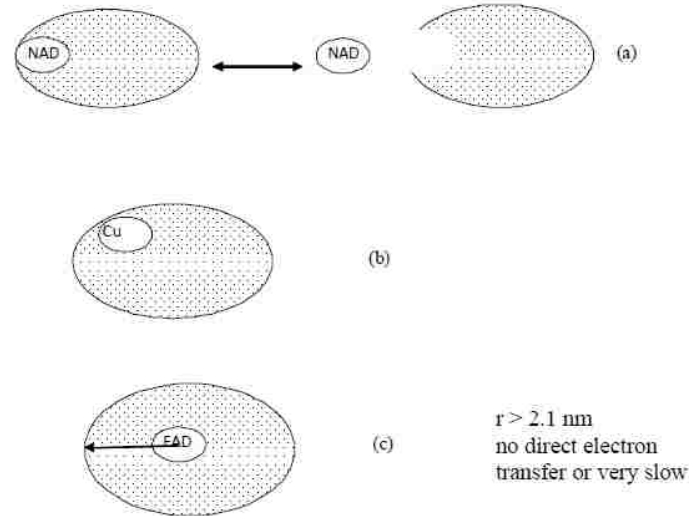


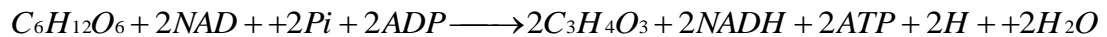
Figure 1.7. Three groups of enzymes based on location of enzyme active centre. E. H. Yu and K. Scott. *Energies* 2010, 3, 23.)

1.3.2. Anode Design Precedents

Enzymatic biofuel cells utilize enzymes as catalysts to perform the oxidation of organic biofuels in the anode producing a shuttle of electron that travel through an external circuit toward the cathode, where electrons will meet and produce the reduction of oxygen (Figure 1.1). The enzymes employed in the anode are chosen according to the biofuel to oxidize. Enzymatic biofuel cells have the advantage of generating a higher power density; in theory, this range is between 1.65 to 4.1 mW/cm² compared to microbial biofuel cells, 0.0010–0.09 mW/cm² [5]. However, their performance is limited by incomplete oxidation of fuel and low lifetimes. For example, the partial oxidation of glucose by a dehydrogenase would release 2 of 24 electrons decreasing as well the

theoretical energy density by 1/12[13]. The complete oxidation of pyruvate to carbon dioxide would be catalyzed by a cascade of enzymes found in the Krebs cycle in most living organisms. To oxidize glucose to carbon dioxide, the anode should contain the enzymes responsible for the oxidation of glucose to pyruvate found in the glycolytic pathway, in addition to the enzymes found in the Krebs cycle for complete oxidation of pyruvate [6, 13-15]. For the immobilization of these enzymes, one has to take into account that most of the enzymes of both the glycolysis and Krebs cycle are cofactor dependent enzymes requiring nicotinamide adenosine dinucleotide (NADH/NAD⁺) or flavin adenosine dinucleotide (FADH/FAD).

In glycolysis, the glucose is oxidized to pyruvate generating energy by synthesizing adenosine triphosphate (ATP):



In the Krebs cycle, the enzymes are NAD⁺ and FAD dependent enzymes. In this cycle, the pyruvate is further oxidized to Acetyl-CoA and enters to the cycle to be oxidized in a sequence of oxidative reactions [6, 13- 15]. The overall reaction in the Krebs cycle is:



To recreate this cycle, NAD⁺ has to be available into the system for the reactions to happen. Then, when immobilizing Krebs cycle enzymes (Figure 1.8) on the anode electrode, the NAD⁺/ NADH cofactors need to be present for the oxidation of the biofuel

to occur. However, it was found that NADH oxidation has a high overpotential [16-23]; energy must be applied for the reactions to occur. The passivation of the electrode is produced while the oxidation of the cofactor happens at the bare electrode [24]. Because of these reasons, a mediator must be used in order to catalyze the oxidation of the NADH cofactor to NAD^+ .

In this research, the last step in the Krebs cycle, the oxidation of L-Malate to Oxaloacetate catalyzed by a malate dehydrogenase (MDH) (Figure 1.9), was recreated. Methylene green (MG) electropolymerized on the surface of the electrode material was used as a mediator for the oxidation of NADH to NAD^+ to make this cofactor available to the enzyme [25-28].

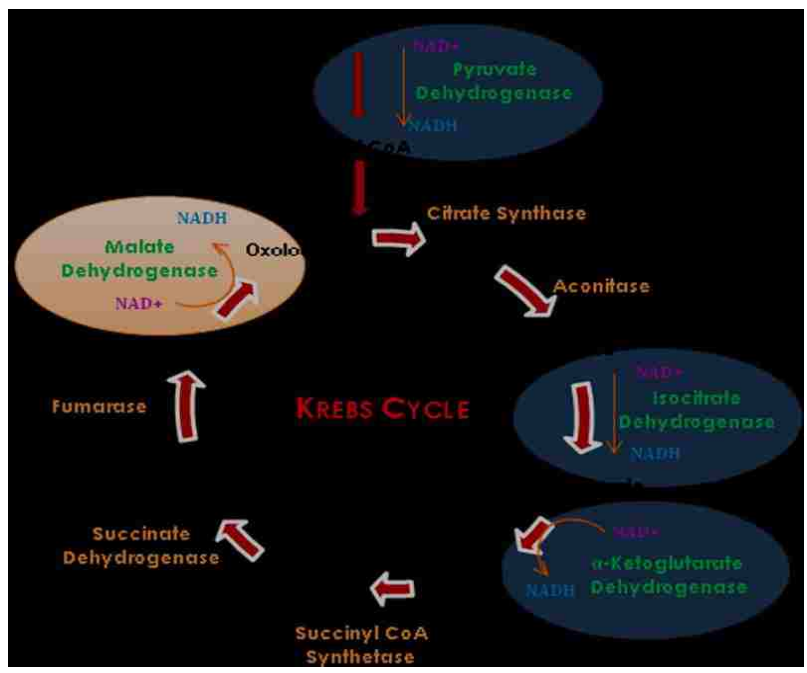


Figure 1.8. Krebs Cycle, also called Citric Cycle is methabolic path way for the complete oxidation of pyruvate - The NADH/ NAD^+ dependent Malate Dehydrogenase enzyme is the last step of the cycle.

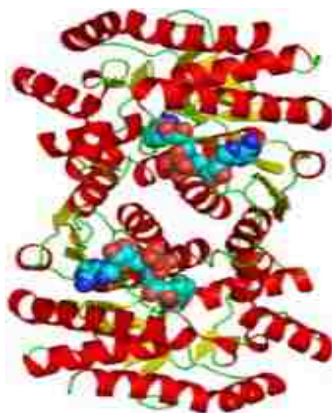


Figure 1.9. Malate Dehydrogenase Structure (Wikipedia)

Methylene Green- Biocatalyst for NADH Oxidation

In both the glycolytic and citric acid cycles, the dehydrogenase enzymes produce the breakdown of organic compounds. These are NADH/NAD⁺ dependent enzymes; their activity is limited to the availability of the oxidized form of this cofactor (NAD⁺) in the surroundings. During the oxidation of the biofuel substrate the oxidation is coupled to the reduction of the NAD⁺ cofactor to NADH; the reoxidation of NADH to NAD⁺ is necessary to perpetuate the reaction cycle.

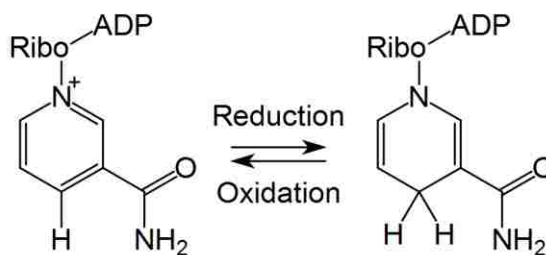
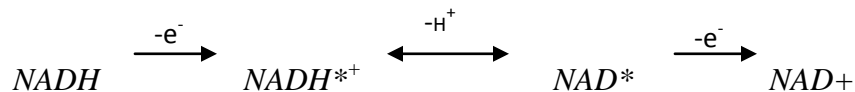


Figure 1.10. NAD⁺ reduction reaction to NADH(P.N. Barlet 2008)

NADH/NAD⁺ is a two electron, one-proton redox couple that undergoes a radical mechanism of oxidation. The initiation of the reaction through this mechanism, which is

the formation of the first cation-radical complex, is the limiting step of the reaction (see below) [30-35].



The excitation step forms a hybrid that later could derive into an alfa or beta form of the molecule. The formation of either of the forms is determined by the interaction of the intermediate structure with the enzyme. The inclination to generate those forms is related to the characteristics of the active site, it is different for different enzymes [36]. As a result, NADH needs to further transfer the charge to the electrode to release the electron and conduct work. This process occurs at large overpotential, as large as 1 V in an energetic scale (Figure 1.11). The successful oxidation of this cofactor gives the opportunity of using any of the NADH dependent dehydrogenases and, in this way, a larger range of biofuels.

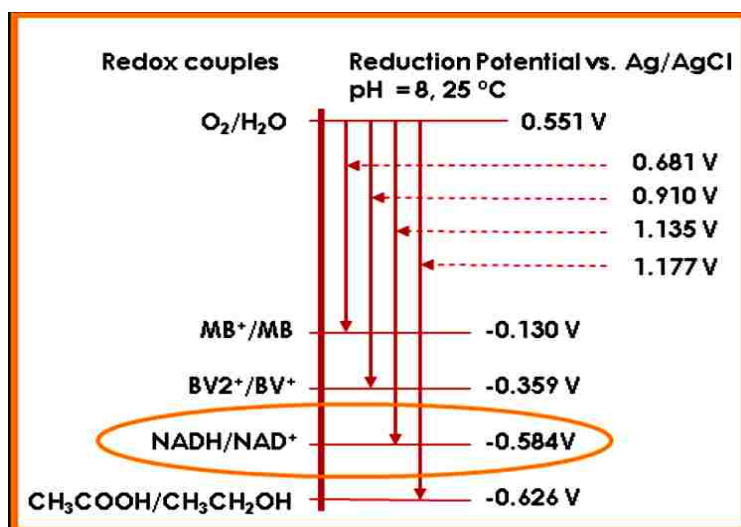


Figure 1.11. Potential of redox couples for dehydrogenase enzymes where NADH/NAD⁺ is shown to have a potential of -0.584 V at pH 8 (M. J. Cooney and B. Y. Liaw. P.S. Wang and J. B. Kim Editors. *Biomolecular Catalysis: Nanoscale Science and Technology*. 2008)

The oxidation of NADH can be performed by using a catalyst to improve the kinetics of the reaction. The catalyst or mediator will accelerate the first step of the radical mechanism mentioned above, shuttling the electron transferred from the electrode to the NADH substrate [25-29]. To this end, the chemically modified electrodes are designed to overcome the unfavorable kinetic barrier that this reaction presents. The mediator needs to undergo a two-electron process as well in order to accomplish a catalytic reaction [36]. For the NADH oxidation, the mediator needs to decrease the overpotential of the NADH oxidation reaction to minimize the energy losses of the cell and simultaneously approach controlled-diffusion reaction rates. To accomplish a satisfactory electrode design, the mediator needs to be immobilized on the electrode surface by undergoing an irreversible process that confers stability to the mediator structure. After immobilization, the mediator should have long-term stability and stability in presence of NADH; it has to catalyze the reaction without losing its structural properties and the interaction with the electrode surface. Moreover, the selectivity of the catalyst is prevailing; it should be selective for NADH to make NAD^+ available for the enzyme without having parallel reactions with other components of the solution [37-45].

In previous research good mediators for NADH oxidation, which included phenothiazine and phenoxazine derivatives, characterized as *ortho*- or *para*-quinones, were identified [25-28, 46]. It was observed that phenothiazine mediators had good catalytic activity due to the properties of the organic heterocyclic structures with C-C double bonds; single and double bonds alternating along the structure. The structure allows for good interaction with the electrode surface. Tse and Kuwana achieved the decrease of the NADH reaction overpotential to 0.4V using monolayer-modified-surface

glassy carbon electrodes [47]. These electrodes were created by modifying the glassy carbon surface with cyanuric chloride and later modified with dopamine, or 3,4-dihydroxybenzylamine. Other studies have demonstrated that Meldola's blue and toluidine blue can be used in an electrochemical sensor for NADH on carbon electrodes [48-49]. Pessoa et al immobilized Meldola's blue and toluidine in silica oxide matrices and bulk zirconium phosphate. More studies have suggested the use of methylene blue and methylene green (MG), phenothiazine dyes, as possible mediators for this reaction [49]. Dai et al showed successful immobilization of MG on glassy carbon for NADH sensing as well [46]. The contribution from Karyakin et al, Svoboda et al and Rincon et al in the electroanalysis and structural studies performed on MG were determinants in choosing this mediator in the research presented here [26-28, 50]. Rincon et al showed electrocatalytic activity of the polymerized MG (PMG) on glassy carbon with a potential as low as 50 mV (vs Ag/AgCl) toward the oxidation of NADH.

Considering all the factors mentioned above, this research focused in creating an electrode that could accomplish both oxidation of NADH and L-Malate by using MG as mediator. MG was immobilized on the electrode surface by electropolymerization (detailed later) and characterized by electron scanning microscopy and electron dispersion spectroscopy. NADH and L-Malate oxidation were evaluated by electrochemical procedures detailed later.

1.3.3. Cathode Design Precedents

Enzymatic biofuel cells are power devices that make use of the chemical energy from organic compounds to generate electric energy made available by catalytic activity of oxidoreductase enzymes. Oxidation of the biofuel is performed in the anode while oxygen is reduced in the cathode, releasing water as the product of reaction. The reduction of oxygen is achieved by employing enzymes extracted from eukaryotes and prokaryotes as catalysts. A cathode could also be designed to mimic the oxygen reduction found in living organisms. In the mitochondria of eukaryotes and some bacteria, oxygen is reduced by the electron transferred through the electron transfer chain, where the cytochrome oxidase enzyme transfers the electron to the cytochrome c cofactor, a hemoprotein cofactor, to reduce oxygen and form water. In prokaryotic bacteria such as *Myrotecium verrucaria* or *Trametes versicolor*, the reduction of oxygen is performed by activity of the enzymes Laccase and Billirubin oxidase (BOx) respectively (Figure 1.12) [5, 9, 51-53]. By using those enzymes on the surface of the electrode, one could reproduce the catalytic path ways of oxygen reduction as it happens in those living organisms.

For small portable devices the cathode is desired to be an air-breathing cathode. On the other hand, if the cell is thought to be part of a biomedical implantable device, it may use oxygen present in the blood of the host organism, but this depends on the planned use of the device [9]. In air-breathing cathodes, air is expected to be passively fed to the cell; in other words, the cathode has to feed itself by allowing mass transport to the catalytic layer of the electrode. Studies have demonstrated MET and DET mechanisms of interaction between the electrode and the active site of the protein. The

mechanisms are determined according to the location of the active site of the enzyme; if the catalytic site is available or is hiding in the shell of the enzyme when interacting with the cathode surface (see Enzyme section). The mechanism of electron transfer then depends on the enzyme to be used. It has been reported that cytochrome oxidase was used in a MET cathode design that used cytochrome c as mediator [56]. 2,2'-azino-bis(3-ethylbenzthiazoline-6-sulphonic acid) (ABTS) was also employed as a mediator in Laccase and BOx cathodes by Smolander et al. [57]. However, it has been proven also that these enzymes can work under a DET mechanism [58-66]; this was achieved by immobilization of the enzyme on the electrode surface. This mechanism is thought to give a better performance by decreasing losses of the cathode potential and the full biofuel cell.

In order to accomplish efficient electron transfer by DET, the active site and electrode surface distance has to be such that allows for electron transfer with minimum losses. The enzyme must be immobilized in such a way that helps to conserve the 3-D structure of the enzyme at a given pH and temperature, and allows for the best oxygen-electrode surface-active site interaction. Scientists have improved the immobilization technique for both enzymes, Laccase and BOx, on different materials. Heller et al. has co-immobilized Laccase and BOx on an electrically “wired” electron conducting hydrogel and later immobilized BOx on modified carbon fiber microelectrode (CFME) [55]. The group showed in a later experiment a cell performance of $268\mu\text{W}/\text{cm}^2$ and $350\mu\text{W}/\text{cm}^2$. Ivnistki et al. immobilized both enzymes on screen printed carbon (SPC) electrodes using Dithiobis(succinimidyl propionate) (DSP) as a linker in his first studies [70]. Later, Ivnistki et al., also, had immobilized BOx in carbon nanotubes (CNT) /Nafion membrane

and Laccase in a silica/CNT matrix in order to characterize the electrodes surface and the biocatalysts performance [66]. Recently, Wen et al. have achieved immobilization of BOx on single walled carbon nanohorns (SWNHs)-CFME to assemble a miniature glucose/air biofuel cell showing a power output of $\sim 140 \mu\text{W}/\text{cm}^2$ with an OCV of 0.7V [67]. This cell conserved around the 80% of its power after 12 hours of continuous work. As these studies show, the immobilization of the enzyme needs to allow an efficient electron transfer while preserving the structure of the enzyme to improve the cathode performance. Herein, one has to consider also that the enzymes chosen need to have high catalytic activity and stability. Finally, because the objective is to have a good performance of the biofuel cell or high power output, one has to look for an electrode design that would give the highest potential, close to the potential of the enzyme itself.

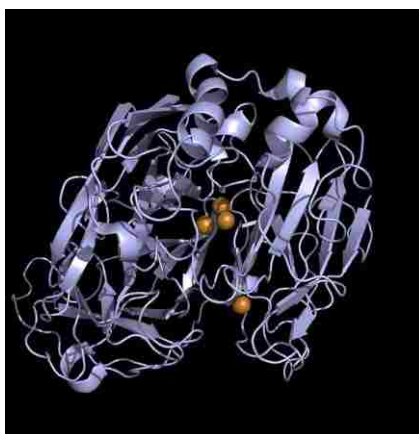


Figure 1.12. Laccase from *Trametes versicolor*, (armstrong.chem.ox.ac.uk/fuelcel.html)

Multicoper Oxidases Integrated in the Cathode Design

The oxygen reduction reaction (ORR) is a 4-electron pathway used in nature by multi-copper oxidase enzymes such as laccases, ascorbate oxidase or bilirubin oxidase [61-70]. These enzymes show efficient DET with carbon electrode materials (i.e. carbon

nanotubes, teflonized carbon powders, etc.) [61-66]. The structure and biochemistry of these multicopper oxidases (MCO) were extensively studied from a fundamental standpoint. The enzyme active site is formed by four copper atoms classified as Type 1 (T1) a paramagnetic copper and Type 2 (T2) and Type 3 (T3), diamagnetic coppers. One T2 and two T3 coppers form a trinuclear cluster center which is stabilized by a His-Cis-His tripeptide bridge (Figure 1.12). However, due to the complexity of multi-copper redox enzymes, it has been difficult to fully understand the electron transfer process.

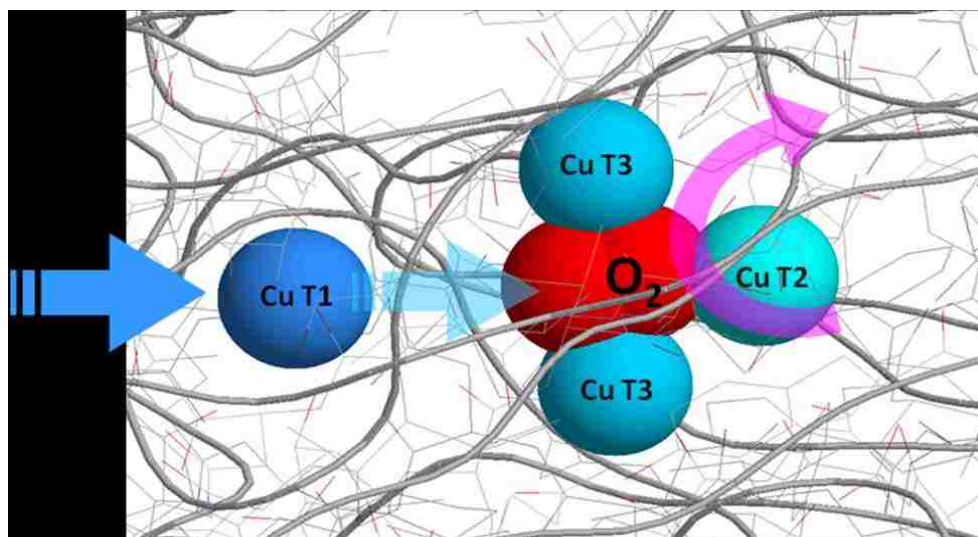


Figure 1.13. Multicopper Cluster Center- Oxygen Interaction (*Atanassov, P. Presentation on Multicopper Oxidases*)

Despite their similarity, these MCOs show different redox potentials. Theoretically, the potential difference is due to the absence of covalent bonds between the copper and histidine groups, where the hydrogen bonds vary with the distance of the coordinating histidine groups affecting the tripeptide bridge and the coppers' stability in the intermediary structure. The redox properties of these oxidases were studied in order to gain an understanding of the active site-conformation perturbations and arrangement of the monolayer enzyme immobilized on the electrode surface.

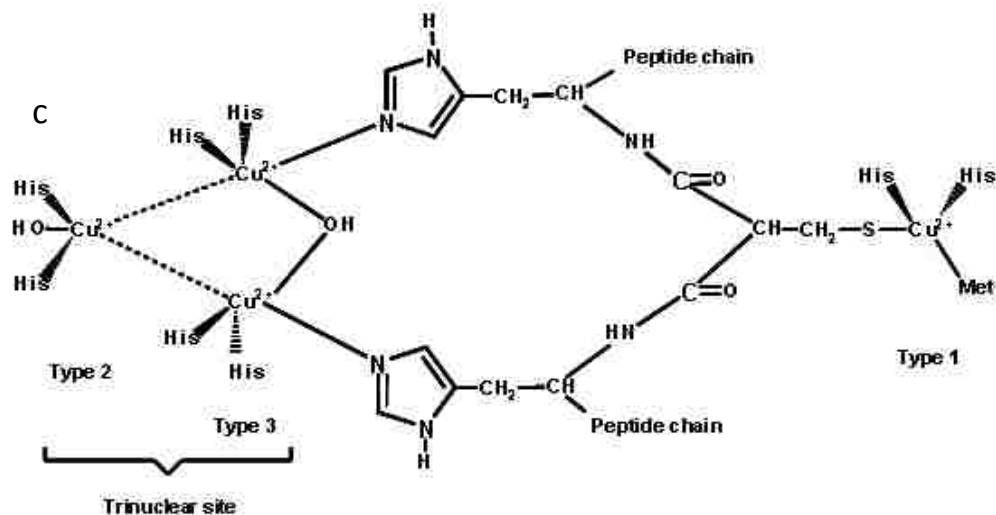


Figure 1.14. Multicopper Cluster Center conformation (Loera Corral Octavio et al. *Advances in Agricultural and Food Biotechnology*, 2006, 323)

The mechanism of oxygen reduction was studied in some oxidases more than others [68, 69]. Studies show that copper (Cu) in MCOs is involved in a mechanism in which a Cu^{2+} ion oxidizes the substrate by accepting an electron forming a Cu^+ that later will be reoxidized by transferring its electron to molecular oxygen. The required 4-electron transfer is accomplished using four copper sites (Figure 1.13). In the active site of the enzymes, the T1 copper is the primary electron acceptor, located at approximately 6.5 Å deep in the enzyme structure. This distance allows for electron tunneling and DET with the cathode material. The trinuclear cluster is located at 12 Å from the electrode surface and was proven to be the site where the molecular oxygen is attached by hydrogen bonding [65, 68- 69]. The enzyme stores electrons that traveled from the anode by getting completely reduced; this state contains four electrons that can be transferred to oxygen. The ORR starts when oxygen is bonded to the fully reduced Cu trinuclear cluster in presence of protons that traveled from the anode also (generally through a proton

exchange membrane (PEM)). The trinuclear cluster center is accessible to oxygen attachment and proton interaction via two electrolyte channels that connect the internal active site to the exterior of the enzyme. The reduction of oxygen is initiated by reducing the T1 copper and subsequently tunneling the electron down a His-Cis-His tripeptide to the trinuclear Cu cluster (Figure 1.14.b, Hopping ET) [65]. At least one of the two electrons from the T1 is tunneled toward the T3 in the trinuclear cluster. T2 is necessary for the oxidation of this reduced T3 allowing it to act as a two electron acceptor. It is believed that T2 participates in the transfer of one of the electrons required to reduce T3. T2 is thought to participate in the stabilization of the intermediary complex generated when oxygen is attached to the trinuclear cluster [68]. It was suggested also that alkaline values of pH promote the formation of a T2-OH complex (Figure 1.14.b, Non-hopping ET), inhibiting the oxygen reduction since T3 Cu cannot accept an electron until the OH group is dissociated from the cluster [71].

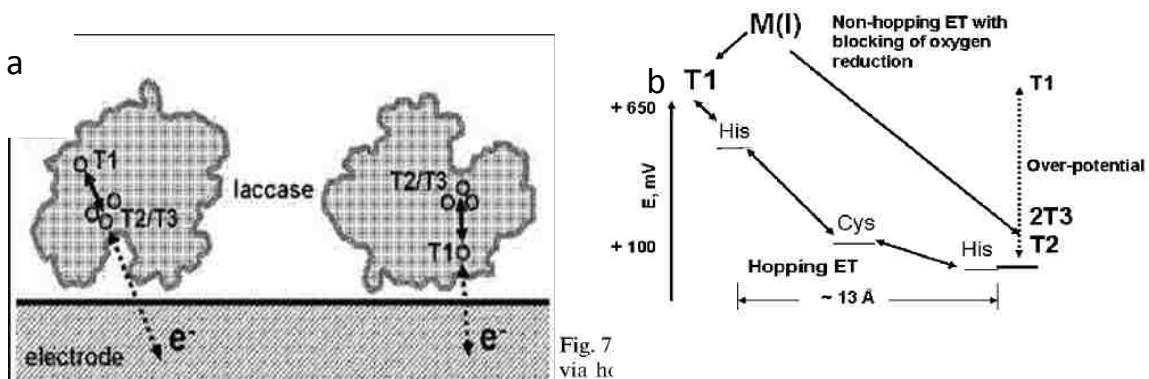


Figure 1.15. a) Laccase-electrode surface interaction, b) Intramolecular electron transfer in Laccase (Ivnitski, D.; Atanassov, P. *Electroanalysis*, 2004, 16 1182)

The multicopper cluster in Laccase was studied to determine the activity of the copper sites. Solomon's group applied X-Ray adsorption edge spectroscopy in the study of native Laccase and modified Laccases to have a better understanding of the

involvement of T1 and T2 coppers in the ORR [68]. Solomon used two modified Laccases samples: T2D and Hg1. In T2D, the T2 copper site was removed while the T1 and T3 coppers remained in the enzyme. In Hg1, T1 copper was removed and replaced by Hg^{2+} , which cannot undergo further reduction, and the trinuclear cluster was preserved in the active site. Both samples were compared to the native Laccase performance. In the first sample, T2D Laccase, the T1 copper is observed to be fully oxidized after shuttling its electron to the T3 coppers while both T3 coppers are oxidized and T2 copper is fully reduced. However, the T2D Laccase does not get oxidized later, it does not transfer its electron to the substrate and ORR of the substrate does not occur. Secondly, in the study of the Hg1 sample, the trinuclear cluster is observed to get fully reduced and later get oxidized allowing the ORR of the substrate. The electron is transferred to the cluster directly, it does not go to the Hg^{2+} (it cannot be reduced). Even though ORR happens in the Hg1 Laccase, the rate of reaction is $k > 1 \times 10^3 \text{ M}^{-1} \text{ s}^{-1}$ while the native Laccase shows a rate of reaction $k \sim 5 \times 10^6 \text{ M}^{-1} \text{ s}^{-1}$. These results show that T2 copper is required for oxygen reduction and Laccase reactivity since the ORR occurs in absence of the T1 copper (in Hg1 Laccase). The T2 site is involved in the trinuclear cluster stabilizing the intermediate formed when oxygen is attached to the active site. However, in presence of the T1 copper, the Laccase acts as a better catalyst. This is reflected by the decrease of the reaction rate of the ORR (the shuttling of electrons is faster). This shows that the integrity of the 4-Cu active site must be preserved for an efficient catalytic activity of the MCOs.

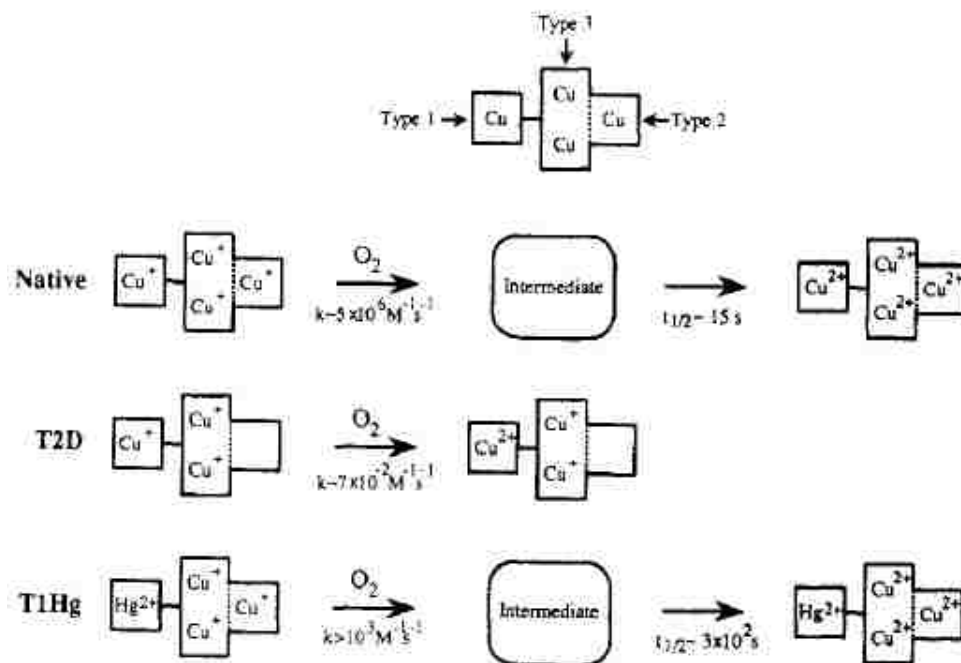


Figure 1.16. Activity of native and modified Laccase with oxygen (Solomon et al, *E. I. J. Am. Chem. Soc.* 1990, 112, 2243)

As stated earlier, understanding the intra-molecular electron transfer mechanism inside redox enzymes and the understanding of interfacial processes are necessary in order to “engineer” enzyme/ electrode interfaces. The study of the active site conformation-perturbations and arrangement of the monolayer enzyme on the electrode surface can help us develop a fully understood enzyme/electrode catalytic layer. As a consequence, we need to create a cathode electrode with controlled orientation, distribution and stability of the enzyme on the electrode surface by applying an adequate immobilization technique [2-3, 9].

Chapter 2. Experiments and Methods for Electrodes Integration

2.1. Enzyme Immobilization Techniques

The stability of enzymes determines the lifetime of biofuel cells. The lifetime of an enzymatic or any other biofuel cell can be improved by optimizing immobilization techniques for the electrode design. At the early stage of enzymatic biofuel cells, Willmer et al. and Katz et al. reported that enzymatic biofuel cells last only a few days [72,73]. Lately, studies have shown to approach a lifetime of 20 days for a glucose oxidase/BOx biofuel cell by immobilizing the enzymes in an Os-containing redox polymer [75]. Moore et al. and Minteer et al reported better results by entrapping dehydrogenases using tetrabutylammonium bromide modified Nafion membranes. Moore et al showed an enzyme-lifetime of 45 days after immobilization [75]. Minteer also reported mitochondria entrapment in that modified Nafion membrane that had a lifetime period of 60 days [5]. Ivnistki showed successful immobilization of Laccase and BOx in a silica-gel/CNTs matrices [62, 70]. These nanotube structures could provide better attachment of enzymes due to its conductive (metallic or semiconductive) behavior and similar surface size. Nanotubes materials in a composite electrode structure would increase the enzyme loading, thus improving the current and power densities of biofuel cells [2-3, 9, 67].

Enzyme immobilization could be based on simple physical adsorption of the enzyme on the electrode surface by crosslinking agents selected according to both electrode material and enzyme used, or by immobilization of the enzyme in a polymer

matrix. Herein, the enzymes used were Laccase and BOx. Laccase was immobilized by a crosslinking agent and BOx was immobilized in a silica-gel matrix.

Enzyme Immobilization by Crosslinking Agent for Anode Design

Crosslinking agents are compounds that attach to a surface by adsorption or covalent bonding. Agents that attach to a surface by covalent bindings modify the chemical structure of the electrode surface and its conductive properties as well. A covalent binding to a C-C- double bond (π orbital) in a single walled carbon nanotube (SWNTs), for example, would affect its conductive performance by breaking the quasi-metallic behavior of the electron cloud because a new bond is formed with the crosslinker. Due to this, the use of an adsorbed crosslinking agent is desired. This would attach to the surface of the electrode without altering the conductivity of the material. Chen et al reported the successful use of a linking agent, 1-Pyrenebutanoic Acid, Succinimidyl Ester (PBSE), as a noncovalent functionalization group for protein immobilization on SWNTs by π -stacking [76]. The pyrenyl group of the compound was reported to interact with the graphite plane as well as it does with the SWNT surface (π -stacking). However, it was found that due to the plane structure of the pyrenyl ring, this compound has better interaction with multiwalled carbon nanotubes (MWNTs) walls (Figure 2.1). Also, looking to the enzyme attachment, the *N*-hydroxysuccinimide side of the agent molecule reacts with an amine group of the enzyme forming an amide bond. This crosslinking agent attaches irreversibly to the SWNTs and MWNTs surface as well as the enzyme providing stability to the electrode catalytic layer in solution.

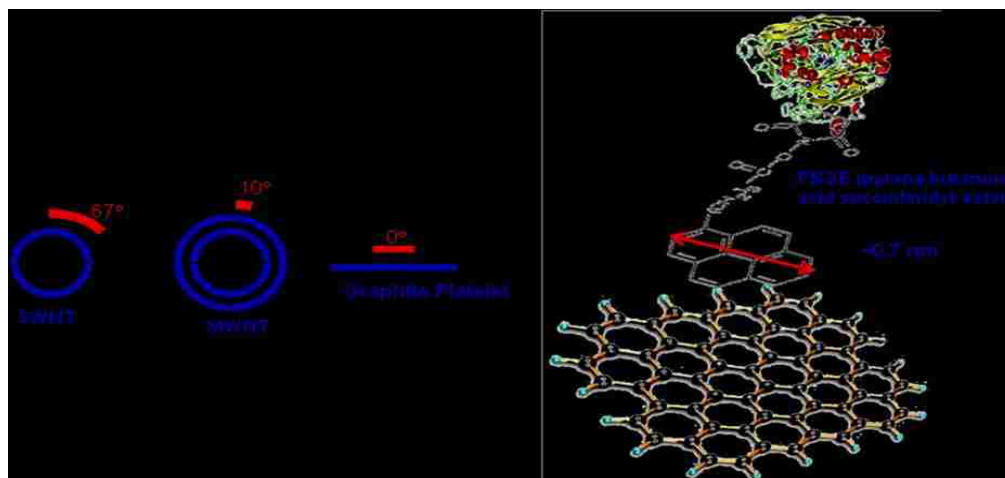


Figure 2.1. PBSE interaction with MWNTs surface (Chen, R.J.; Zhang, Y.; Wang, D.; Dai, H. J.)*Am. Chem. Soc.* 2001, 123, 3838)

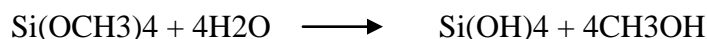
Enzyme Silica-gel Entrapment for Cathode Design

As stated early, nanostructures have a great potential for high enzyme loading, stabilization and activation of enzymes with high performances that are believed to go far from traditional electrode-enzyme immobilization techniques. Engineering the biocatalyst-electrode surface is the critical next step in biofuel cell design. Because of this, the enzyme entrapment in silica-gel, a technique mostly applied in pharmaceutical research for enzyme stabilization for drug delivery among others studies, was attempted.

In previous works, the immobilization of Laccase was achieved, but the enzyme denatured after a short period of time. To preserve the Laccase's structure and activity, the silicification process was applied. Laccase and CNTs was immobilized on Toray Paper (TP) electrodes using an *in-situ* silicification reaction [62]. Lysozyme was adsorbed onto TP to initiate a biosilicification reaction; a suspension of Laccase and CNTs was deposited on the surface of TP and later a silica precursor was added forming a

conductive matrix of silica and CNTs. This offered the combined advantage of enzyme stabilization, high electrochemical surface area, and enhanced electrical conductivity.

Silica-gel matrix formation by chemical vapor deposition (CVD) has been used as encapsulation and stabilization technique for protein [77]. Moreover, Lopez's group has been able to immobilize cell organelles such as liposomes and porphyrins, cell membranes and whole cells and has proven to conserve the organelles' stability [78]. The polymer precursor utilized is tetramethyl orthosilicate (TMOS), a volatile silica precursor at room temperature. The process is based in the volatilization of the precursor into a solution which contains the enzyme. The process is performed within a chamber with established dimensions (it was 50mm of diameter x 12 mm deep in this research) to allow the adequate mass transport. Once the precursor reaches the solution/ air interface, it reacts with water by a polymerization process. As a result, the enzyme is entrapped into a bulk silica-gel or silica matrix.



The principles applied in the study mentioned above could be applied to engineer the enzyme/electrode surface for a biofuel design. Herein, the immobilization should be performed in a conductive material such as carbon nano-composite materials that would provide a high surface area and high enzyme loading. It is prevailing to control thickness

of the catalytic layer to assure enzyme-electrolyte solution interaction as well as enzyme-electrode surface DET interaction while enzyme stabilization is achieved.

2.2. Integrating Composite Nanomaterials into Anode Designs and Cathode Designs

It is essential to engineer the biocatalyst-electrode surface since this step is a critical milestone in biofuel cells development. Various nanomaterials have shown a great potential to induce stabilization and activation of enzymes. High surface area nanostructures would provide enzyme attachment and large enzyme loading to increase current and power densities of enzymatic biofuel cells. Optimum carbon nanomaterial electrodes must simultaneously satisfy several competing criteria: high electrical conductivity, significant attractive interactions with enzymes, high surface to volume ratio, and sufficiently large pore size to facilitate mass transport. Engineering a system that meets these criteria requires fundamental understanding of the *combined effects* of nanomaterial chemical structure, dispersion state, processing path, and processing conditions on carbon nanomaterial electrode structure and enzyme/carbon nanomaterial interactions.

2.2.1. SWNTs- Integration for Anode Design

Carbon nanotubes are promising electrode materials for biofuel cell design because of its combination of the high electrical conductivity, mechanical strength and

thermal and chemical stability [58, 79-84]. In addition, their small diameters result in both high surface to volume ratios and favorable interactions with similarly sized enzymes. Recent investigations have demonstrated both immobilization of enzymes on carbon nanotubes due to the hydrophobic interaction of CNT and enzyme and direct electron transfer (DET) [1-3, 58, 80]. These promising initial results provide an impetus for engineering hierarchically ordered carbon nanotube structures with controlled surface chemistry [79, 85-86].

In this work, “Bucky” papers nanocomposites were used for the anode design. Combinations of SWNTs and isopropanol (IPA) and methylene green (MG) were used to create anode electrodes consisting of *hierarchically ordered carbon nanomaterials with controlled surface chemistries*. The SWNTs provide high electrical conductivity and enzyme interaction [82], while the other materials facilitate formation of a range of pore sizes; the larger pore sizes facilitate mass transport.

Carbon nanotubes (CNTs) belong to the fullerenes structural group. The structure of a SWNT can be compared to the structure of a graphene sheet rolled into a cylinder along a (m,n) lattice vector in the plane (with diameter $\sim 1\text{nm}$ and length/diameter ratio $\sim 132 \times 10^6/1$) [79, 87]. The (m,n) vector indicates the two directions of the hexagonal ring lattice. The n and m indices determine the chirality and the conductive properties of the nanotube; the angle formed between the hexagonal rings and the tube axis determine the band gap that gives the structure its metal or semiconductor behavior (Figure 2.2). When $m=0$, the nanotube has a zig-zag configuration (Figure 2.3.a). When $n=m$, the nanotube has an armchair configuration, its structure is quasi-metallic (Figure 2.3.b). In any other n,m correlation, the nanotube has a chiral configuration and metallic behavior

(Figure 2.3.c). In theory, a metallic SWNT is able to transport a current density approximate to 4×10^9 A/cm² [88]. The chemical bonding between the carbons of the nanotube is composed of hybrid sp² bonds. CNTs form “ropes”, they align themselves; this is due to Van der Waal (VdW) interactions between the orbitals of the grapheme structure.

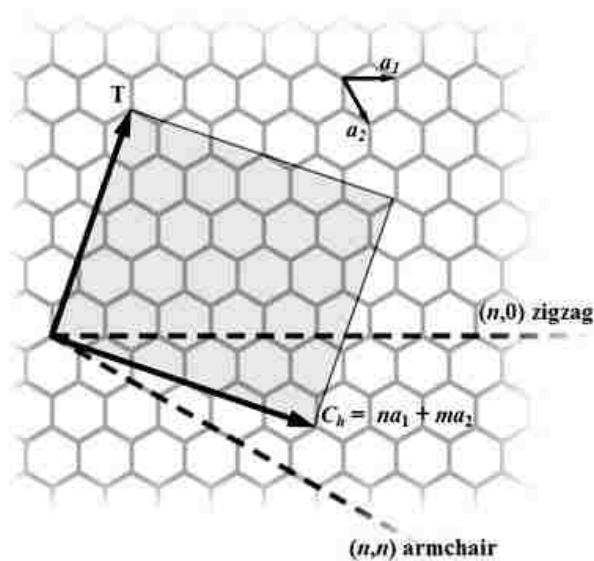


Figure 2.2. Schematic structure of a graphene sheet. The two basis vectors a_1 and a_2 are shown (Dai, H. *Acc. Chem. Res.* 2002, 35, 1035).

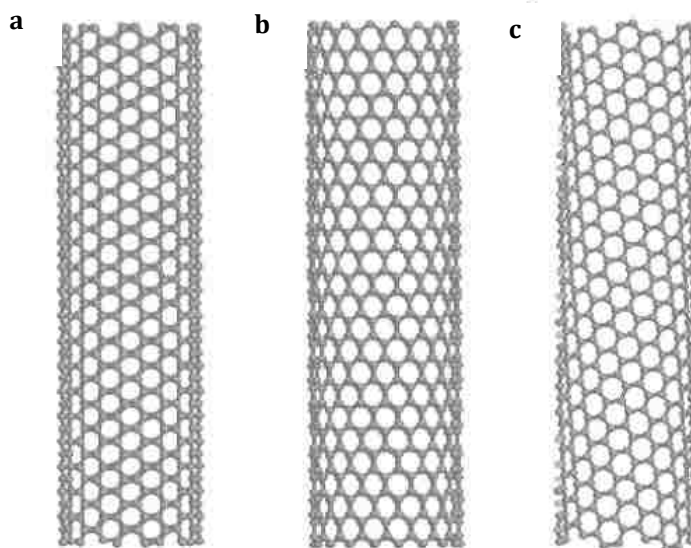


Figure 2.3. a) Armchair, b) zigzag, c) chiral configurations in a SWNT Dai, H. *Acc. Chem. Res.* 2002, 35, 1035)

The synthetic processes for SWNTs are chemical vapor deposition, arc discharge and laser ablation. The commercially available SWNTs are synthesized by CVD. One of the CVD synthesis procedures use methane as source of carbon and iron oxide nanoparticles or other metal catalysts supported on alumina as catalyst [79]. The synthesis is performed in a high temperature chamber (~1000°C). SWNTs synthesized by CVD on supported catalyst are semiconducting in nature. On their surface, covalent bonding of sidewall functional groups is difficult and produces the decrease in electrical conductivity due to loss of conjugation sp^2 . The noncovalent attachment of those functional groups however is possible and the sp^2 electronic property is preserved as well as its conductivity [76]. The anode design presented in this study is based on the noncovalent adsorption of PMG on the SWNTs' surface of the bucky paper composite.

2.2.2. MWNTs and Teflonized Carbon Fibers Integration for Cathode Design

As stated earlier, understanding the intra-molecular electron transfer mechanism inside redox enzymes and understanding of interfacial processes are necessary in order to “engineer” enzyme/ electrode interfaces. Controlled and oriented enzyme immobilization is needed to successfully improve the electrode design. Enzyme immobilization is performed by simple adsorption or crosslinking agents selected according to the electrode material employed. In this study, there are two cathode design developed that are based on multiwalled carbon nanotube paper (MWNTs) called “Buckeye” paper (BEP) and teflonized carbon fiber paper called “Toray” paper (TP).

Similarly to SWNTs, MWNTs are fullerenes species with structures alike to rolled graphite sheets into cylindrical shapes. A MWNT consists of structure with concentric tubes; it has higher diameter and length. The distance between the layers is approximately 3.4 Å. Because of its size, the external curvature of a MWNT could be approximate 10° while a SWNT has a curvature ~ 67° (Figure 2.1). The difference on curvature allows the MWNTs to be used for enzyme immobilization with the PBSE linking agent (Figure 2.1). The conductivity observed in MWNTs is higher than SWNTs due to the interaction of concentric layers by sp² bonds, π-configuration, that make the electrons transfer easier.

Toray paper (TP) is a material with high electrical and thermal conductivity, high strength and permeability, and minimal electrochemical corrosion. This material is made by a combination of carbon fibers with Teflon polymer. The high surface area of the composite material has the characteristics needed to be used as gas diffusion layer in fuel cell design; it was used in phosphoric acid fuel cells (PAPC), in polymer electrolyte fuel cells (PEFC) and expected to be applied in other fuel and biofuel cell designs [89]. Its manufacturer reports the material has very low resistivity ~80 mΩ in plane and ~4.7-5.8 mΩ through the plane [89]. The resistivity measurements vary according to the teflon content of the paper, which varies from 5% to 60% wt. The teflon percentage in the material also affects the gas permeability; the higher the percentage of the teflon in the composite the lower the gas permeability. In higher teflon percentage TP, the conductivity through the plane is not affected; this makes the material desirable to be used for enzymatic biofuel design. The high content of teflon makes the TP surface hydrophobic and could interact better with the enzymes which also has hydrophobic

characteristics. The TP surface will provide better enzyme-material interaction and increase enzyme loading on the surface while an adsorption immobilization technique is applied.

2.3. Physical and Electrochemical Characterization Techniques

The experiments performed in this study were used to create and characterize the surface of the anode and cathode electrodes. Electrochemical techniques were applied in order to engineer a design of a catalytic layer and to characterize the electrode surface: Open Circuit Voltage measurements (OCV), Cyclic Voltammetry (CV), Chronoamperometry and Chronopotentiometry. Additional physical characterization such as Scanning Electron Microscopy (SEM), Energy Disperse Spectroscopy (EDS) and Transmission Electron Microscopy (TEM) techniques were used in order to further characterize the electrodes surface.

2.3.1. Electrochemical Techniques for Electrode Characterization

The electrochemical techniques were applied to create and characterize the electrodes. The configuration of the electrolytic cell chosen is a three-electrodes cell which consists of working, reference and counter electrodes. The working electrode is the electrode to be evaluated. The reference electrode is an electrode with known potential against which the working electrode is compared. The counter electrode is an auxiliary electrode which acts as source or sink of electrons to balance the current in the working

electrode. The surface area of the counter electrode has to be ~3 times higher than the working electrode to avoid effects of this electrode on the electrochemical measurements.

Open Circuit Voltage

This technique is based on the measurement of the potential at zero current or at open circuit. The potential difference between the analyzed electrode and the potentiostat terminal is measured. This measurement gives information of the thermodynamics of the electrolytic cell, the thermodynamic potential of the enzyme-surface electrode. It does not provide any information of the kinetics and transport of the biofuel cell.

Cyclic Voltammetry

This technique provides information on the reversibility, kinetics of the electron transfer, and redox potential of the electroactive species. This is performed by linearly sweeping back and forth the potential of the working electrode within a potential range by a triangular wave form (Figure 2.4.a). Herein, the current is measured against the potential while a scan rate potential is applied. For an oxidoreduction reaction, the cathodic potential peak, E_{pc} , and cathodic current, i_{pc} , correspond to the reduction of the species, and are shown at negative sweeps ($Ox + n e^- \rightarrow Red$) (Figure 2.4.b). In the reverse direction, the anodic potential peak, E_{pa} , and the anodic current, i_{pa} , are shown at positive sweeps and correspond to the re-oxidation of the species ($Red \rightarrow Ox + n e^-$) (Figure 2.4.b). Finally, the redox potential of the species (Red/Ox), E^o , can be obtained from the equation stated early: $E^o = (E_a + E_c)/2$.

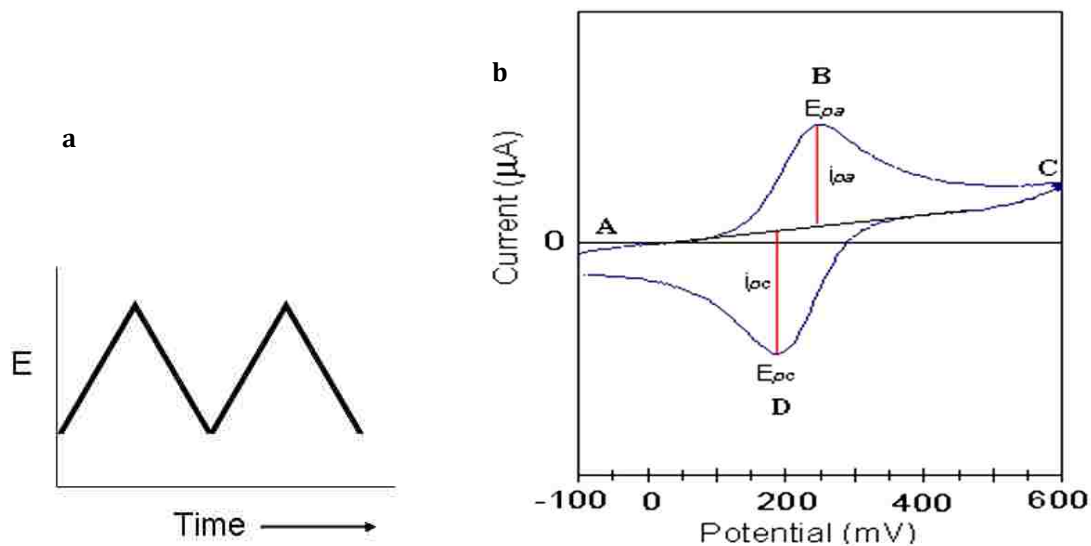


Figure 2.4. a) Plot of potential vs. time showing a triangular waveform in a CV, b) Cyclic Voltammogram for a reversible redox reaction

In this research, CVs are performed to electrochemically evaluate the electrodes and to immobilize the mediator for NADH oxidation (MG) by physical adsorption and electropolymerization of the monomer to PMG on the SWNTs electrode surface. Also, the cathode performance is tested by this procedure.

Chronoamperometry

Chronoamperometry is a potentiostatic technique that measures the faradic current generated as a function of time while a stepping potential is applied (Figure 2.5.a). The faradic current (as a function of time) shows the behavior of the charging double layer of the electrode at the applied potential and the exponential decay due to the electron transfer (Figure 2.5.b).

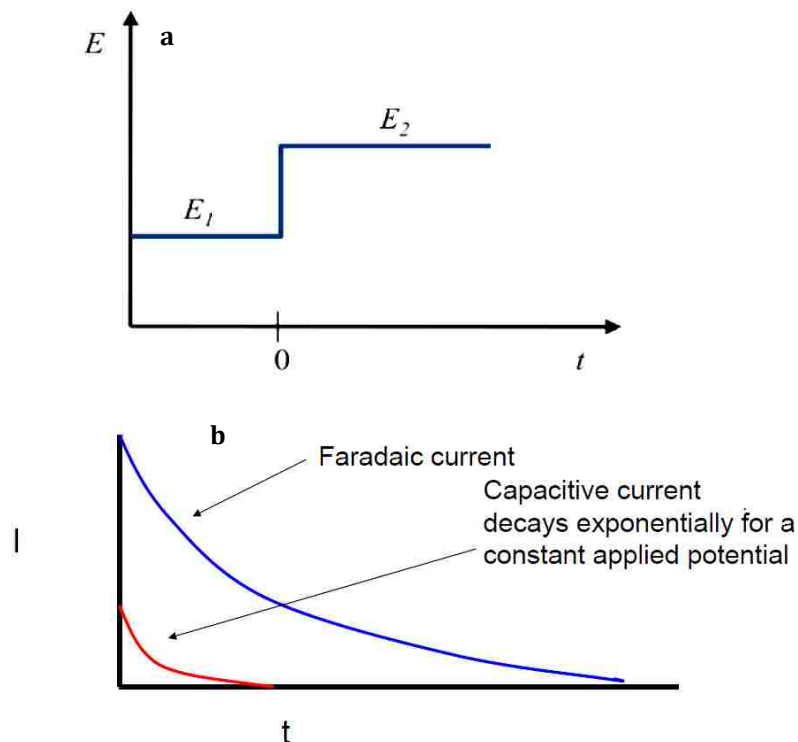


Figure 2.5. a) Stepped potential in chronoamperometry, b) Faradic current and exponential decay of current as a function of time

Chronoamperometry helps to relate the working potential of the working electrode while this approaches a constant current density for changing stepping potentials (Figure 2.6.a). In order to know the potential at which the working electrode is capable to have the best performance, stepping potentials are applied and the quasi-steady state current is measured. This process is followed until no change of current is observed for different stepping potentials; then, the data can be plotted in a **potentiostatic polarization curve**, current vs. potential (Figure 2.6.a). The working potential of the electrode is the potential at which the current starts its steady state behavior; the current approaches a plateau.

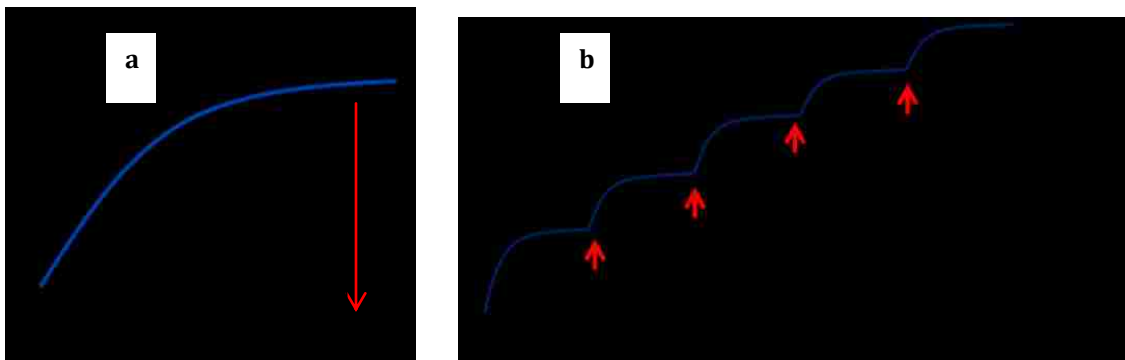


Figure 2.6. a) Potentiostatic Polarization Curve, working potential of the electrode is found when current approaches steady state behavior, b) Chronoamperometric curve, current vs. time, at a constant potential, the change in current measured is due to the change of the concentration of the reactant in the cell by aliquots added

Furthermore, the chronoamperometric measurements of an oxidoreduction reaction are used to characterize the process with respect to the analyzed species. Considering an enzymatic reaction as the process and the substrate as the analyzed species, it is possible to relate the behavior of the enzyme to the concentration of the substrate in the electrolytic cell. For this, the current generated in the redox process at a constant applied potential is monitored. In the cell, the current is measured while aliquots of the substrate are added producing a change in generated current (Figure 2.6.b). This technique can be further used to characterize the behavior of an enzyme with its substrate and its change in concentration. This technique provides more accurately information of the performance of the cell in real operational conditions.

Chronopotentiometry

In this technique, a controlled current is applied to the cell and the potential of the working electrode is monitored as a function of time. Galvanostatic potential is measured

when the applied current is constant (Figure 2.7.a). In order to sustain the constant current applied, the working electrode makes changes in potential to allow the process to proceed. In a redox couple, *Red/Ox*, as *Red* species moves from the electrode surface, the *Ox* species moves toward the electrode surface to be reduced on it; the space where the species travel is called the transition region and the time they take to travel this space is called the transition time. This technique is used to determine the electron transfer rate of the oxidoreduction reaction occurring on the electrode surface. By plotting the potential measured against the applied current, the **galvanostatic polarization curve** is obtained (Figure 2.7.a).

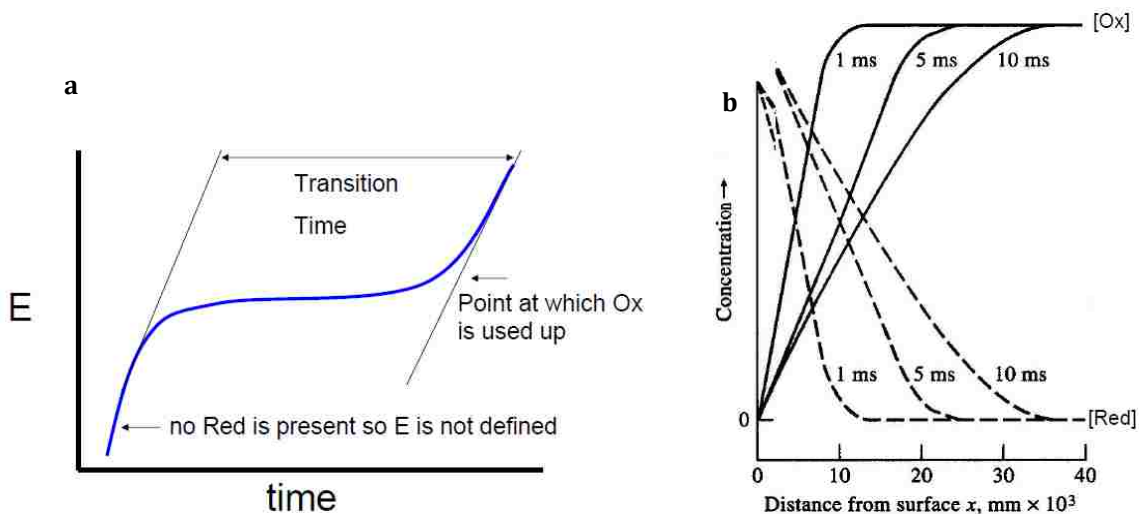


Figure 2.7. a) Chronopotentiometric curve, potential as a function of time at a constant applied current, b) Red and Ox species concentration with respect to the distance to the working electrode surface

2.3.2. Physical Surface Characterization Techniques

Scanning Electron Microscopy (SEM)

SEM is a technique that allows the imaging of the surface of a material at a micro and nanometer scale. A negative potential is applied to a tungsten wire generating an electric field; this electric field is then concentrated in the tip of the tungsten wire and an accelerated electrons beam is emitted. The SEM uses magnetic fields to focus the electron beam toward the sample. The beam of accelerated electrons carries energy when it collides with the surface of the material to be analyzed. As interaction of beam-surface is produced, the electrons are decelerated and energy is dissipated; as a result, secondary electrons, backscattered electrons and x-rays, visible light and heat emissions are observed. Secondary and backscattered electrons are detected and used to study the topology and morphology of the surface for SEM imaging.

Energy Disperse Spectroscopy (EDS)

The EDS characterization technique was used to analyze the chemical composition of materials. As stated above, for the SEM technology, when the accelerated electrons beam hit the surface of the sample, an emission of X-ray is produced. This emission is due to the inelastic collisions of the electron beam with electrons in the shell of the atoms of the sample; X-ray photons are generated due to the specific energy of the external orbital of the atoms that compose the sample. X-ray photons have the energy that corresponds to the energy difference between the levels of the electrons involved in the process. Those photons are characteristics of each atom and have a defined wavelength of

emission. These X-ray emissions are used to identify the atomic elements present in the sample. This technique is used to characterize qualitatively and quantitatively the elemental composition of the sample.

Chapter 3. SWNTs-Based ‘Bucky’ Papers Integrated to Anode Design

By mimicking the Krebs’ cycle, an enzymatic-biofuel cell will produce electric energy using low-cost organic natural sources [1-3]. In nature the Krebs' cycle is a pathway in which a cascade of redox reactions catalyzed by enzymes produces a flux of electrons in the oxidation of organic compounds such as sugars and alcohols. Most enzymes in the Krebs’ cycle are NAD^+ -dependent enzymes. In this research, malate dehydrogenase (MDH) is used to oxidize L-Malate (substrate) to Oxaloacetate. The L-Malate oxidation is a reaction coupled to the reduction of NAD^+ to NADH, where NAD^+/NADH acts as a cofactor. Thus, the performance of MDH is conditioned to the availability of NAD^+ . However, the oxidation of NADH to NAD^+ has been a major challenge to overcome during the past decades due to the slow kinetics of the reaction occurring at large overpotentials and the corrosion of the bare electrode oxidation [16-23]. As consequence, it is imperative to design a sensitive and stable electrode that promotes a low overpotential using a mediator that catalyzes the oxidation of NADH to NAD^+ (and its regeneration) and prevents the corrosion of the electrode material.

In order to overcome the obstacles presented by the kinetics of the NADH oxidation [36] and the MDH performance, this research focused in the design of a stable anodic electrode based on SWNTs-papers and a mediator. The electrocatalyst employed was poly-methylene green (PMG), a highly stable electroactive phenothiazine with catalytic activity for this redox reaction. During the past few years substantial effort was placed in investigating the structure and catalytic activity of such PMG catalytic materials [25-28,

50]. The PMG was deposited on the surface of the “bucky” papers [90-92] by electrochemical polymerization of the methylene green (MG) monomer [93]. The performance of the electrode toward NADH oxidation and L-Malate oxidation was tested by applying chronoamperometric measurements [94]. An additional characterization of the materials was developed by Scanning Electron Microscopy (SEM) and Energy Disperse X-Ray Spectroscopy (EDS) for further understanding of the “bucky” paper-MG electrode.

3.1. Experimental and Methods for Anode Characterization

Apparatus

The electrochemical experiments were performed in a three-electrode cell by conventional potentiostats: Gamry Reference 600 Potentiostat/Galvanostat/ZRA and Princeton Applied Research VersaSTAT 3 potentiostat / galvanostat. All potentials are reported vs. Ag/AgCl. The material characterization was performed using a Scanning Electronic Microscope Hitachi (S-5200) equipped with an Energy Dispersive Spectrometer (EDS).

Chemicals for anode Design

HiPco SWNTs were obtained from Unidym Inc. (Menlo Park, CA) and had a length to diameter (aspect) ratio of ~ 600 and a purity of ~ 90%. Isopropanol (purity > 99%), Methylene Green (MG) Zinc Chloride double salt (purity > 99%, from Fluka Cat. 66870), NADH (purity ~98%, Sigma Cat. N6005), NAD⁺ (purity ~98%, Fluka Cat.

43407), Lyophilized Malate Dehydrogenase (MDH) from porcine heart (activity 2700un/mg protein, USB products from Affymetrix Cat. 18665) and L-(-)-malic acid (Sigma Cat. M1000) were used without further purification. KNO_3 , NaNO_3 , Monobasic and Dibasic Sodium Phosphates were obtained from EMD Chemicals Inc. were used to prepare the pH 7 phosphate buffer stock solution. TRIS buffer at pH 7 was made from Tris(hydroxymethyl)Aminomethane (EMD Chemicals 9210) , Hydrochloric acid 1.0 N (VWR 7647-01-0) and used to prepare the MDH enzyme stock solution. L-malic acid was prepared with distilled water and its pH was adjusted to 7.1 with concentrated NaOH solution.

SWNTs- Papers - “Bucky” Papers

Two types of SWNT “bucky” papers [47-48] were fabricated for and employed in this work. BP11 “bucky” paper was fabricated by magnetically stirring 60 mg of purified HiPCo SWNTs in isopropanol (1 mg/ml) for three days to produce a uniform dispersion of small bundles. Then, the dispersion was filtered through a 0.2 μm PTFE filter paper. The BPMG “bucky” paper was fabricated by stirring 60 mg SWNTs and 13 mg MG in isopropanol (1 mg/ml) followed by filtering the suspension through a 0.2 μm PTFE filter paper. The “bucky” papers were dried at room temperature for 15 minutes, peeled off the filter paper, and vacuum dried overnight at 80 °C. The thickness of the “bucky” papers was measured to be approximately 350 μm .

In order to maintain the SWNTs’ pristine properties, no sonication or functionalization was performed. The SWNTs were stirred in isopropanol to break up large nanotube aggregates while still retaining large ropes of nanotubes. The presence of

nanotube ropes in the “bucky” paper increase the porosity of the “bucky” paper, thus facilitating enhanced transport of materials while still preserving a network for electrical conductivity. The MG and SWNTs were stirred together, prior to filtration, in order to distribute MG evenly through the nanotubes and to maximize interfacial contact between the SWNTs and MG.

Cavity Anode Design

The cavity electrode design was chosen for this study. 50% teflonized carbon powder (XC50) was used as adherent material and compacted into the cavity of the electrode. Then, a piece of “bucky” paper that fitted the cavity diameter was placed and pressed on top of the compacted XC50 and adhered to it. The “bucky” paper’s surface was further modified by PMG deposition.

The PMG was deposited on the surface of the “bucky” papers by electrochemical deposition in a three electrodes cell, where Ag/AgCl (CH Instruments Inc. Cat. CHI111) and Pt (0.127mm and purity 99.9% Alfa-Aesar Cat. 10282) were the reference and counter electrodes used respectively and the “bucky” paper cavity electrode played as the working electrode. The electrodeposition was performed by means of 10 cyclic voltammograms [95] at a scan rate of 5 mV/s within -0.5 to 1.3 V range following the standard protocol by Svoboda et al. [96]. The MG growing solution consisted of 0.5 mM MG and 0.1 M KNO₃ dissolved in 10 ml of 50 mM sodium phosphate buffer solution at pH 7. The process was performed in absence of oxygen to avoid the oxidation of the polymer; nitrogen was used to deplete oxygen from the growing solution. Similar steps

were used with rotating disk electrode (RDE) at 1600 rpm. By following this procedure, the BP11-MG and BPMG-MG electrodes were created.

Hydrodynamic Polarization Curves

In order to find the working potential at which PMG on the electrodes oxidizes NADH and MDH oxidizes L-Malate, hydrodynamic polarization curves were developed using both BP11-MG and BPMG-MG electrodes for the static as well as the RDE at 1600 rpm. The curves were obtained by plotting the measured current against the respective potential. The steady state currents were measured by applying constant potentials that ranged from -0.05 V to 0.35 V by increments of 0.05 V. For NADH, the current was measured in 10 ml cells of 1 mM NADH, 10 mM NADH and a blank of phosphate buffer for both electrode materials, BP11-MG and BPMG-MG.

Chronoamperometry for NADH oxidation

The concentration of the NADH stock solution was determined and used in chronoamperometric measurements. The concentration of the NADH stock solution was found by measuring the absorbance of this compound applying UV-VIS spectroscopy and the law of Lambert-Beer. This law establishes a linear relationship ($A=\epsilon bC$) between the UV-VIS absorbance of a compound to its concentration, C (molar units, M), its molar absorbtivity, ϵ ($M^{-1}cm^{-1}$) and the width of the cuvette, which contains the sample (cm). The concentration was determined at the highest absorbance peak, close to unity, in the UV-Vis spectrum in a 300 to 500 nm wave length (λ) range. The absorbance peak for

NADH was found at $\lambda=340$ nm. Its concentration was easily found since the absorptivity for NADH is $\epsilon=6300 \text{ M}^{-1}\text{cm}^{-1}$ at standard condition and the conventional cuvette has 1cm of width. The absorbance measured was effectively linearly dependent of the concentration in the 0 to 6 mM NADH range; high concentrations of NADH showed high absorbance. Then, the performance of the electrodes was analyzed by chronoamperometry.

Chronoamperometric curves were obtained by monitoring the current generated by consecutive periodic addition of NADH or L-Malate aliquots to the electrolytic cell as a function of time. 0.3 V, ideal working potential found through the hydrodynamic polarization curves, was applied to evaluate the performance of the electrodes for the NADH oxidation. This experiment consisted of adding aliquots of 58 mM NADH solution (NADH stock solution) to the electrochemical cell which initially contained 10 ml of phosphate buffer solution. Before the first aliquot of NADH was added to the cell and after each posterior addition, the system showed steady state current behavior. Each addition was made in a time interval of 500 seconds to allow the system to approach steady state. The currents were measured after each aliquot added and were plotted against the respective concentration of the NADH in the cell.

Chronoamperometry for L-Malate oxidation

Chronoamperometric measurements were also developed to evaluate the MDH behavior using the BP11-MG and BPMG-MG electrodes. For the evaluation of the enzyme performance, the current was monitored for each aliquot of the L-Malate (substrate) added to the electrolytic cell where a constant 0.1 V voltage was applied.

Initially, the cell contained 50 μl of enzyme ---dissolved in TRIS buffer in a proportion of 1mg:100 μl respectively, 10ml of 10 mM NAD^+ dissolved in phosphate buffer at pH 7 and 45.0 ± 0.1 mg KNO_3 . In this step, each aliquot of 1 M L-Malate was added to the cell after the steady state current was approached in time intervals of 400 seconds. The measured steady state current was plotted as a function of the respective substrate concentration. The mentioned procedure is used to gather data to evaluate the kinetic behavior of the MDH enzyme in the oxidation of L-Malate using the “bucky” papers electrodes BP11-MG and BPMG-MG.

Resistivity, Wettability and SEM imaging of “Bucky” Papers

BP11 showed a resistivity of 14.7 m Ω / mg and BPMG 47.2 m Ω /mg; a copper (Cu) wire was used as a blank. As expected, both “bucky” papers show low resistivity demonstrating their high quality as conductor material for the design of our electrodes.

The SEM micrographs show how the strains of SWNTs effectively conferred a high surface area to the “bucky” papers and high porosity due to the bundles formed by the nanotubes (Figure 3.1). There were no treatment or conductive coatings performed on the samples prior to SEM observations. The combination of porosity provided by the SWNTs and hydrophilicity provided by the IPA conferred high wettability to the “bucky” papers. BP11 and BPMG were easily wetted but BPMG showed to be more hydrophilic than BP11 due to the presence of MG (highly hydrophilic and soluble in water). Due to their porosity and their hydrophilicity, both materials are fragile. Despite their fragility, they were easily used in the fabrication of these cavity anodes.

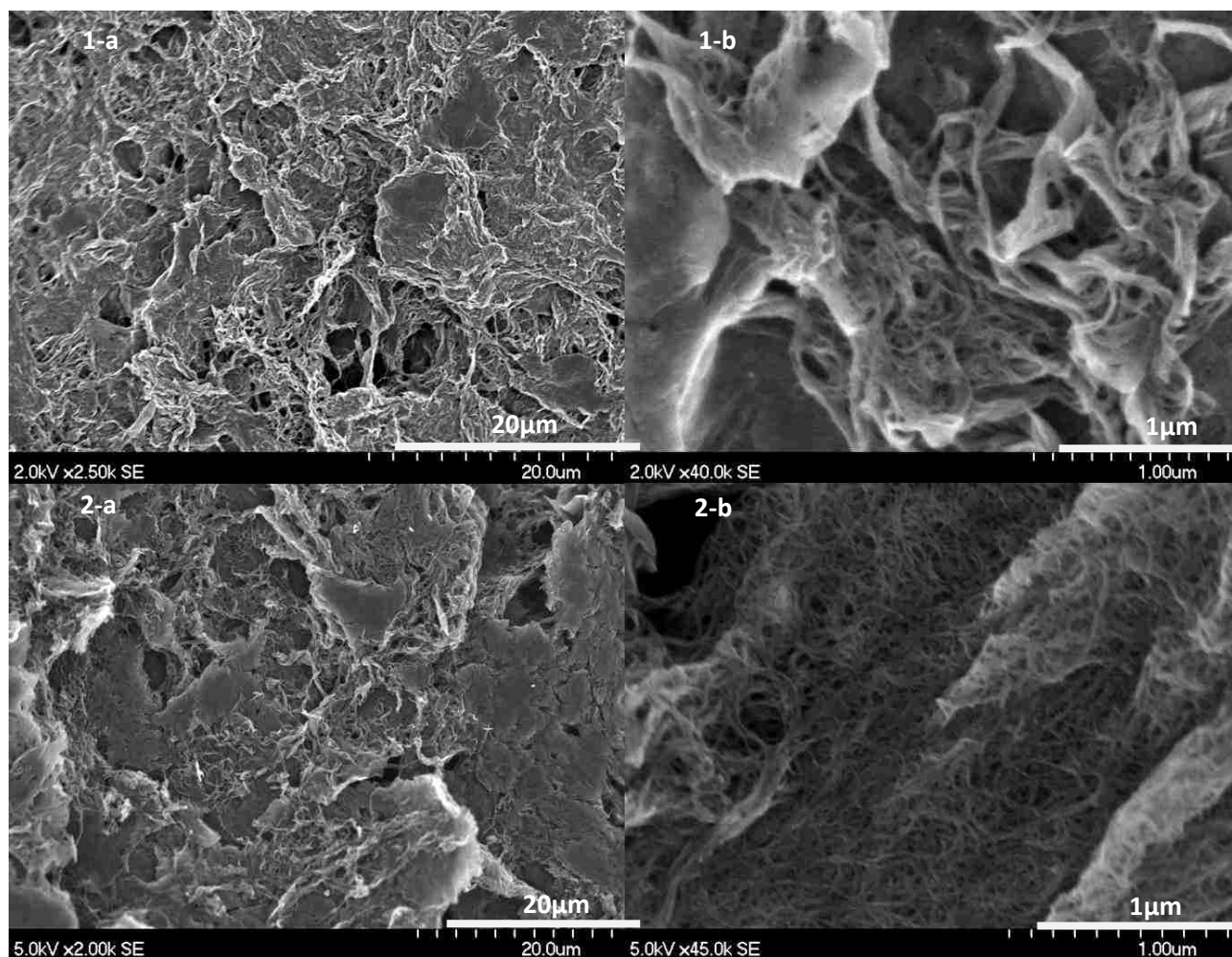


Figure 3.1. SEM Images of 1-a) & 1-b) BP11 (SWNTs + IPA) and 2-a) & 2-b) BPMG (SWNTs + IPA + MG) before MG electrodeposition.

Methylene Green Electrodeposition

MG was deposited on the surface of the “bucky” papers by means of 10 voltammetric cycles within -0.5 V and 1.3 V at 5 mV/s of scan rate. The oxidative peak of MG is observed at 0.1 V in the first cycle and 0.2 V in the 10th cycle on both BP11 and BPMG papers for the static (not shown) as well as the RDE (Figure 3.2) electrodes. The displacement of the oxidative peak indicates that an oxidative polymerization is taking place and more electroactive species are being deposited on the surface of the electrode

[28, 82]. A background was also performed in this step using XC50-Carbon Black and XC50 (not shown). On both “bucky” papers, the MG electrochemical deposition generates a nucleation of PMG that results in the formation of particles observed on their surface by SEM imaging (Figure 3.3).

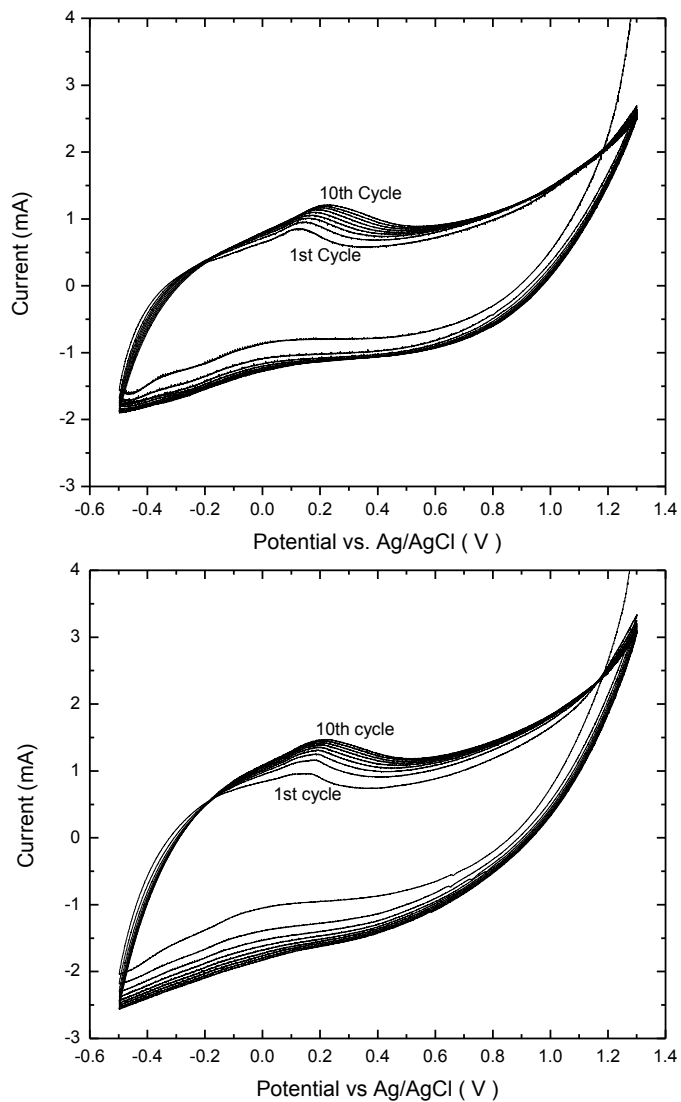


Figure 3.2. Electrodeposition of MG at 5 mV/s between -0.35 to 1.3 V on a) BP11 (SWCNTs+IPA), b) BPMG (SWCNTs+IPA+MG). The peak shift indicates the polymerization reaction takes place

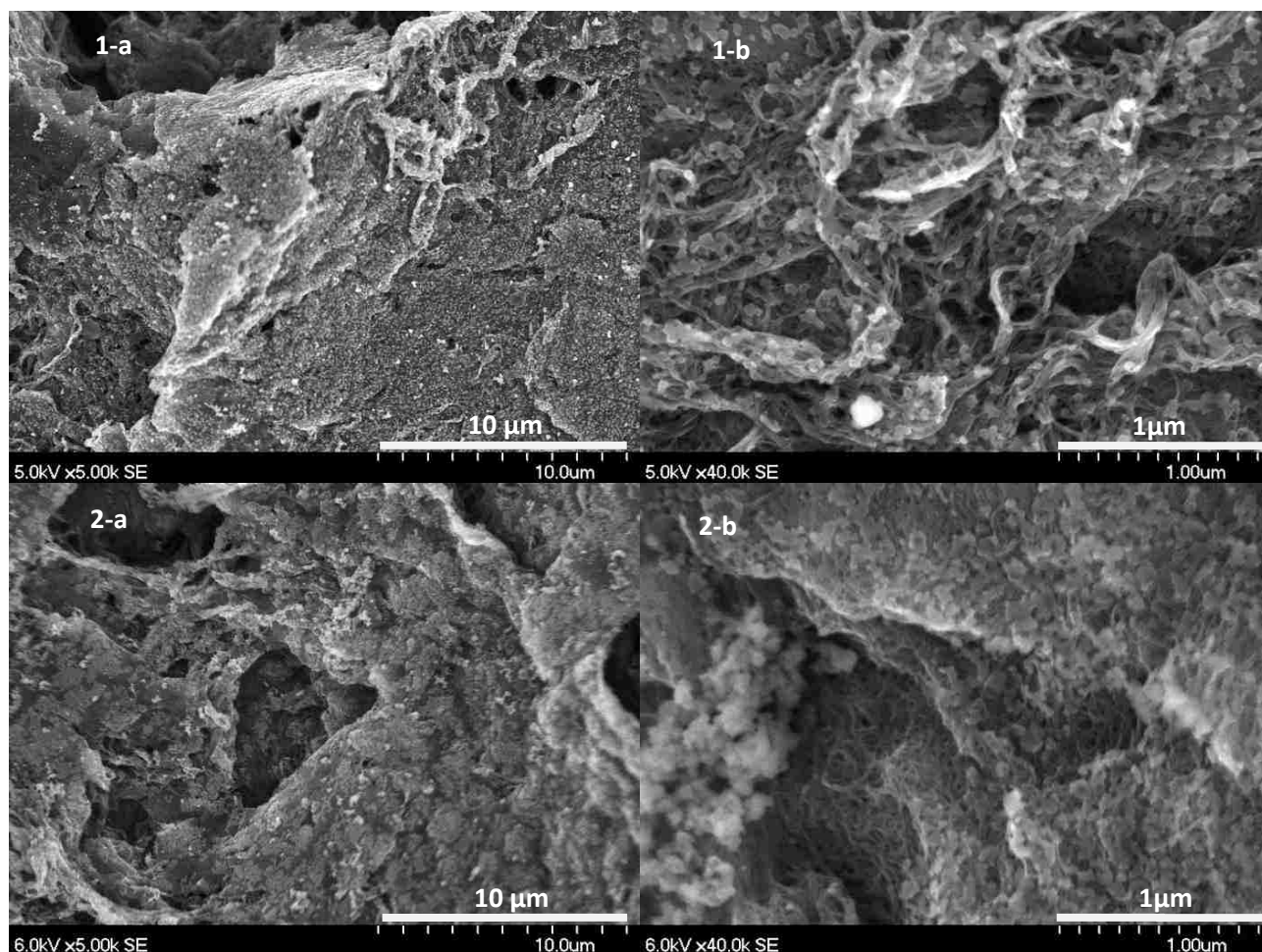


Figure 3.3. SEM images of surface electrodes after MG electrodeposition 1-a) & 1-b) BP11-MG and 2-a) & 2-b) BPMG-MG.

The EDS techniques were applied to corroborate the polymerization of MG was successfully performed. By SEM imaging, the particles of polymers are observed on the surface of the material (Figure 3.3) which shows a noticeable difference compared to the initial clean surface-material shown in Figure 3.1. The particles vary from 10~20 nm to 1 μ m (Figure 3, 1-b and 2-b) and are uniformly distributed on the “bucky” papers surface. Since electrolytic salts are used in the process of polymerization, it is logic to believe the nucleation observed may be due to the precipitation of electrolytes. Because of this reason, a further analytical study by EDS was performed applying a 10 KeV beam. For this analysis, the structure of the MG monomer was taken into account and from it, Sulfur

(S) and Zinc (Zn) were traced on the BP11 surface (Figure 3.4). In this case, the presence of sulfur and zinc on the surface would demonstrate an effective polymerization because MG is the only source of them. The EDS spectrum demonstrated that MG was successfully deposited on the BP11 (Figure 3.4); Table 1 shows that sulfur constituted the 5.26% of the total deposited compounds to the BP11 paper surface as well as zinc (5.26%). BPMG is expected to have MG deposited on its surface as well since the same procedures were applied in its process. To corroborate these results and that no other compound was deposited, the “bucky” papers were subjected to cyclic voltammetry in a background solution without the MG monomer. These solutions contained the buffer and KNO_3 in similar quantities than the MG growing solution. After exposing the material to 10 voltammetric cycles, the surface of the BP11 was analyzed through SEM imaging and EDS. SEM images showed that there was precipitation of electrolytes, there were sporadic formations of particles on the BP11 surface (not shown). However, the EDS analysis showed presence of neither sulfur nor zinc (spectrum not shown). The EDS shows that meaningless amounts of electrolytes in the growing solution precipitated on the “bucky” paper’s surface but PMG was successfully deposited (Figure 3.4). Further chronoamperometric measurements confirmed the MG polymerization on BP11 and BP-MG and show the PMG performance as mediator in the anodic process.

Table 3.1. EDS data of the surface of BP11-MG electrode, composition of the elements deposited on the carbon SWNT electrode

Element	O	K	P	S	Zn	Total
Wt%	36.84	10.53	42.11	5.26	5.26	100

Methylene Green Monomer

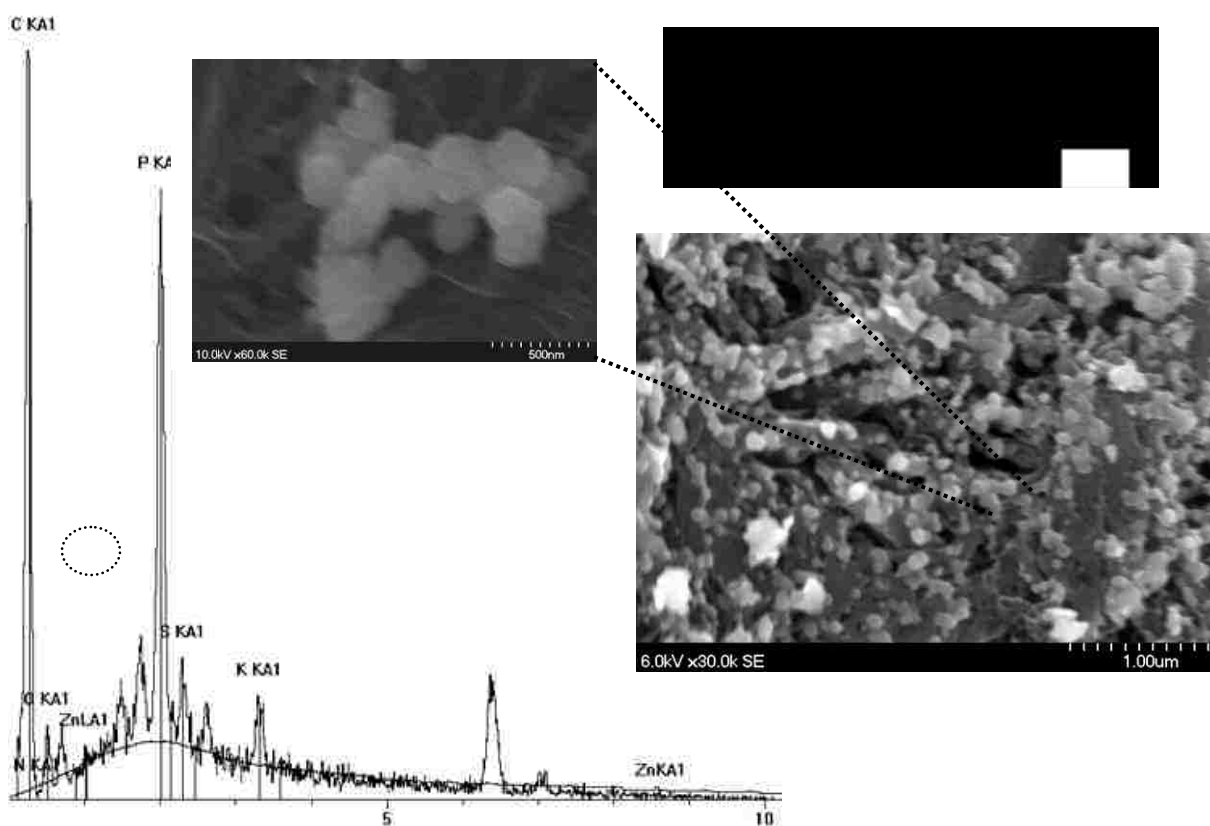


Figure 3.4. EDS spectrum of the surface of BP11-MG Electrode

Hydrodynamic Polarization Measurements

By constructing a hydrodynamic polarization curve, the ideal working potential for NADH was determined for both BP11-MG and BPMG-MG electrodes. For the BP11-MG electrode, the working potential found was 0.3V (Figure 3.5-a); this was applied to perform chronoamperometric measurements for NADH. For a 10 mM NADH the current is proportionally increased with the concentration of NADH compared to 1 mM NADH and the buffer background. In Figure 3.5-b, the compositional material MG proved to induce an increment in the current generated at the same potential range of testing (-0.05 to 0.35 V). The current measured is approximately 95 μ A at 0.2 V on BPMG-MG

electrode (Figure 3.5-b) while the current measured for BP11-MG electrode is approaching 25 μA at 0.3V (Figure 3.5-a), both experiments performed with 10 mM of NADH. Evenmore, comparing both curves with the BPMG-MG at 1600 rpm (RDE) and mantainning constant all other conditions, the graph shows an increment on the current measured to 225 μA at 0.2V on BPMG-MG (Figure 5-c), demonstrating the mass transport dependance of the oxidative process with respect to the electrode material design. The increment of the current measured with BPMG-MG demonstrates that the high amount of MG in this material induces a larger number of NADH oxidative reactions per surface area and unit time, but does not make the material a better condutor when compared to BP11-MG.

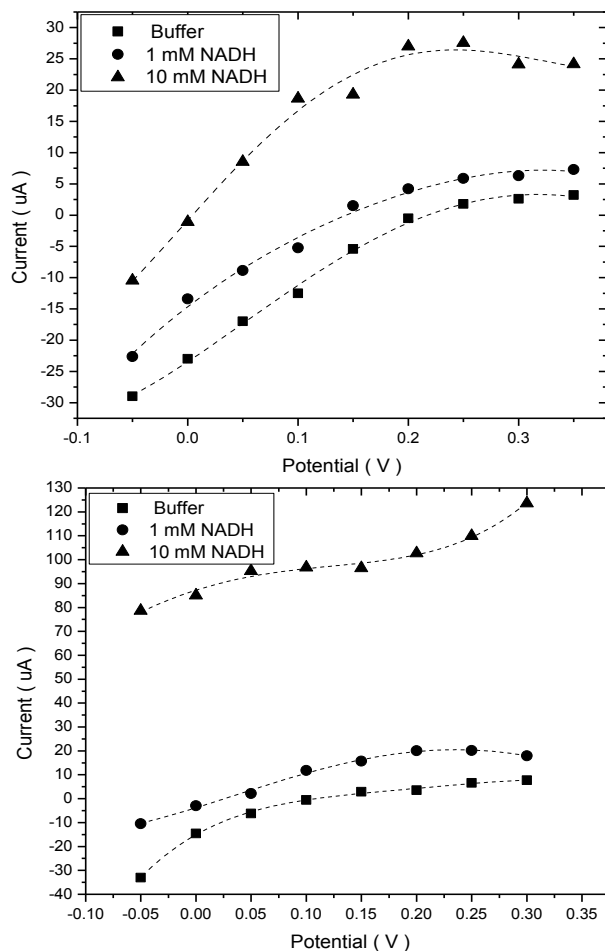


Figure 3.5. Hydrodynamic Polarization curves with Sodium Phosphate Buffer, NADH 1 mM and NADH 10 mM on a) BP11-MG Electrode , b) BPMG-MG Electrode and c) BPMG-MG RD Electrode at 1600 rpm

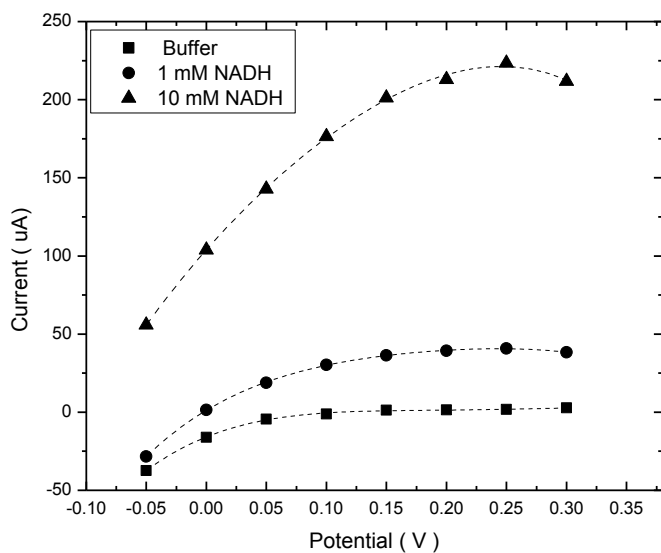


Figure 3.5. c) Hydrodynamic Polarization curves with Sodium Phosphate Buffer, NADH 1 mM and NADH 10 mM, BPMG-MG RD Electrode at 1600 rpm

Chronoamperometry with NADH

The chronoamperometric curves (Figure 3.6) were used to find the relationship of the current generated with respect to the concentration of NADH in the cell. The generated currents demonstrate there was a catalytic activity produced by the PMG on the surface of the “bucky” papers (BP11 and BPMG). An increasing stepped current was observed due to the catalyzed oxidation of NADH, which produced a shuttle of electrons when each NADH aliquot was added to the cell. The linear relationship shown in Figure 3.6 demonstrates that the system follows the 1st order Fick’s law within the range of concentration measured (0 to 6 mM NADH).

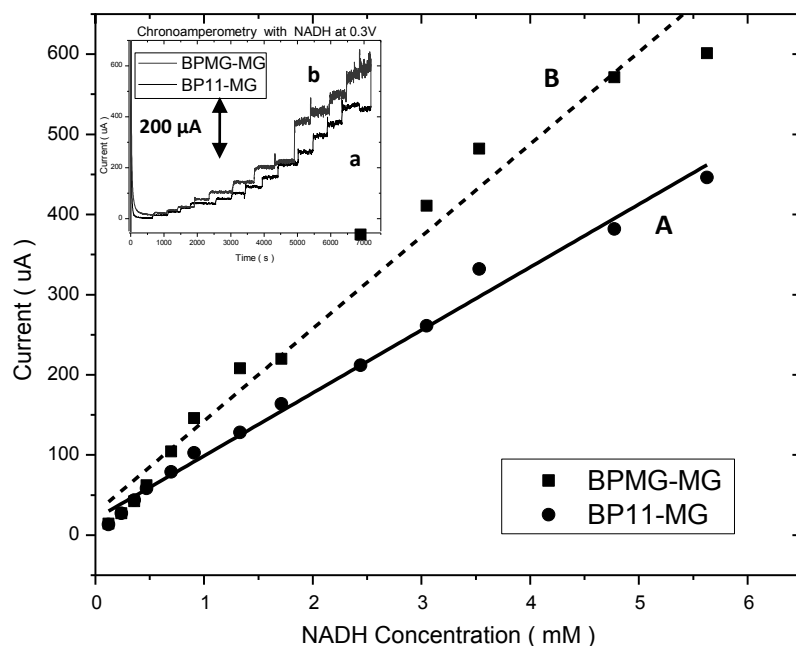


Figure 3.6. Relationship between Current generated and NADH Concentration (mM) on A) BP11-MG, B) BPMG-MG Electrodes found by Chronoamperometry with NADH on a) BP11-MG and b) BPMG-MG Electrodes. The 1st Fick's Law behavior is observed.

Chronoamperometry with MDH by additions of L-Malate

Chronoamperometric measurements were performed to evaluate the enzymatic activity of MDH in the presence of PMG electrocatalyst. After each consecutive addition of aliquots of 1M L-Malate (at steady state), the currents were recorded and plotted against the substrate concentration. Initially, in the cell, MDH and its diffusible cofactor NAD⁺ were in solution at a concentration of 0.5 mg in 50 µl of MDH and 10 ml of 10 mM NAD⁺ respectively. The enzyme shows a typical Michaelis-Menten behavior at 0.1 V potential (Figure 3.7). The Michaelis-Menten constant of MDH was found to be $K_M = 0.029 \pm 0.009$ M using the BP11-MG anode and $K_M = 0.028 \pm 0.003$ M using the BPMG-MG anode (Table 2). The maximum current generated are $I_{max} = 8.6 \pm 0.9$ µA for BP11-MG and $I_{max} = 7.4 \pm 0.3$ µA for BPMG-MG at the given conditions (Table 3.2). The

enzymatic process shows there are neither inhibitors nor competitive processes occurring in the substrate oxidation reaction.

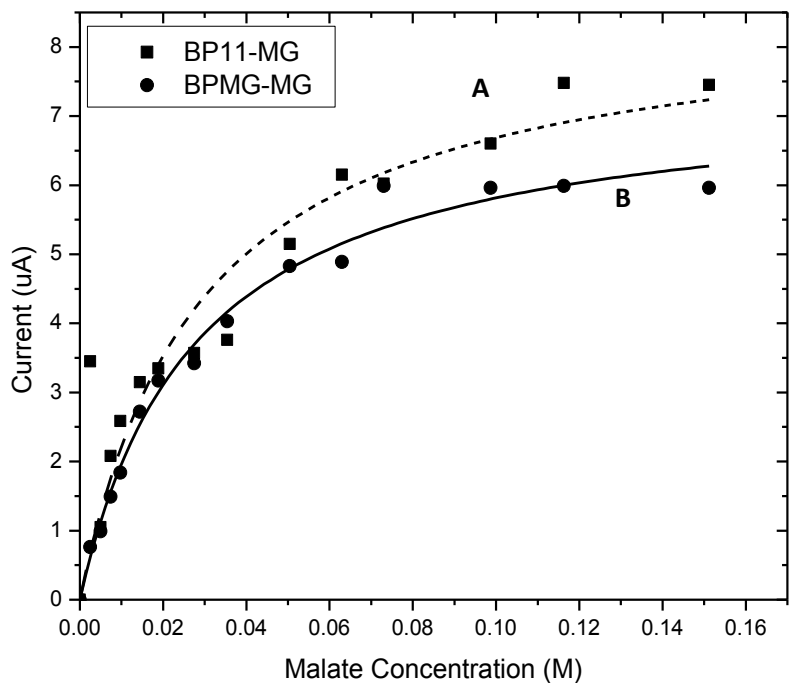


Figure 3.7. Relationship between Current generated and L-Malate Concentration (M) on A) BP11-MG (dashed line), B) BPMG-MG (solid line) Electrodes found by Chronoamperometry with MDH. Michaelis-Menten kinetics, there are neither inhibitors nor competitive processes.

Table 3.2. Michaelis-Menten parameters found by chronoamperometry of L-Malate with MDH

	$I_{max} (\mu A)$	$K_M (M)$
BP11-MG	8.6 ± 0.9	0.029 ± 0.009
BPMG-MG	7.4 ± 0.3	0.028 ± 0.003

3.2. Results and Discussion

Resistivity, Wettability and SEM imaging of “Bucky” Papers

BP11 showed a resistivity of 14.7 mΩ/ mg and BPMG 47.2 mΩ/mg; a copper (Cu) wire was used as a blank. As expected, both “bucky” papers show low resistivity demonstrating their high quality as conductor material for the design of our electrodes.

The SEM micrographs show how the strains of SWNTs effectively conferred a high surface area to the “bucky” papers and high porosity due to the bundles formed by the nanotubes (Figure 3.1). There were no treatment or conductive coatings performed on the samples prior to SEM observations. The combination of porosity provided by the SWNTs and hydrophilicity provided by the IPA conferred high wettability to the “bucky” papers. BP11 and BPMG were easily wetted but BPMG showed to be more hydrophilic than BP11 due to the presence of MG (highly hydrophilic and soluble in water). Due to their porosity and their hydrophilicity, both materials are fragile. Despite their fragility, they were easily used in the fabrication of these cavity anodes.

Methylene Green Electrodeposition

MG was deposited on the surface of the “bucky” papers by means of 10 voltammetric cycles within -0.5 V and 1.3 V at 5 mV/s of scan rate. The oxidative peak of MG is observed at 0.1 V in the first cycle and 0.2 V in the 10th cycle on both BP11 and BPMG papers for the static (not shown) as well as the RDE (Figure 3.2) electrodes. The displacement of the oxidative peak indicates that an oxidative polymerization is taking

place and more electroactive species are being deposited on the surface of the electrode. A background was also performed in this step using XC50-Carbon Black and XC50 (not shown). On both “bucky” papers, the MG electrochemical deposition generates a nucleation of PMG that results in the formation of particles observed on their surface by SEM imaging (Figure 3.3).

The EDS techniques were applied to corroborate the polymerization of MG was successfully performed. By SEM imaging, the particles of polymers are observed on the surface of the material (Figure 3.3) which shows a noticeable difference compared to the initial clean surface-material shown in Figure 1. The particles vary from 10~20 nm to 1 μ m (Figure 3.3, 1-b and 2-b) and are uniformly distributed on the “bucky” papers surface. Since electrolytic salts are used in the process of polymerization, it is logic to believe the nucleation observed may be due to the precipitation of electrolytes. Because of this reason, a further analytical study by EDS was performed applying a 10 KeV beam. For this analysis, the structure of the MG monomer was taken into account and from it, Sulfur (S) and Zinc (Zn) were traced on the BP11 surface (Figure 3.4). In this case, the presence of sulfur and zinc on the surface would demonstrate an effective polymerization because MG is the only source of them. The EDS spectrum demonstrated that MG was successfully deposited on the BP11 (Figure 3.4); Table 3.1 shows that sulfur constituted the 5.26% of the total deposited compounds to the BP11 paper surface as well as zinc (5.26%). BPMG is expected to have MG deposited on its surface as well since the same procedures were applied in its process. To corroborate these results and that no other compound was deposited, the “bucky” papers were subjected to cyclic voltammetry in a background solution without the MG monomer. These solutions contained the buffer and

KNO_3 in similar quantities than the MG growing solution. After exposing the material to 10 voltammetric cycles, the surface of the BP11 was analyzed through SEM imaging and EDS. SEM images showed that there was precipitation of electrolytes, there were sporadic formations of particles on the BP11 surface (not shown). However, the EDS analysis showed presence of neither sulfur nor zinc (spectrum not shown). The EDS shows that meaningless amounts of electrolytes in the growing solution precipitated on the “bucky” paper’s surface but PMG was successfully deposited (Figure 3.4). Further chronoamperometric measurements confirmed the MG polymerization on BP11 and BP-MG and show the PMG performance as mediator in the anodic process.

Hydrodynamic Polarization Measurements

By constructing a hydrodynamic polarization curve, the ideal working potential for NADH was determined for both BP11-MG and BPMG-MG electrodes. For the BP11-MG electrode, the working potential found was 0.3V (Figure 3.5.a); this was applied to perform chronoamperometric measurements for NADH. For a 10 mM NADH the current is proportionally increased with the concentration of NADH compared to 1 mM NADH and the buffer background. In Figure 3.5.b, the compositional material MG proved to induce an increment in the current generated at the same potential range of testing (-0.05 to 0.35 V). The current measured is approximately 95 μA at 0.2 V on BPMG-MG electrode (Figure 3.5.b) while the current measured for BP11-MG electrode is approaching 25 μA at 0.3V (Figure 3.5.a), both experiments performed with 10 mM of NADH. Evenmore, comparing both curves with the BPMG-MG at 1600 rpm (RDE) and

maintaining constant all other conditions, the graph shows an increment on the current measured to 225 μA at 0.2V on BPMG-MG (Figure 5.3.c), demonstrating the mass transport dependence of the oxidative process with respect to the electrode material design. The increment of the current measured with BPMG-MG demonstrates that the high amount of MG in this material induces a larger number of NADH oxidative reactions per surface area and unit time, but does not make the material a better conductor when compared to BP11-MG.

Chronoamperometry with NADH

The chronoamperometric curves (Figure 3.6) were used to find the relationship of the current generated with respect to the concentration of NADH in the cell. The generated currents demonstrate there was a catalytic activity produced by the PMG on the surface of the “bucky” papers (BP11 and BPMG). An increasing stepped current was observed due to the catalyzed oxidation of NADH, which produced a shuttle of electrons when each NADH aliquot was added to the cell. The linear relationship shown in Figure 6 demonstrates that the system follows the 1st order Fick’s law within the range of concentration measured (0 to 6 mM NADH). This means that the current measured is linearly dependent on the concentration of NADH which follows a first order diffusive gradient toward the electrode surface. The movement of NADH molecules is from the bulk of the electrolyte solution, region of higher concentration, toward the electrode surface or catalytic layer, region of lower concentration due to a consumption of NADH by the oxidation reaction.

Chronoamperometry with MDH by additions of L-Malate

Chronoamperometric measurements were performed to evaluate the enzymatic activity of MDH in the presence of PMG electrocatalyst. After each consecutive addition of aliquots of 1M L-Malate (at steady state), the currents were recorded and plotted against the substrate concentration. Initially, in the cell, MDH and its diffusive cofactor NAD⁺ were in solution at a concentration of 0.5 mg in 50 μ l of MDH and 10 ml of 10 mM NAD⁺ respectively. The enzyme shows a typical Michaelis-Mente behavior in a potential of 0.1 V. The enzyme is catalyzing the irreversible conversion of substrate to products at this potential and the rate of catalysis performed by the enzyme is dependent on the concentration of the substrate (Figure 3.7). The Michaelis-Menten constant of MDH was found to be $K_{Mapp} = 0.029 \pm 0.009$ M using the BP11-MG anode and $K_{Mapp} = 0.028 \pm 0.003$ M using the BPMG-MG anode (Table 2) (K_{Mapp} is apparent K_M). The maximum current generated are $I_{max} = 8.6 \pm 0.9$ μ A for BP11-MG and $I_{max} = 7.4 \pm 0.3$ μ A for BPMG-MG at the given conditions (Table 3.2). The enzymatic process shows there are neither inhibitors affecting the performance of the enzyme nor competitive processes or side process occurring during the L-Malate oxidation reaction. The behavior of the curve shows similarities to the Michaelis-Menten behavior reported in previous studies [102].

3.3. Conclusion on the Anode Design Performance

The new SWNTs materials, “bucky” papers, were satisfactorily fabricated and effectively applied to the design of a cavity bioanode and could be further used in the

development of a biofuel cell. The catalytic activity of PMG was observed during chronoamperometric measurements of oxidation at 0.3 V for NADH and 0.1 V for L-malate oxidation by MDH. The oxidation of the NADH by the catalytic activity of PMG follows the 1st Fick's Law at low concentrations. The Michaelis-Menten behavior of the enzyme shows no inhibition or competitive processes during the oxidation of the substrate and no processes affecting the electrodes performance. The oxidation and regeneration of NADH cofactor during the oxidation of L-Malate was satisfactorily catalyzed by PMG electrodeposited on the "bucky" papers' surface.

An improvement of the fabrication of the anode was achieved. The use of SWNTs in the material increase porosity and the surface area of the material providing an increase in the number of active sites of the catalyst per unit area and improving the mass transfer through the material. The interface interactions at the nanoscale for the reactions happening on the materials surface were improved. The components of the BP11 and BPMG (SWNTs, IPA and SWNTs, IPA and MG respectively) are well combined to give a conductive-hydrophilic-porous-manageable material for this cavity anode design. The incorporation of the MG monomer has effectively provided an increase of the number of oxidative NADH reactions, increasing the number of electrons shuttled to the cathode and showing an increase in measured current. The incorporation of the monomer into the material opens the door for improvement and would simplify the manufacturing process of the cavity anode material based in SWNTs. This research increased the understanding of the SWNT materials to enable biofuel cell electrodes with greater reproducibility and efficiency.

Chapter 4. MWNTs-Based “Buckeye” Paper and Teflonized Carbon Fiber- Based “Toray” Papers Integrated for Cathode Designs

Enzymatic biofuel (EBCs) cells oxidize organic fuels such as sugars, alcohols, fatty acids and amino acids among others to generate electrical energy. The cathode for such cell can be designed to mimic oxygen reduction existing in some living organism, some prokaryotes and eukaryotes. In this cathode, oxygen can be passively supplied from ambient air or dissolved in solution. The air-breathing biocathode consists of two layers: a hydrophilic-catalytic layer which is in contact with the biofuel solution and a hydrophobic air-breathing layer that prevents leaking of the biofuel solution and allows the oxygen mass transport by facing the ambient air (Figure 4.1) [98]. The liquid electrolyte cathode, in non-air-breathing mode, designed for implantable devices for example, should use oxygen dissolved in the fluids of the organism where the EBFC is implanted. This cathode needs to be tested with oxygen dissolved in the BFC.

The reduction of oxygen by multicopper oxidases (MCOs) is a 4-electron pathway, which are found in those organisms, and was used for cathode design in this research. These enzymes are found in eukaryotes and prokaryotes; those MCOs are laccase, ascorbate oxidase or bilirubin oxidase [5, 9, 51-53]. These show efficient DET with carbon electrode materials (i.e. carbon nanotubes, teflonized carbon powders) [61-66]. The MCOs active site is formed by four copper atoms classified as Type 1 (T1) a paramagnetic copper (Cu) and Type 2 (T2) and Type 3 (T3), diamagnetic Cu. One T2 and two T3 coppers form a trinuclear cluster center which is stabilized by a His-Cis-His tripeptide bridge (Figure 1.13). The MCOs enzymes show different redox potentials due

to the different distance of the His-Cis-His tripeptide bridge to the T2/T1 and T3 Cu. This research was performed using fungi MCOs: Laccase from *Trametes versicolor* and Bilirubin oxidase from *Myrothecium verrucaria*. Laccase was used in the design of an air-breathing cathode since its catalytic activity is inhibited at physiological conditions (0.14 M NaCl, pH 7.41) [9, 61, 99] and non usable for implantable devices; chloride ion (Cl^-), found in living organism, inhibits the enzyme activity. In order to design an implantable device, BOx was utilized; this enzyme is not inhibited by Cl^- and shows activity at near neutral pH.

The immobilization techniques applied for both designs depend on the application of the BFCs. For implantable devices the immune response of the organism to the elements present in the BFC is a prevailing factor when choosing the immobilization technique of the enzyme. One doesn't want to have toxic compounds to be part of the design. In the design of a BFC for portable devices, there is no body-immune response issue and the applicability of a wide range of linking agents or enzyme immobilization techniques can be considered. The immobilization techniques applied in this research were thought to overcome enzyme stability barriers and to promote DET. Laccase was immobilized on BEP (Buckeye paper, a MWNTs-based paper) by a linking agent (PBSE) forming the catalytic layer, and later assembled with a TP30 (60% teflonized Toray paper, with thickness of 0.11mm), the hydrophobic layer, to conform an air-breathing cathode for a stack cell. BOx was immobilized in a silica-gel matrix on TP90 (60% wt teflonized Toray paper, with thickness of 0.28mm) and was tested in an electrolytic cell with saturated O_2 in solution.

4.1. Buckeye and Toray Papers Integration for an Air-Breathing Cathode Design

In the cathode, the electrons transferred from the anode have to meet an electron acceptor to allow the electrical current to flow continuously. The oxygen reduction reaction (ORR) is subject to the availability of oxygen on the catalytic layer. The design of an air-breathing cathode has to facilitate oxygen transport through the hydrophobic layer. Oxygen will meet the flux of electrons, the enzyme active site and hydrogen protons in solution in a three-phase interface to produce water (Figure 4.1.a). The interaction of the active site of the enzyme and the electrode surface has to overcome the electron transfer barrier; for this to happen, the material has to be very conductive and the enzyme has to be well oriented toward the electrode surface. Additionally, this catalytic layer has to be in contact with the electrolytic solution that transports H^+ in order to allow the formation of water molecules when oxygen is reduced. As a consequence, the enzyme immobilization technique needs to help the active site-oxygen-protons interaction with the electrode surface. Thus, the design has to be formed by a catalytic layer that is hydrophilic enough to transport H^+ within the layer where oxygen will meet the active site and electron to react (Figure 4.1.a). In order to overcome these necessities, the 3-D structure of the enzymes has to be preserved to assure the active site will catalyze the reaction and will do it for a long period of time. Thinking about all the requirements mentioned above for an air-breathing cathode, in this research, we used a crosslinking agent on BEP to design the catalytic layer and assembled this with two hydrophobic layers made from Nickel mesh and 50% teflonized carbon black (Ni/XC50), first, and TP30, secondly. Both electrodes were tested in a stack cell design (Figure 4.1.b).

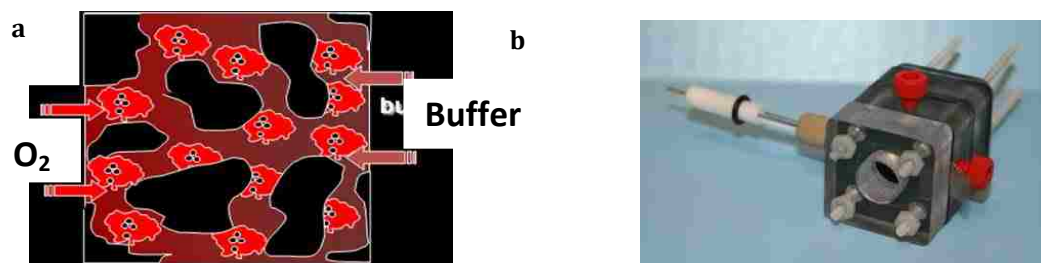


Figure 4.1. a) Air-breathing Cathode Design, b) Air-breathing Stack Cell (both from Carolin Lau's presentation on Air-breathing Cathodes)

4.1.1. Experiments and Methods for Air-Breathing Cathode Characterization

Apparatus

The electrochemical experiments were performed in a three-electrode cell by conventional potentiostats: Gamry Reference 600 Potentiostat/Galvanostat/ZRA and Princeton Applied Research VersaSTAT 3 potentiostat / galvanostat. All potentials are reported vs. Ag/AgCl reference electrode. The material characterization was performed using a Scanning Electronic Microscope Hitachi (S-5200).

Materials

Buckeye paper was obtained from Buckeye Composite Inc. 60% Teflonized Toray Paper thickness of 0.11 mm (TP30) was obtained from Toray Industries Inc. Isopropanol (purity > 99%), Monobasic and Dibasic Sodium Phosphates were obtained from EMD Chemicals Inc. Phosphates were used to prepare the pH 6 phosphate buffer stock solution. Laccase, DMSO, and PBSE were obtained from Sigma (St. Louis) and used without further purification. Laccase was dissolved in DMSO in proportion 4mg/1ml.

MWNTs-Based Paper, “Buckeye” Papers

The manufacturer reports the BEP is made from plain MWNTs; no treatment is performed on the nanotubes. Non-covalent interaction between the sp^2 orbital of the singular MWNTs form π - stacking bonds and maintain the nanotubes together in a whole piece alike to a paper. These MWNTs provide high thermal and electrical conductivity to the material and shows to have high strength and be very handable. The resistivity measured for the material was very low, in the range of 3.5-4.5 Ω , thus the BEP is very conductive.

The material showed to be highly hydrophobic. Once it was treated with PBSE, it showed to be more hydrophilic (Figure 4.2). SEM images show the material has a very high surface area and high porosity that would improve enzyme loading and enzyme-electrode surface interaction (Figure 4.3). From the SEM images, it is observed that the diameter of the MWNTs ranges between 10 nm and 30 nm approximately. In the image of the edge of the material, it is important to note that the bundles of MWNTs are more or less oriented (Figure 4.3.b), this will facilitate the conductivity or electron transfer.

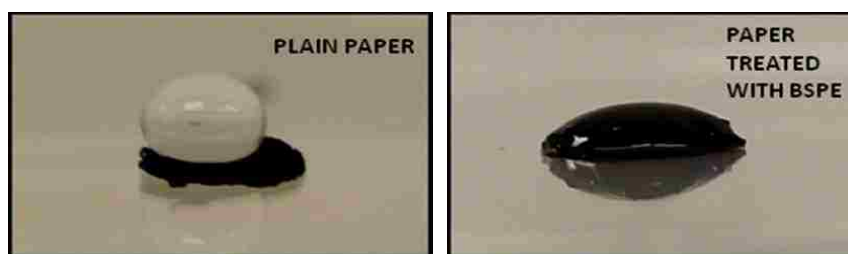


Figure 4.2. a) BEP without surface treatment, b) BEP treated with PBSE

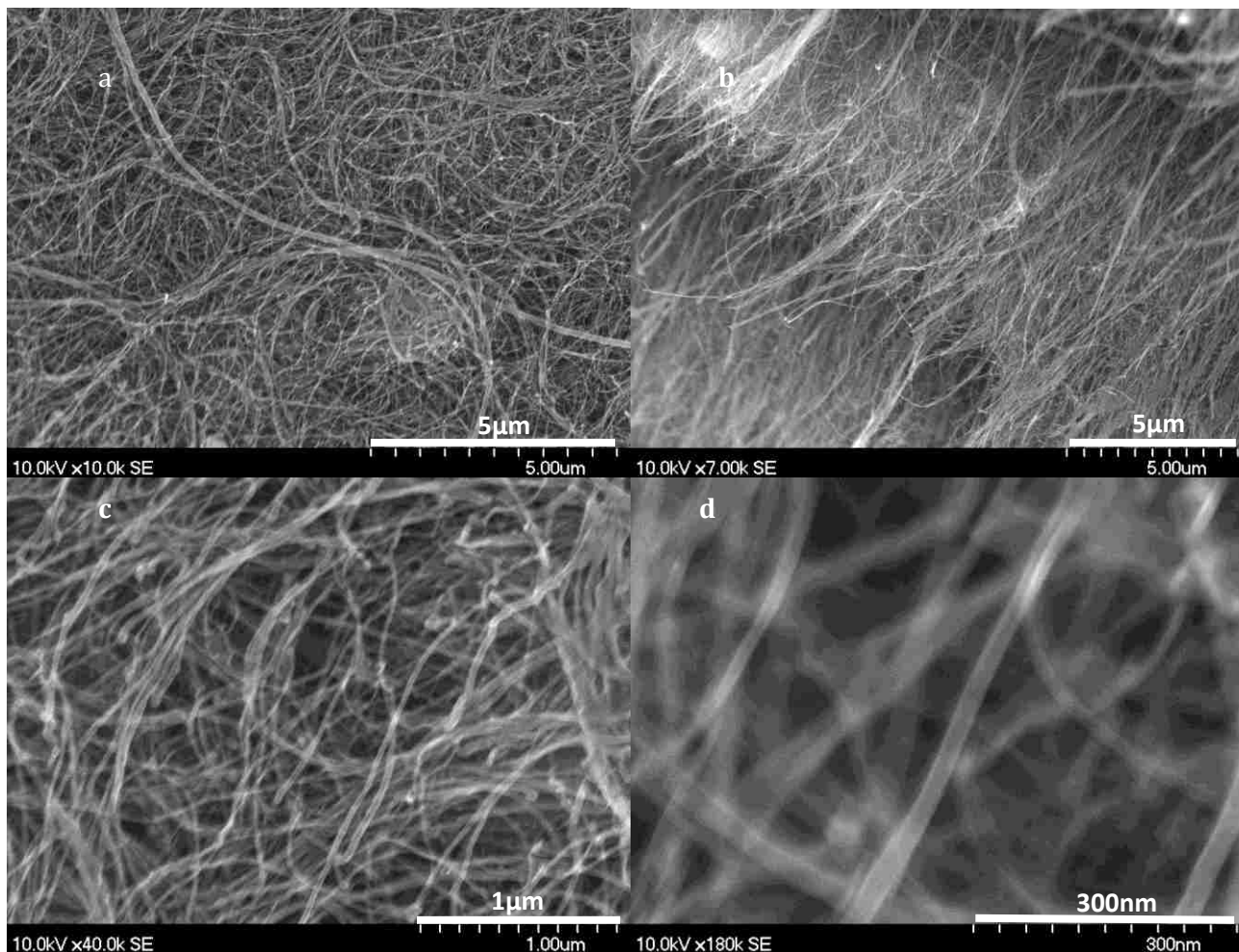


Figure 4.3. BEP without farther treatment

Laccase Enzyme Immobilization for a Three-Phase Interface Cathode Design

Immobilization experiments were performed using 50 % teflonized carbon black (XC50) compacted on nickel mesh and TP30 as the air-breathing hydrophobic layer and BEP, as the catalytic electrode material. Laccase is immobilized on the surface of BEP by pyrene butanoic acid succinimidyl ester (PBSE), a crosslinking agent. Laccase attaches to the succinimidyl group of the PBSE which in turn attaches to the graphite ring of the BEP (Figure 4.5). PBSE interacts optimally with BEP; its planar pyrene ring has shown

efficient sp^2 hybrid orbital interactions with the MWNT due to low curvature of the graphite rings within the MWNTs structure (Figure 4.4).

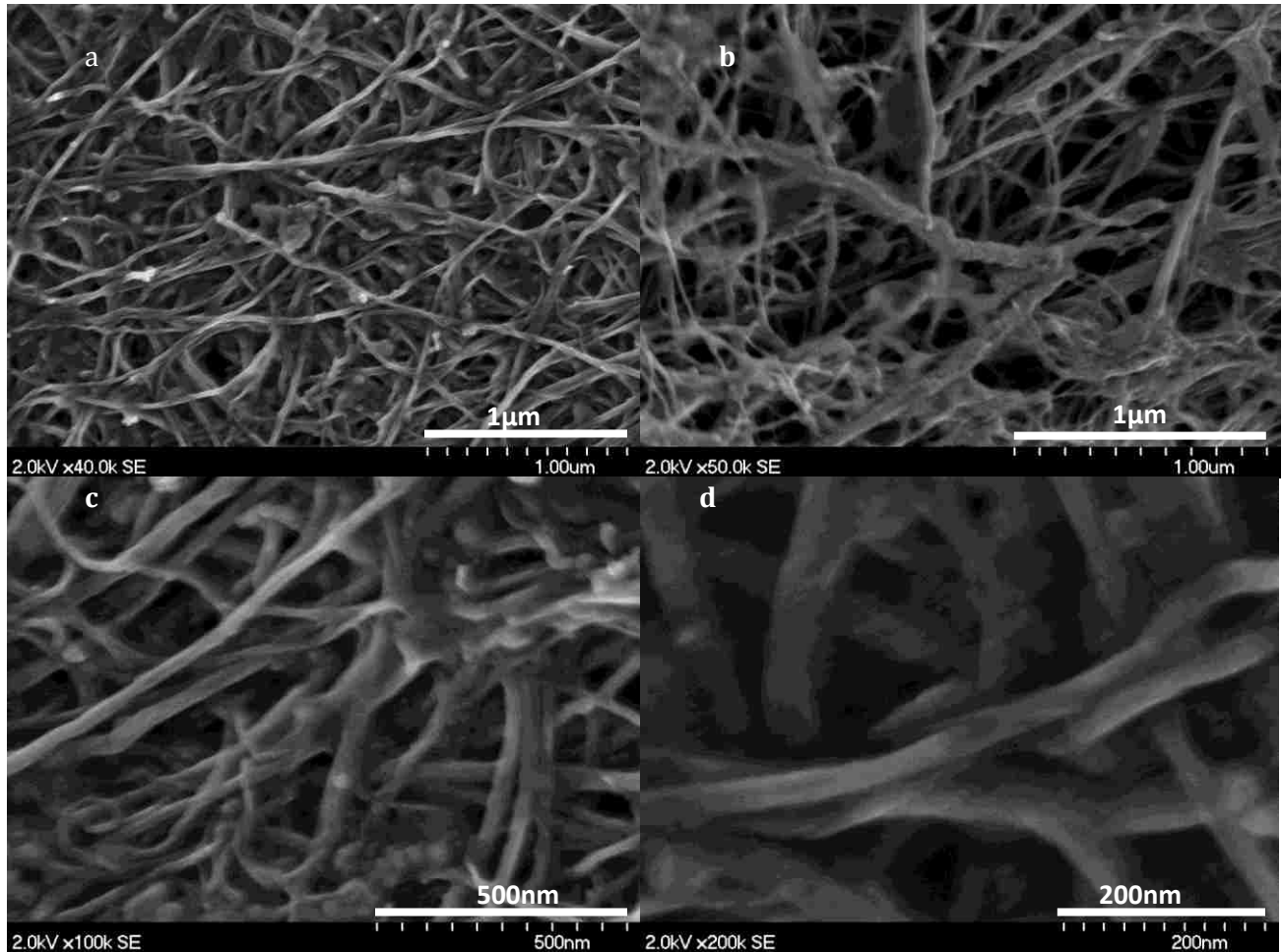


Figure 4.4. BEP, PBSE and Laccase deposited on the surface forming a film

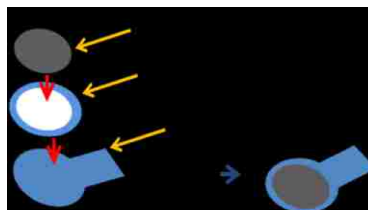


Figure 4.5. TP30/BEP setup for stack cell. BEP was previously treated with PBSE and Laccase was deposited overnight

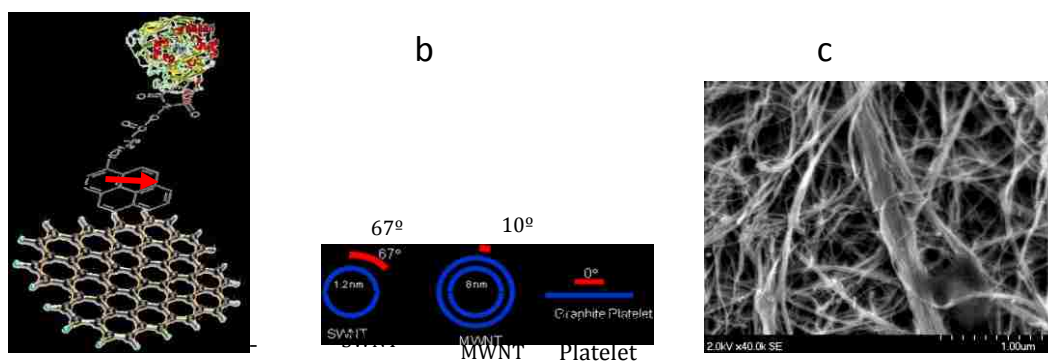


Figure 4.6. Laccase immobilization on BEP, a) PBSE/BEP interaction, b) Curvature of the interacting surface , c) BEP SEM Image. (source: a) and b) Chen, R. J., Y. Zhang, et al)

Stack-Cell Air-Breathing Cathode

Initially, a piece of BEP was pressed on top of XC50 on Ni mesh. 10 kPsi of pressure was applied in this process. Later, 200 μ l of PBSE diluted in DMSO (proportionally 4 μ g /ml, respectively) was deposited on top of the electrode for 1 hour. After this, the electrode was washed 3 times with DMSO and 3 times with phosphate buffer (pH 6). Subsequently, 200 μ l of Laccase/phosphate buffer was deposited on the electrode and left it overnight. The Laccase solution was obtained from dissolving 4 mg of Laccase in 1 ml of the 0.1 M phosphate buffer (pH 6). The first cathode, Ni/XC50/BEP/PBSE/Laccase, was created.

Secondly, further studies were performed to evaluate TP30 as hydrophobic material for the cathode design. These tests were developed under similar electrolytic conditions of the previously mentioned experiments. TP30 was selected because of its high conductivity, hydrophobicity, high porosity and low thickness. In these experiments, Ni mesh and XC50 were replaced by TP30. Due to the fragility of the material no high pressing step was applied; the setup of the material consisted in fixing the piece of

BEP/PBSE/Laccase on top of TP30 piece and within a TP30 ring (Figure 4.5). There is no teflonized carbon or any adhesive between the materials but bare material contact. This was achieved by fixation of the materials with the pressure applied by the cell assemble process. It is expected not to have air between the layers and later proved by OCV measurements. Then, second cathode, TP30/BEP/PBSE/Laccase, was created and submitted to electrochemical tests.

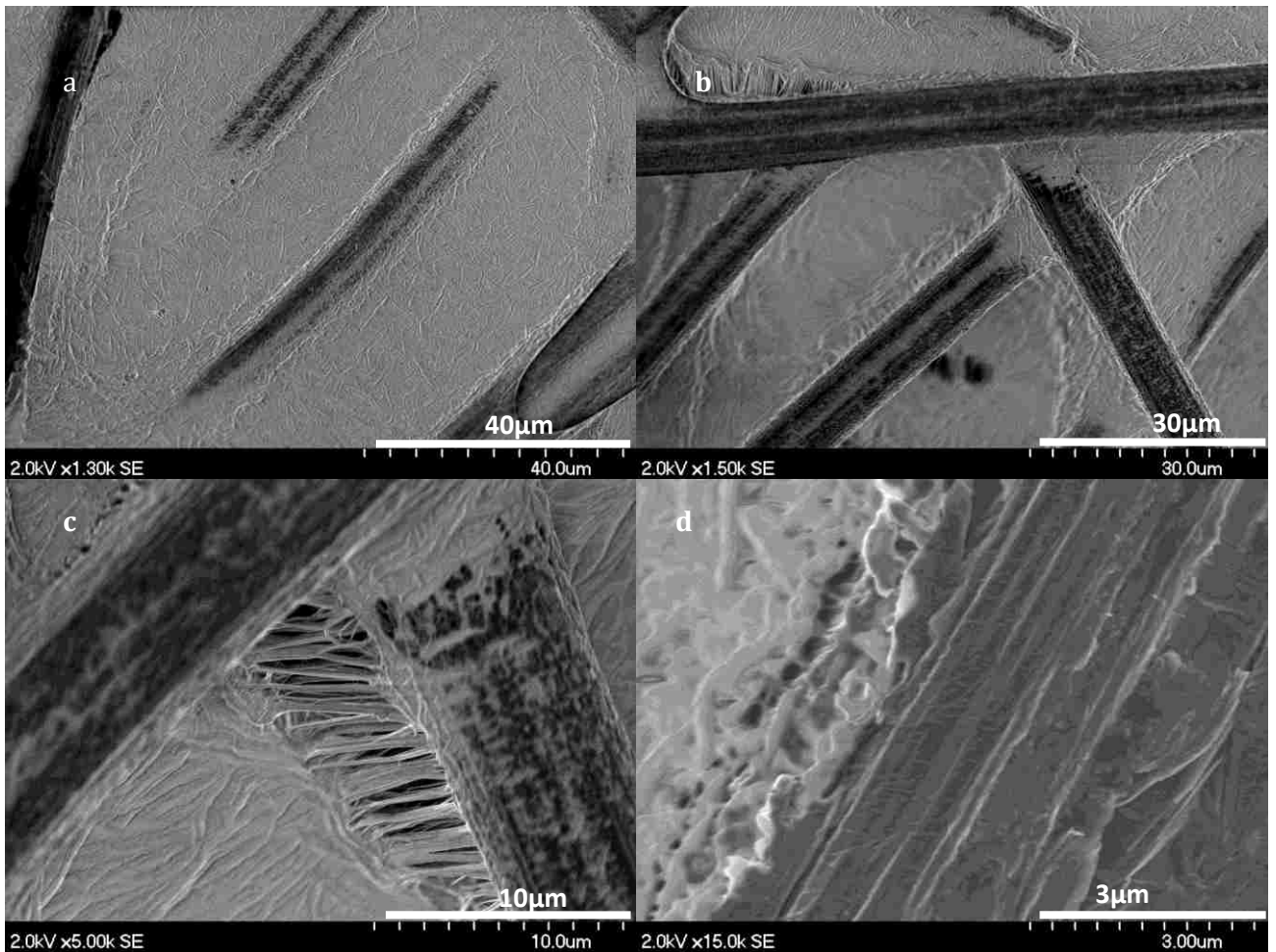


Figure 4.7. TP30, 60% Teflonized Carbon Fiber, 0.11 mm Thickness. The porosity of the material allows for a three phase interface interaction

Open Circuit Voltage to Evaluate the Gas Diffusion Layer of the Cathode Design

The cathodes fabricated by employing PBSE as a crosslinking agent for Laccase immobilization on BEP were tested electrochemically to evaluate their performance toward ORR. The firsts electrochemical tests were open circuit voltage measurements (OCV) (Figure 4.8). The cathodes used were Ni/XC50/BEP/PBSE/Laccase and TP30/BEP/PBSE/Laccase in an electrolytic cell with 0.1M phosphate buffer at pH 6. These experiments were performed in two situations: applying a flux of oxygen toward the air-breathing face of the cathode and without applying any oxygen.

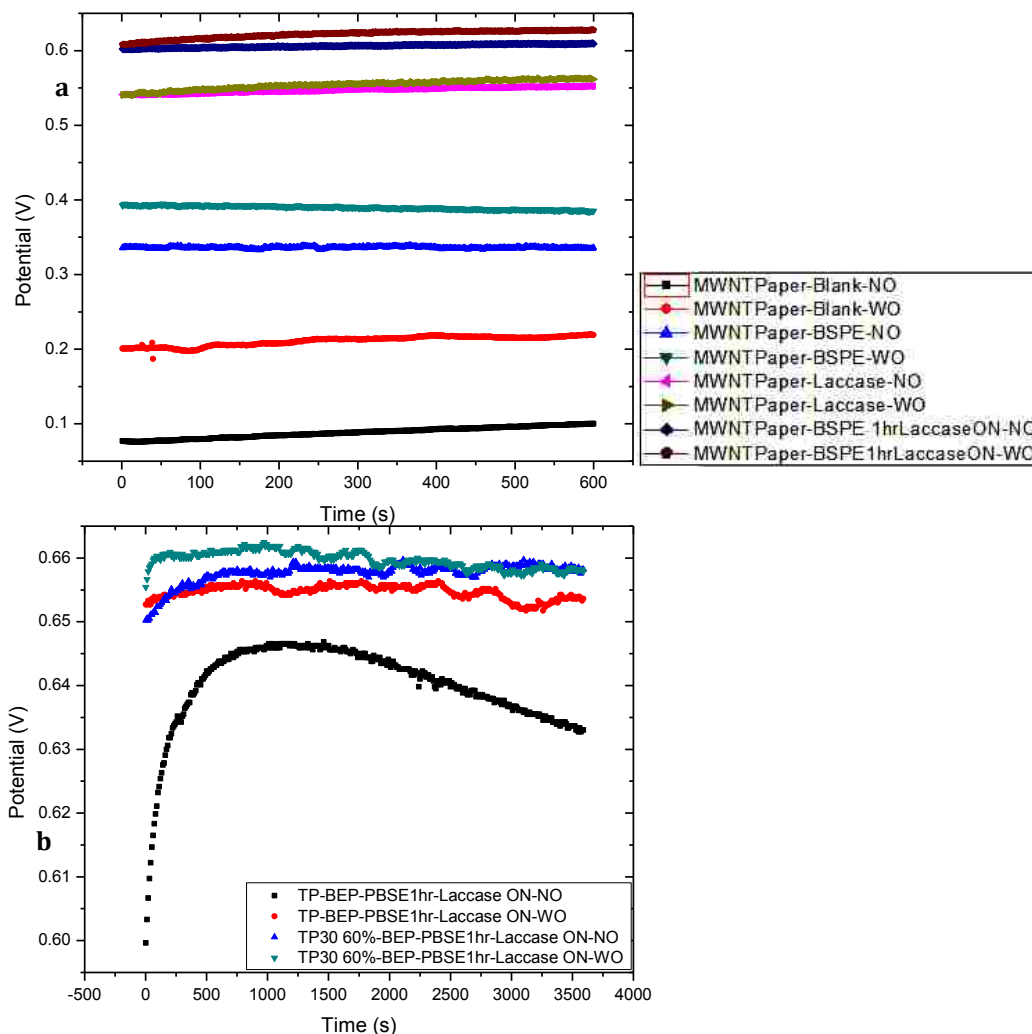


Figure 4. 8. Open Circuit Voltage for a) Ni/XC50/BEP/PBSE/Laccase cathode, b) TP30/ BE/PBSE/Laccase and TP90 (called just TP)/BEP/PBSE/Laccase cathodes (ON-Overnight, NO-No Oxygen was supplied to the cell, WO-With Oxygen supplied to the cell). In all cases, except blanks, PBSE was deposited for 1hr and Laccase was deposited overnight

Cyclic Voltammetry for the ORR Performance

These experiments were developed in a 3 ml stack cell where the biocathode is exposed to air (Figure 4.9) and the electrolytic solution is phosphate buffer (pH 6). A multiple cyclic voltammetry between -0.2 V and 0.8 V at a scan rate of 10 mV/s (Figure 4.9), 20 mV/s and 50 mV/s (not shown) were performed. Additional background tests were performed to evaluate the performance of the bare BEP material. The background electrodes were BEP/PBSE and BEP/Laccase at similarly experimental conditions.

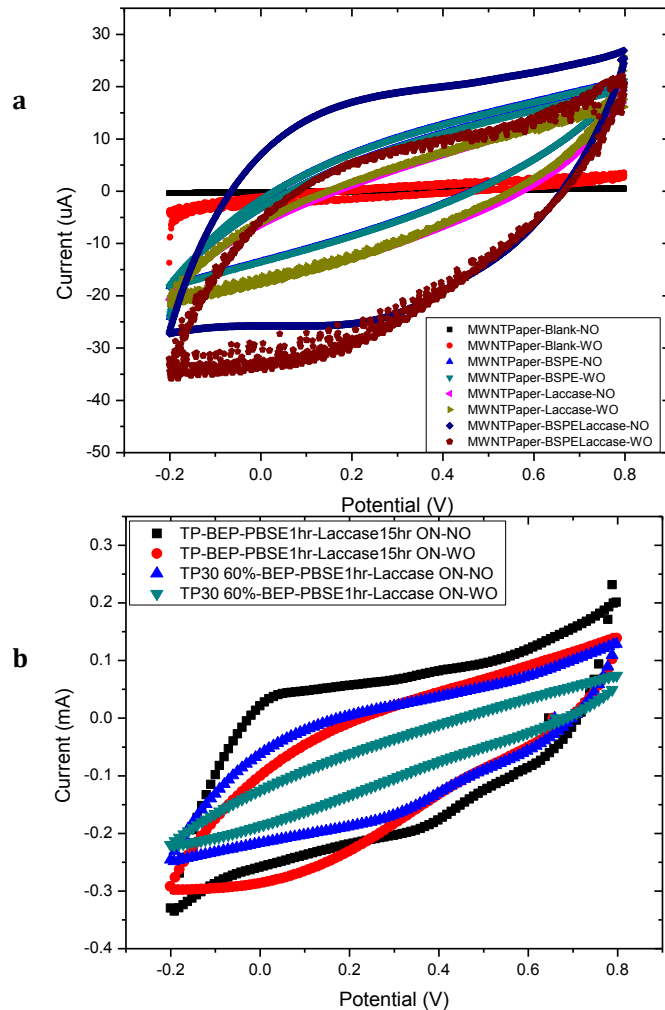


Figure 4.9. Cyclic Voltammograms for a) Ni/XC50/BEP/PBSE/ Laccase, b) TP30/BEP/PBSE/Laccase and TP90 (called just TP)/BEP/PBSE/Laccase cathodes at a scan rate of 10mV/s in PB at pH 6. (ON-Overnight, NO-No Oxygen is supplied to the cell, WO-With Oxygen supplied to the cell). In all cases, except blanks, PBSE was deposited for 1hr and Laccase was deposited overnight although in some insets it was omitted.

Potentiostatic Polarization Curves for the Air-Breathing Cathode Performance

Chronoamperometric measurements were taken, currents were measured while controlled potentials were applied, The resulting currents at quasi-steady state were plotted against their respective potentials (Figure 4.10).

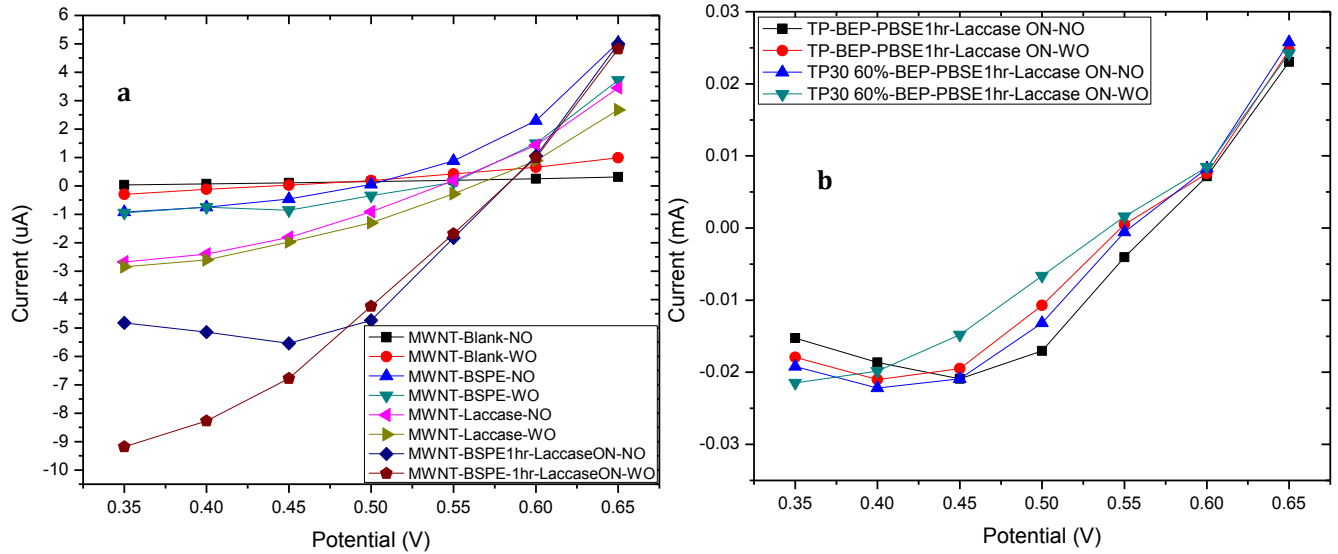


Figure 4.10. Potentiostatic Polarization Curves for a) Ni/XC50/BEP/PBSE/Laccase, b)TP30/BEP/PBSE/Laccase, and TP90 (called jus TP)/BEP/PBSE/Laccase cathodes (ON-Overnight, NO-No Oxygen was supplied to the cell, WO-With Oxygen supplied to the cell) In all cases, except blanks, PBSE was deposited for 1hr and Laccase was deposited overnight

4.1.2. Results and Discussion

Open Circuit Voltage to Evaluate the Gas Diffusion Layer

For the first cathode setup, Ni/XC50/BEP/PBSE/Laccase, the OCV graph shows that cathode approached the theoretical redox potential for Laccase at approximately 0.62 V with and without supplying oxygen to the cell toward the air-breathing face of the electrode (blue and maroon lines, respectively, in Figure 4.8.a). For the second cathode setup, TP/BEP/PBSE/Laccase, the OCV graph shows that the air-breathing cathode

approaches a potential of 0.66 V, 40mV more than the first setup, when applying and without applying oxygen to the breathing layer (blue and light green lines in Figure 4.8.b). There is no a considerable difference between the OCV curves when oxygen is supplied and when it is not. These results suggest us that the second cathode setup is not starving from oxygen but it is capable of feeding itself since there is no oxygen mass transport limitation.

Cyclic Voltammetry for ORR

Cyclic voltammograms were performed on both cathodes setups, Ni/XC50/BEP/PBSE/Laccase and TP30/BEP/PBSE/Laccase. The CVs experiments showed an increase in the width of the cycle respect to the background tests demonstrating an increase in the charge transferred for both electrodes with respect to their backgrounds. In Figure 4.9.b, TP30/BEP/PBSE/Laccase cathode shows an order of magnitude higher of current measured for the same potential range. These results show that the charge transferred is much higher when compared to the first setup, and the concentration of the active Laccase or the Laccase which is catalyzing the ORR is also higher, according to the equation $\Gamma = Q/nFA$ (where Γ =surface concentration of Laccase, Q=charge transferred from integrating the anodic and cathodic peaks from the CVs, F=Faraday constant, n=number of electron per enzyme (4), and A= electrode surface area).

At this point, it is assumed that no air is between the TP30-BEP materials. To prove this is true, a much thicker Toray paper (60%teflonized Toray paper with 0.19 mm, TP) was employed in the OCV and CVs measurements. Later, the data was compared to

the previous results with TP30/BEP/PBSE/Laccase setup. As a remainder, we have to consider that while the hydrophobic layer increases its thickness, the passive oxygen supply by air breathing decreases, thus increasing the oxygen starvation in the cell. In this situation, oxygen should be fed to the cell to avoid starvation. Then, in the experiments with the TP/BEP/PBSE/Laccase setup, the OCV curve shows its maximum value at about 0.645 V potential which decreases to 0.63 after 1 hr when oxygen is not supplied (black line in Figure 4.8.b). However, the OCV curve shows a potential ~ 0.652 V and it is constant after 1 hr since oxygen is continuously applied to the breathing layer (blue line in Figure 4.8.b). These results demonstrated that no air is stored between the materials or layers, TP-BEP or TP30-BEP, since the OCV curves are subjected to changes in the TP-BEP setup because its thickness, this limits the oxygen mass transport to the catalytic layer. Also, the OCVs for TP30-BEP show to be independent of oxygen fed into the cell since it is mostly constant in both situations (supplying oxygen and without supplying oxygen). This led us to conclude that the open circuit potential observed in TP30/BEP/PBSE/Laccase cathode was due to the passive transport of oxygen through the air breathing layer. TP30/BEP/PBSE/Laccase works ideally as air breathing layer and TP30 shows to be a very conductive material.

Potentiostatic Polarization Curves and Power Curves

The polarization curves show the performance of the cathodes at potentiostatic mode. The Ni/XC50/BEP/PBSE/Laccase electrode shows a current density of $\sim 5\mu\text{A}$ for 0.65 V (\sim the OC potential) in Figure 4.10.a, while TP30/BEP/PBSE/Laccase electrode has a current density $\sim 0.025\text{mA}$ ($25\mu\text{A}$) (Figure 4.10.b) and a power density of $\sim 0.20\mu\text{W}$

for the same potential (0.65V) if we consider the anodic potential no greater than 0V. Also, at different potentials, the TP30/BEP/PBSE/Laccase shows to be independent of oxygen active transport (Oxygen is actively fed). In the other hand, the behavior of the Ni/XC50/BEP/PBSE/Laccase shows to be dependent on the feeding of oxygen to the cell. These results allow us to concluded that the TP30/BEP/PBSE/Laccase cathode could be used for air-breathing cathode design for future enzymatic BFC. However, the stability and performance of the enzyme need to be analyzed more in depth. Trying a different method of immobilization for Laccase may help to improve the performance of the cell. Also, the ensamble of the cell could be improved by using a porous adherent layer between TP30 and BEP materials.

4.1.3. Conclusion for the Air-Breathing Cathode

Experiments demonstrate TP30 could be successfully used as the air-breathing layer in the cathode design. In the TP30/BEP/PBSE/Laccase cathode design, oxygen is passively supplied to the cell. The material allows oxygen mass transfer by the porosity of the material. These properties make this material optimum to use in DET oxygen reduction catalyzed by MCOs. TP30/BEP/PBSE/Laccase and Ni/XC50/BEP/PBSE/Laccase have redox potential approaching the theoretical potential for the Laccase enzyme, 0.66 V and 0.62V respectively. The formation of a PBSE-Laccase film is observed on the BEP material by SEM imaging which demonstrates true the theory of interaction of BPSE with the MWNTs ring (due to curvature close to the graphite rings curvature). The TP30/BEP/PBSE/Laccase cathode shows better performance at potentials close to the OCV (0.65V) than the Ni/XC50/BEP/PBSE/

Laccase cathode. The cathode performance did not accomplish the expected work output; the reason may be due to a low active site-electrode interaction and enzyme stability. It may be possible to improve the TP30-BEP layers interaction by applying a porous adherent material in the assembly of the cathode. Also, using a different enzyme immobilization technique could help for enzyme-electrode interaction and enzyme stabilization. These results open the possibilities to engineer an air-breathing layer for a cathode design utilizing TP30 and BEP composite materials.

4.2. Toray Paper Integration for a Liquid Electrolyte Cathode Design

In an enzymatic biofuel cell, the reduction of oxygen to form water can be performed in the cathode. In implantable devices, oxygen can be supplied by the fluids or blood of the organism where the BFC is implanted. In lab tests, oxygen is supplied by pumping oxygen to an electrolytic cell solution at physiological conditions of electrolytes concentration and pH. In this case, MCOs can also be employed. Herein, there is no need to have an air-breathing or hydrophobic layer. One can focus in the design of the catalytic layer to work in physiological conditions (0.14 NaCl, pH 7.41), and the immobilization and stability of the enzyme. Then, BOx was chosen for this design because previous studies have proven that the enzyme works at higher pH than Laccase and is not inhibited by the anion chloride (Cl⁻) as Laccase does [61, 99]. This research made use of enzyme silica-gel entrapment by CVD since this technique was successfully applied in previous studies [62, 70, 77-78]. By applying this technique, the catalytic activity and the 3D structure of the enzyme is expected to be maintained. The objective of this research is to create a cathode by entrapment of BOx through CVD of silica-gel on the electrode to achieve the catalysis of the ORR at physiological conditions (0.14 M NaCl, pH 7.41, and 37°C). Additionally, it is expected to prolong the enzyme lifetime for at least a month by applying this enzyme immobilization technique.

4.2.1. Experimental and Methods to Evaluate the Liquid Electrolyte Cathode

Apparatus

The electrochemical experiments were performed in a three-electrode cell by conventional potentiostats: Gamry Reference 600 Potentiostat/Galvanostat/ZRA and Princeton Applied Research VersaSTAT 3 potentiostat / galvanostat. All potentials are reported vs. Ag/AgCl reference electrode. The material characterization was performed using a Scanning Electronic Microscope Hitachi (S-5200).

Chemicals for Liquid Electrolyte Cathode Design

Teflonized 60% Toray paper 0.28 mm thick (TP90) was obtained from Toray Industries Inc. Isopropanol (purity > 99%), Monobasic and Dibasic Sodium Phosphates were obtained from EMD Chemicals Inc. and were used to prepare the pH 7.41 phosphate buffer stock solution. TMOS was obtained from Sigma (St. Louis, MO).

Teflonized 60% Toray Paper (TP90)- 0.28 mm Thickness

SEM images show the material TP90 has a large surface area and high porosity (Figure 4.11). The manufacturer of TP30 reports the material has a resistivity of 80 m Ω through the plane and 5.6m Ω in the plane. The porosity was reported to be 80% with a thickness of 0.28mm. The SEM images show the carbon fibers have a diameter approximately to 5-10 μ m and that they are joined by a Teflon film.

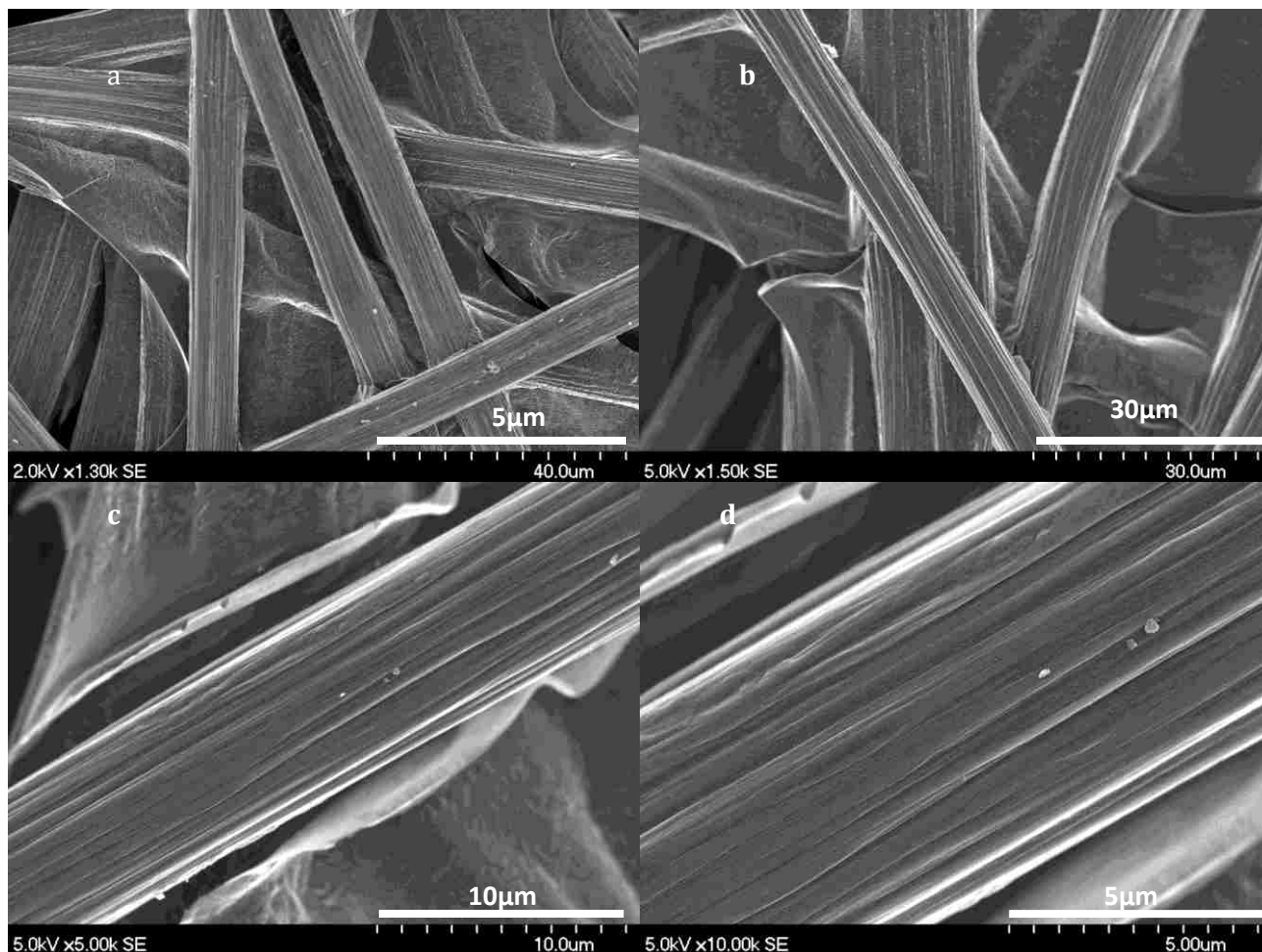


Figure 4.11. SEM images of TP90, 60% teflonized carbon fiber “Toray” Paper, 0.28 mm Thickness

Bilirubin Oxidase Enzyme Immobilization for ORR

Enzymes were trapped in a very porous silica-gel matrix which was designed to be thinner enough to allow electrode surface-electrolytic solution interaction. The formation of the silica-gel matrix is produced by polymerization of the TMOS precursor in solution as it was stated early in the immobilization techniques. The solution in this case is the physiological solution in which the enzyme was dissolved. The presence of electrolytes accelerates the polymerization process.

Cap Cathode Design for a Liquid Electrolytic Cathode with Immobilized BOx

The cap glassy carbon electrode was chosen for the tests. A 4cm x 4cm-piece of TP90 was treated with IPA and washed with PB at pH 7.41. Then, 200 μ l of BOx solution was deposited on the sample and left to rest overnight at 4°C in a centrifuge tube (~500 rpm). The BOx solution was made by dissolving 4mg of BOx enzyme in 1ml of 0.1M PB, 0.14 M NaCl buffer at pH 7.41. Next, the humid sample was placed in a CVD chamber formed by two bottom lids of petri dishes. Later, 50 μ l of TMOS precursor was deposited in a cap of a microcentrifuge tube and placed into the chamber next to the TP90 sample (See schema in Figure 4.12). Then, the lids were closed and sealed with parafilm and allowed to react for 10 minutes at room temperature (~25°C). After that time, the TMOS precursor was removed from the chamber and the TP/BOx/Silica-gel sample was saved at 37° C as stock electrode for later electrochemical experiments. This stock electrode was kept to be used for various experiments during a month period (Figure 4.13). The experiments were performed using a glassy-carbon cap electrode design. For each testing, a piece of TP/BOx/silica-gel was cut from the stock. The tests were programmed to be daily for a week and then once weekly and, finally, monthly.

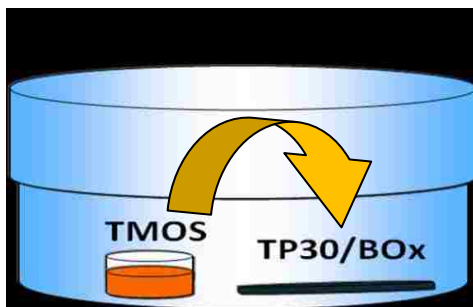


Figure 4.12. Chemical Vapor Deposition Chamber for silica-gel formation

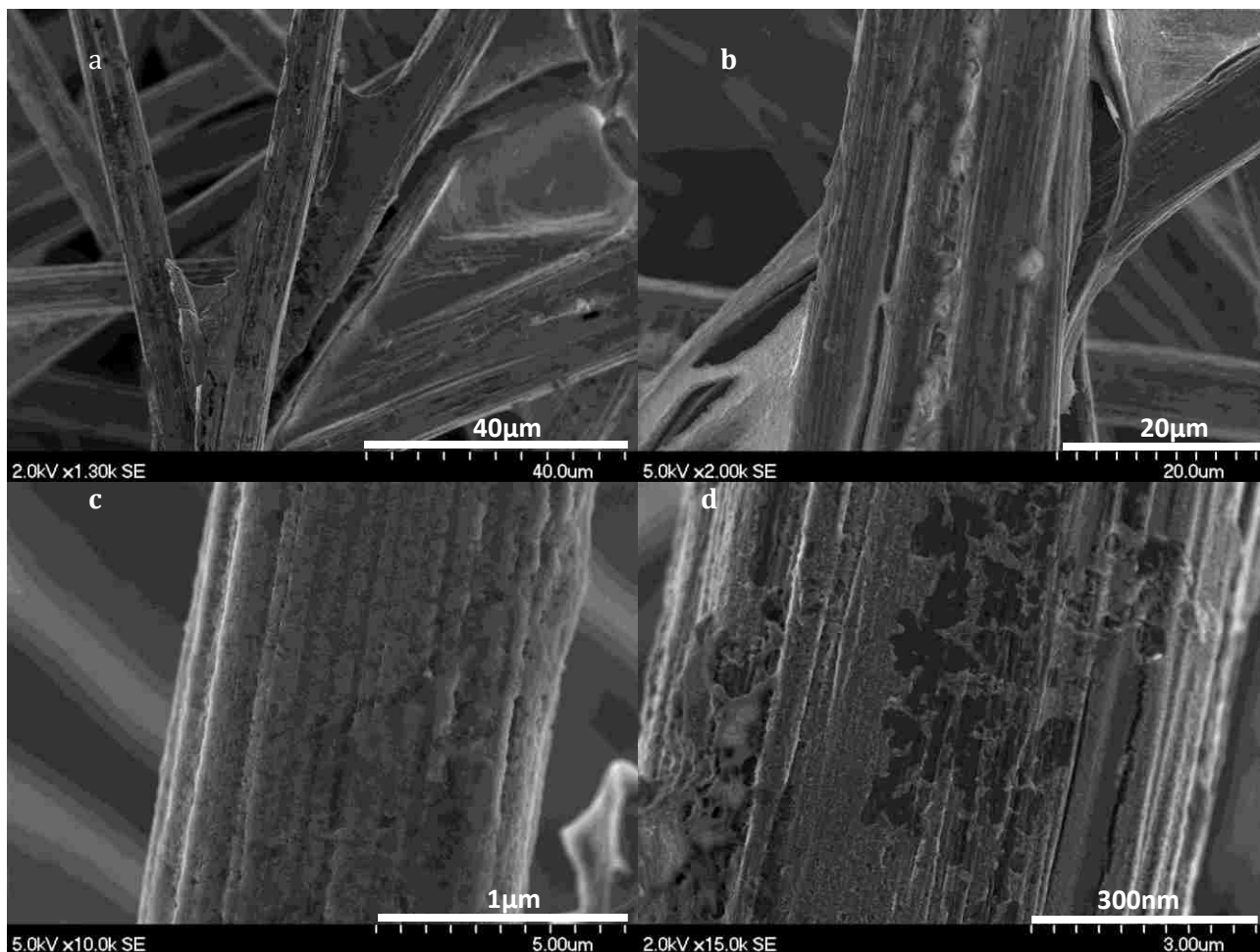


Figure 4.13. SEM images of TP90, after enzyme immobilization by Silica-gel entrapment with a time of exposure of the electrode to the precursor (TMOS) of about 10 min at room temperature (~25°C). Silica-gel forms a porous film on the TP90 surface allowing enzyme, electrolytic solution, electrode interaction

Potentiostatic Polarization Curve to Evaluate the Catalytic Layer of the Liquid Electrolyte Cathode

The performance of the cathode was tested by chronoamperometry, controlled potentials were applied while the current was measured. The potentials were applied in 300 seconds intervals to allow the system to approach steady state before a new potential was applied. The potentials applied were as follow: 0.55V, 0.525V, 0.5V, 0.45V, 0.4V, 0.3V, 0.2V, 0.1V and 0V. The measurements were taken while oxygen was supplied to

the electrolytic cell, saturated solution. The cell contained 10 ml of 0.14 M NaCl, 0.1M PB solution at pH 7.41. Subsequently, the steady state currents were recorded, and plotted against their respective potentials (Figure 4.14). Later, these currents were applied to perform chronopotentiometric measurements.

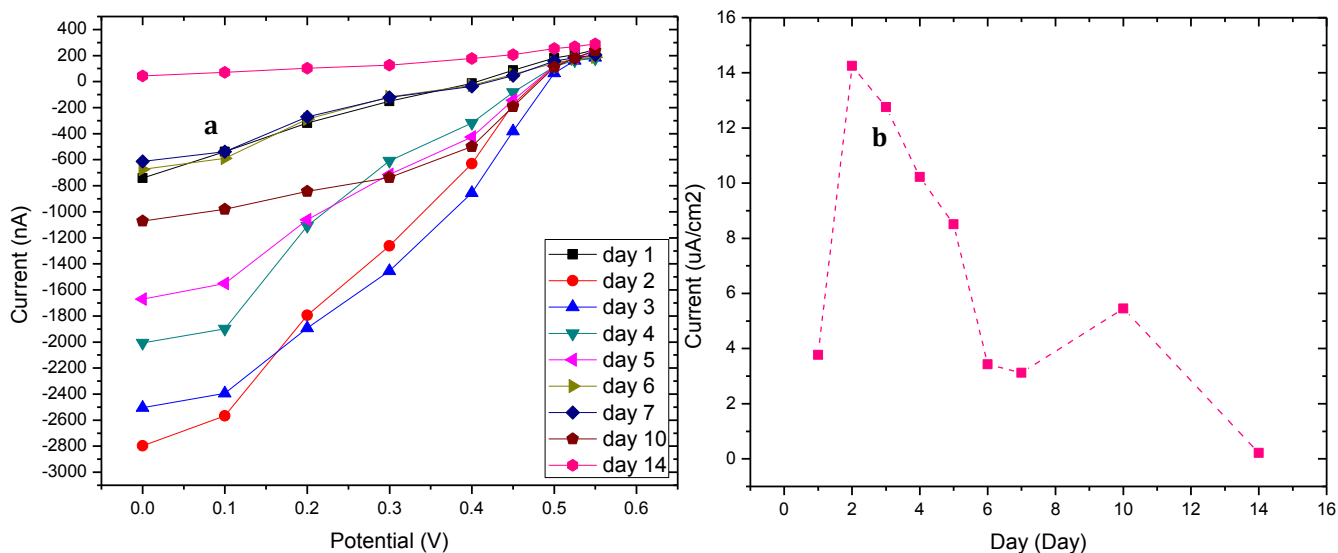


Figure 4.14. a) Potentiostatic Polarization Curve for TP90/BOx/SilicaGel cathode, 0.14 NaCl, 0.1M PB pH 7.41, b) Stabilization Curve at 0V.

Galvanostatic Polarization Curve Evaluate the Catalytic Layer of the Liquid Electrolyte Cathode

The activity of the enzyme was tested in galvanostatic mode. The currents recorded by chronoamperometry were used in this test. Controlled currents were applied while the potential measurements were recorded. Oxygen was actively supplied to the cell as well. The cell contained 10 ml of 0.14 M NaCl, 0.1M PB buffer solution at pH 7.41. Then, the potentials measured were plotted against their respective currents for farther analysis (Figure 4.15).

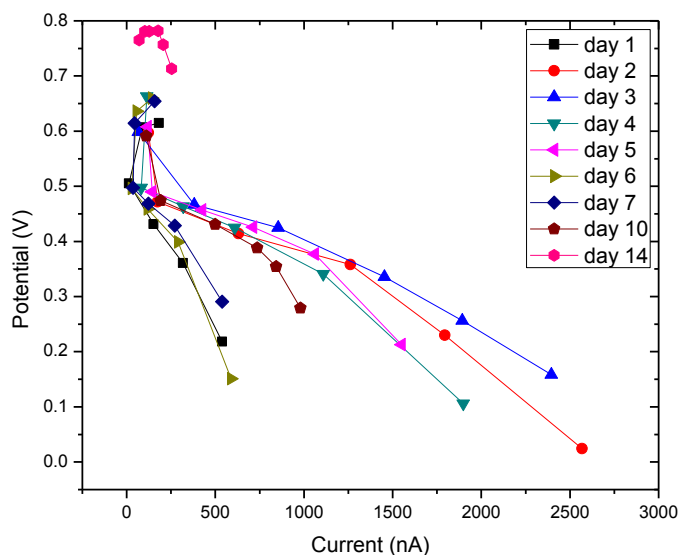


Figure 4.15. Galvanostatic Polarization Curve for TP90/BOx/SilicaGel cathode, 0.14 NaCl, 0.1M PB pH 7.41 (changed axis)

4.2.2. Results and Discussion of the Performance of the Liquid Electrolytic Cathode

Resistivity, Wettability and SEM imaging of “Toray” Papers

The resistivity of the material showed to be very small. The TP90 material without treatment was very hydrophobic but further treatment with IPA allow the material to be hydrophilic enough to allow deposition of the enzyme solution on it. By SEM imaging, the surface of the material is found to be very porous and have high surface area. Also, the images demonstrate the carbon fibers of around 8-10 μm of diameter and are joined together by a Teflon film (Figure 4.11).

After the TMOS precursor formed a silica-gel matrix for enzyme immobilization, SEM images were taken. The images show the TP90 surface, the carbon fibers, are covered by a very porous silica-gel film (Figure 4.13).

After enzyme immobilization by CVD of silica-gel the surface of the material shows to have a thin but porous film deposited. The porosity of the TP90/BOx/Silica-gel

may allow enzyme-electrode-electrolytic solution interaction; thus, oxygen and hydrogen protons (in solution) would approach the active site of the enzyme and the flux of electrons will proceed to reaction.

Potentiostatic Polarization Curve to Evaluate the Catalytic Layer of the Liquid Electrolyte Cathode

The chronoamperometric measurements were taken daily for a week, then at the 10th and 14th days (Figure 4.14.a). These results show the enzyme decreased its activity the first days with decreasing voltage (from 0.55V to 0V). The current density at 0.55V was approximately the same value ~ 200-250 nA for all the measures taken. In the second day, the current density decreased, but this changed in the posterior measurements as the currents increased approaching values similarly to the ones recorded during the first day, when the enzyme was assumed to be most active. After the 3rd day, the curves moves toward the values taken in the first day, ~ -2.45μA at 0V for the 3rd day and ~ -600nA for the 7th day at 0V; being this last value close to the current density registered the day 1. The measures taken at the day 14 show to be very small for any potential in the range of 0.55 V to 0V (pink line in figure 4.14.a). The stabilization curve, where the current measured at 0V is plotted against the unit time (days), shows that the enzyme is working better between day 2 and day 5. Day 10 shows also the cathode has satisfactory performance. This change in the stabilization curve may be due to the enzyme stabilization, the enzyme takes a time to get stabilized into the matrix since this matrix is not fully formed. After the 10th day, the curve shows decreasing in current density that may be due to the inaccessibility of the electron and substrate to the active site of the enzyme. The silica-gel is fully conformed and does not allow the oxygen reduction to

happen. More experiments should be performed to analyze the behavior after day 14th. Additionally, other non-electrochemical test such as circular dichroism spectroscopy.

Analyzing the experimental polarization curves to the theoretical polarization curve (Figure 1.2), we can see that the performance of the electrode is more affected by the activation losses than the ohmic and mass transport losses. From the second to the 10th day, the polarization curves show relatively small ohmic and mass transport losses with compared to day 14. It is assumed that the enzyme acquired its ideal 3-D structural conformation with an active site extremely active toward the ORR. Respect to this fact, the bulk silica-gel formation was reported to be completed after 14 to 21 days of resting in a closed CVD chamber at room temperature, as found in previous studies [77]. The reaction must take place in a humid environment since H₂O is a reactant for this process. The silica-gel formation ends when H₂O evaporates or the TMOS precursor is consumed. This process is accelerated when electrolytes are present in the solution where TMOS is polymerizing. Here, we have to consider that the sample is preserved in the physiological solution to avoid the enzyme to dry and to denaturalize. Thus, it could be assumed that the enzyme gets its ideal 3-D structure when the silica-gel matrix is completely formed and that this took more or less 10 days. This matrix may make inaccessible the active of the enzyme; then, no reaction happens.

From the potentiostatic polarization curve, the ohmic and mass transport losses are shown to be small within a week of measurements. These results suggest that active site-electrolytic solution- electrode interaction is very efficient during the 2nd day and 5th day. The enzyme shows activity toward the ORR until the 10th day. Also, this data show

that a long lifetime electrode for enzymatic, microbial or mitochondrial biofuel cell could be created by optimizing this silica-gel immobilization technique.

Galvanostatic Polarization Curve Evaluate the Catalytic Layer of the Liquid Electrolyte Cathode

Chronopotentiometric measurements were taken to evaluate the cathode behavior in galvanostatic mode. For this, controlled constant currents were applied and their respective potentials were monitored. The behavior of the cathode demonstrated to successfully approach potentials close to 0.72 V-0.78 V for a current range of 50 nA-350 nA at the 14th day of enzyme entrapment. These potentials, at the 14th day, were higher than the potentials registered during the previous measurements, around 0.6 V-0.65 V for a similar current density range (50 nA-250 nA) (Figure 4.15). Between day 2 and 10 the current densities are in the range of 600 nA and 2.7 mA for the potential range given above. Activation losses are present for this cathode design.

Comparing the results from the galvanostatic polarization curves (Figure 4.15) to the potentiostatic polarization curves (Figure 4.14), it is demonstrated that the cathode maybe capable to work at higher potentials than the potential reported previously for BOx. Ivnitski et al reported that T1 copper had a midpoint redox potential approximately to 0.55 V, and T2 and T3 redox potentials had potentials close to 0.217 V and 0.385 V respectively for BOx on screen-printed electrodes. Then, looking to the experimental curves in this research, we can see that the currents found at potentials in the range of 0.55 V to 0 V, the current densities are in the range of 100 nA to 300 nA. When these currents (100 nA- 300nA) were applied to the chronopotentiometry, the potentials ranged

between 0.72 V to 0.78 V. These results demonstrate the redox potential for BOx is \sim 0.75 V on TP90 having BOx entrapped in a silica-gel matrix. Additionally, these results suggest that the BOx enzyme acquires its “close” 3-D conformation near the second week of immobilization. The current densities are lower than in the first week (when it shows highest catalytic activity), the enzyme may be “too” stabilized and the active site “buried” into the shell of the enzyme.

4.2.3. Conclusion on the Performance of the Liquid Electrolyte Cathode Performance

As stated earlier, the results found through this research open new opportunities for electrode designs that consist in the immobilization of the biocatalyst and the creation of a catalytic layer that maintains the 3-D structure of the catalytic site in the enzyme, and the needed electrode-biocatalyst-solution interaction. Herein, the BOx showed to have a redox potential close to 0.75 V on TP90 and at physiological conditions. It was proven that the physiological conditions, NaCl concentration and pH, do not affect the cathode performance, Cl⁻ does not inhibit the enzyme performance. The polarization curves for this cathode design demonstrated low ohmic and concentration (mass transport) losses. The results suggest the electrode-active site and electrolytic solution interaction is successfully accomplished for the first week of enzyme immobilization. Additionally, the electrode had a proven lifetime of about 2 weeks, which is not frequently achieved when the biocatalyst is an enzyme; this is due to the fast denaturalization processes to which the enzyme is subject when taken outside its natural environment.

The enzyme immobilization technique could be adapted for other bioelectrode designs such as air-breathing and liquid electrolyte cathodes or anodes designs. To improve the time active-life of the enzyme, one could work in a new silica-gel design with larger polymer chains (larger functional groups); a balance structure between stability and active site accessibility. The porosity of the polymer could allow the active site to be stable and accessible because the active site is not “buried”. As a result, it could be possible to immobilize enzymes, a cascade of enzymes from biocatalytic path ways for BFCs or solar cell designs, organelles or whole cells as it was reported in research related to pharmaceutical applications. From our point of view, this technology can be used to efficiently engineer the composite nanomaterials and biocalatysts for membraneless BCF electrode designs.

Chapter 5. Conclusions on the Independent Tested Anode and Cathodes

In this research the performance of the anode and the cathode design are not integrating a full biofuel cell. As a consequence, the analysis presented here are independent of each other.

5.1. Bucky Paper-Based Anode Design for the Oxidation of NADH catalyzed by PMG and the L-Malate catalyzed by MDH

The enzyme-based anode tested in this research demonstrates to successfully oxidize NADH to NAD⁺ by PMG catalysis and L-Malate to Oxaloacetate by MDH enzyme in solution. The PMG mediator shows high catalytic activity toward the oxidation of NADH once it is deposited on the bucky paper surface, following the First Law of Fick; the oxidation of NADH is linearly dependent on the concentration of NADH within the range measured (up to 6 mM NADH).

When compared to previous studies, the electrodeposition of the mediator (MG) shows to have a higher charge transferred for the reaction. For the deposition of the mediator monomer, previous studies have shown CVs with oxidation peaks of MG deposition at -0.17 V/cm² with a current of 179 μA/cm² on glassy carbon electrodes (vs. Ag/AgCl) [50]. In this research the electropolymerization peaks appear at + 0.12 V and a current of 0.95 mA (~ 2.47 mA/cm² for an electrode radius of ~3.5mm) is observed; the curve moves toward more positive potentials as the number of cycles increase. The last cycle is found at + 2.2V and a current of 1.2 mA (vs Ag/AgCl) is obtained. The incorporation of the monomer as constituent of the conductive material helps the

polymerization of the monomer by increasing the loading of the catalyst on the electrode surface. The increase in the concentration of the catalyst is observed to be translated as more active sites per unit area, which translates as an increase of the current density through the electrode.

Polarization curves for the analysis of the performance of the PMG toward the oxidation showed to have a higher power output for the PBMG-MG electrode than the BP11-MG electrode. The current density observed at 0.2 V is approximately 25 μA for BP11-MG, (at maximum potential for this electrode) and 100 μA for BPMG-MG, at the same conditions (10mM NADH, 0.2 V). However, through kinetic analysis of the reaction performance, it is possible to observe that both electrodes are mass transport limited since the RDE shows to have better performance while it is spinning at 1600rpm, 225 μA of current density for 0.2 V. These results show we could optimize the anode design to minimize the mass transport losses while increasing the driving force of the substrate toward the anode surface.

The MDH enzyme follows the Michaelis-Menten behavior with no inhibitor affecting its performance in the cell. The enzyme seems to have better interaction with the electrode and the substrate compared to glassy-carbon electrodes studied in previous work. Studies have reported a maximum current density of 1.55 $\mu\text{A}/\text{cm}^2$ for a potential of 0.1V at a concentration of L-Malate of 700 mM in the cell [50]. This research presents a maximum current density of 8.6 μA for BP11-MG ($\sim 22.35 \mu\text{A}/\text{cm}^2$ for an electrode radius $\sim 3.5\text{mm}$) and 7.4 μA ($19.23 \mu\text{A}/\text{cm}^2$ for the same electrode radius) for BPMG-MG anodes 160 mM of L-Malate concentration (at 0.1V also). Thus, it is clear that the performance of the anodes presented here showed successful oxidation of the substrate L-

Malate by the MDH dehydrogenase. This is possible due to the availability of the NAD⁺ (through catalysis by PMG) in solution and due to the enzyme, substrate and surface electrode interaction.

However, this study had presented the half biofuel cell performance of a unique enzyme in solution. By immobilizing the enzyme on the electrode surface, the performance and stability of the enzyme could be improved; highly efficient electrode-active site- substrate interactions can be approached.

5.2. Multicopper Oxidases- based Cathodes for the O₂ Reduction to H₂O

A second phase of this research was focused on the development for enzyme-based cathodes. The performances of two different designs of cathodes were presented in this paper. One design was an air-breathing cathode; in the other cathode, oxygen was actively supplied to the half cell at physiological conditions. The first cathode design was thought to be applied in a portable device while the second one was thought to be applied in an implantable device. In this part of the research the main objective was to work in cathode designs that would satisfy the requirements stated above.

5.2.1. Buckeye and Toray Paper- Based Air-Breathing Cathodes for ORR catalyzed by Laccase

In the air-breathing cathode the prevailing task was finding conductive materials to be utilized in the cathode design that would allow passive oxygen supply to feed the ORR. Laccase from *Trametes versicolor* was the enzyme chosen and PBSE was employed as the linking agent. TP30 was used as the material in the air-breathing layer

and BEP (a MWNTs-based paper) as the catalytic-layer material. The BEP was chosen because it was expected to have high non-covalent (π -stacking) interaction with the linking agent. In the TP30/BEP/PBSE/Laccase cathode, the oxygen was demonstrated to be more successfully supplied by the hydrophobic layer when compared to the Ni/XC50/BEP/PBSE/Laccase setup. The OCV for TP30/BEP/PBSE/Laccase was 0.66 V and the corresponding OCV for the Ni/XC50/BEP/PBSE/Laccase cathode was 0.62 V for the same operating conditions. The CVs show the TP30/BEP/PBSE/Laccase cathode having a larger charge transferred through the material. The width of the TP30/BEP/PBSE/Laccase CV graph shows an order of magnitude of difference, putting in disadvantage the Ni/XC50/BEP/PBSE/Laccase, due to lower current densities transferred.

5.2.2. Toray Paper-Based Cathode for ORR Catalyzed by Bilirubin Oxidase

The liquid electrolyte cathode, an non-breathing mode cathode, was designed to meet implantable device requirements. For this, the BOx enzyme was utilized due to its capability of working at nearly neutral pH and in presence of Cl⁻. Since the cathode is planned to be applied in an implantable device, it has to work at pH 7.41 and in solution of 0.14 NaCl, 0.1 M PB buffer. The design consisted of enzyme entrapment in a silica-gel matrix which was successfully accomplished since the enzyme showed to be working at up to 10 days of initiated the process and by SEM imaging. The silica-gel film looks porous and thin enough to allow electrode-active site-electrolyte solution interactions. Moreover, the potentiostatic polarization curves show higher activity during the first week; fact that may be due to the process of silica-gel formation, which was reported to

be optimally finished after the 2nd and 3rd week but accelerated when electrolytes are present. The most notorious aspect in this part of the research is that BOx shows to have a redox potential of ~0.75 V vs. Ag/AgCl (at day 14) at very low current densities (close to zero current), which is higher than reported in previous works (~0.55 V (vs Ag/AgCl) in carbon-printed electrodes). The current densities were low for day 14 when compared to other measurements in previous days. During days 2 to 10, the potentiostatic polarization curve shows low ohmic and mass transport losses; the current density ranges of 600nA to 3mA between the potential range of 0V and 0.55 V. In the galvanostatic curves, the enzyme shows good activity toward ORR until the day 10 where effects of the activation losses are noted. This shows the enzyme acquired its 3-D conformation by molding itself into the silica-gel matrix in about a week.

The material chosen for the last cathode design provides high porosity and surface area increasing enzyme loading and enzyme-electrode interactions. Additionally, the silica-gel formation was successfully designed to form a very thin film so that it does not interrupt the electrode-enzyme communication. This was demonstrated the first 10 days of the experiments.

This research opens the door to new possibilities in electrode designs for biofuel cells as well as solar cells since chloroplast immobilization could be possible. The designs can be further improved by combination of the properties of composite nanomaterials and enzyme silica-gel entrapment. As an example, MDH dehydrogenase could be immobilized by silica-gel entrapment on the bucky paper-based anode, after PMG is electropolymerized. This would assure better enzyme-electrode interaction than

enzyme in solution. The utilization of BOx in a silica-gel matrix could be also successful for air-breathing cathodes in the near future.

The composite nanomaterials studied here demonstrate to have high qualities for electrode design while working with enzymes. BP11 and BPMG are highly recommended to be used in posterior anode designs since they showed to be better conductive materials for PMG for NADH and L-Malate oxidation. It is highly encouraged the use of these materials for the immobilization of a cascade of enzymes, such as those existing in the Krebs cycle, to test for complete oxidation of pyruvate in this case, or other biofuel with the respective needed enzymes. TP30 showed to perform very well as hydrophobic layer for air-breathing cathodes. The high conductivity and manageability of the BEP is also a factor to take into account when designing and assembling a cathode using silica gel- entrapment and BOx for ORR.

References

1. Minteer, S.D.; Liaw, B.Y.; Cooney, M.J. *Current Opinions in Biotechnology* **2007**, *18*, 228.
2. Atanassov, P.; Apblett, C.; Banta, S.; Brozik, S.; Barton, S.C.; Cooney, M. J.; Liaw, B. Y.; Mukerjee, S.; Minteer, S. D. *Electrochem. Soc. Interf.* **2007**, *16*, 28.
3. Willner, I; Yan, Y.-M.; Willner, B.; Tel-Vered, R. *Fuel Cells*, **2009**, *1*, 7.
4. Biffinger, J. C.; Pietron, J.; Ray, R.; Little, B.; Ringeisen, B. R. *Biosens Bioelectron* **2007**, *22*, 1672.
5. Arechederra, R.; Minteer, S.D. *Electrochimica Acta*, **2008**, *53*, 6698.
6. Arechederra, R.; Boehm, K.; Minteer, S.D. *Electrochimica Acta*, **2009**, *54*, 7268.
7. Bhatnagar, D.; Xu, S.; Fischer, C.; Arechederra, R.L.; Minteer, S.D. *Phys. Chem. Chem. Phys.* **2011**, *13*, 86.
8. Wang, C.; Nehrir, M. H.; Shaw, S.R. *IEEE Trans. on Energy Conversion.* **2005**, *20*, 442.
9. Calabrese Barton, C.; Gallaway, J.; Atanassov, P. *Chem. Rev.* **2004**, *104*, 4867.
10. Ribeiro, E. S.; Rosatto, S. S.; Gushikem, Y.; Kubota, L. T. *J Solid State Electrochem.* **2003**, *7*, 665.
11. Yu, E. H.; Scott, K. *Energies*, **2010**, *3*, 23.
12. Heller, A. *J. Phys. Chem.* **1992**, *96*, 3579.
13. Sokic-Lazic, D.; Minteer, S.D. *Electrochem and Solid State Lett.* **2009**, *12*, F26.
14. Sokic-Lazic, D.; Minteer, S. D. *Biosens. Bioelectron.* **2008**, *24*, 939.
15. Sokic-Lazic, D.; Arechederra, R. L.; Treu, B. L.; Minteer, S. D. *Electroanal.* **2010**, *22*, 757.
16. Gorton, L.; Hale, P. D.; Persson, B.; Boguslavsky, L. I.; Karan, H. I.; Lee, H. S.; Skotheim, T. A.; Lan, H. L.; Okamoto, Y. *ACS Symp. Ser.* **1992**, *487*, 56.
17. Blaedel, W. J.; Haas, R. G. *Anal. Chem.* **1970**, *42*, 918.
18. Leduc, P.; Thévenot, D. *Bioelectrochem. Bioenerg.* **1974**, *1*, 96.
19. Blaedel, W. J.; Jenkins, R. A. *Anal. Chem.* **1975**, *47*, 1337.
20. Moiroux, J.; Elving, P. J. *J. Am. Chem. Soc.* **1980**, *102*, 6533.
21. Jaegfeldt, H. J. *Electroanal. Chem.* **1980**, *110*, 295.

22. Elving, P. J.; Bresnahan, W. T.; Moiroux, J.; Samec, Z. *Bioelectrochem. Bioenerg.* **1982**, *9*, 365.
23. Blankespoor, R. L.; Miller, L. L. *J. Electroanal. Chem.* **1984**, *171*, 231.
24. Jaegfeldt, H. J. *J. Electroanal. Chem.* **1980**, *110*, 295.
25. Zhou, D.; Fang, H-Q.; Chen, H-Y; Ju, H-X.; Wang, Y. *Analytica Chimica Acta.* **1996**, *329*, 41.
26. Karyakin, A. A.; Karyakina, E. E.; Schuhmann, W.; Schmidt, H. L. *Electroanal.* **1999**, *11*, 553.
27. Karyakin, A.; Karyakina, E. E.; Schmidt, H. L. *Electroanalysis* **1999**, *11*, 149.
28. Svoboda, V.; Cooney, M. J.; Rippoliz, C.; Liaw, B. Y. *J. Electrochem. Soc.* **2007**, *154* (3), D113.
29. Gorton, L.; Bartlett, P. N., NAD(P)-Based Biosensors. In *Bioelectrochemistry: fundamentals, experimental techniques, and applications*, Bartlett, P. N., Ed. John Wiley & Sons, Inc.: Chichester, **2008**, 157-198.
30. Blaedel, W. J.; Haas, R. G. *Anal.Chem.* **1970**, *42*, 918.
31. Leduc, P.; Thévenot, D. *Bioelectrochem. Bioenerg.* **1974**, *1*, 96.
32. Moiroux, J.; Elving, P. J. *J. Am. Chem. Soc.* **1980**, *102*, 653.
33. Elving, P. J.; Bresnahan, W. T.; Moiroux, J.; Samec, Z. *Bioelectrochem. Bioenerg.* **1982**, *9*, 365.
34. Blankespoor, R. L.; Miller, L. L., *J. Electroanal. Chem.* **1984**, *171*, 231.
35. Ludvik, J.; Volke, J., *Anal. Chim. Acta* **1988**, *209*, 69.
36. Barlet, P.N. (2008) Bioenergenics and Biological Electron Transport. In Barlet, P.N. (Ed), *Bioelectrochemistry: Fundamentals, Experimental Techniques and Applications(1-37)*. Chichester: John Wiley & Sons.
37. Gorton, L. *J. Chem. Soc., Faraday Trans. 1 F* **1986**, *82*, 1245.
38. Gorton, L.; Csöregi, E.; Domínguez, E.; Emnéus, J.; Jönsson-Pettersson, G.;
39. Marko-Varga, G.; Persson, B. *Anal. Chim. Acta* **1991**, *250*, 203.
40. Bartlett, P. N.; Tebbutt, P.; Whitaker, R. G. *Prog. React. Kinet.* **1991**, *1*, 55.
41. Katakis, I.; Domínguez, E., Catalytic electrooxidation of NADH for
42. dehydrogenase amperometric biosensors. *Microchim. Acta* **1997**, *126* (1), 11-32.
43. Lobo, M. J.; Miranda, A. J.; Tuñón, P. *Electroanal.* **1997**, *9*, 191.

44. Lorenzo, E.; Pariente, F.; Hernández, L.; Tobalina, F.; Darder, M.; Wu, Q.; Maskus, M.; Abruña, H. D. *Biosens. Bioelectron.* **1998**, *13*, 319.
45. Gorton, L.; Domínguez, E. *Rev. Mol. Biotechnol.* **2002**, *82*, 371.
46. Dai, Z. H.; Liu, F. X.; Lu, G. F.; Bao, J. C. *J. Solid State Electrochem.* **2008**, *12* (2), 175.
47. Tse, D.C.-S.; Kuwana, T. *Anal. Chem.*, **1978**, *50*, 1315.
48. Ribeiro, E. S.; Rosatto, S. S.; Gushikem, Y.; Kubota, L. T. *J Solid State Electrochem.* **2003**, *7*, 665.
49. Pessoa, C. A.; Gushikem, Y.; Kubota, L. T.; Gorton, L.; *J. Electroanal. Chem.* **1997**, *431*, 23.
50. Rincón, R.A.; Artyushkova, K.; Mojica, M.; Germain, M.N.; Minter, S.D.; Atanassova, P. *Electroanalysis.* **2010**, *22*, 799.
51. Mano, N.; Mao, F.; Heller, A. *J. Am. Chem. Soc.*, **2003**, *125*, 6588.
52. Calabrese Barton, S.; Pickard, M.; Vazquez-Duhalt, R.; Heller, A. *Biosens. Bioelectron.*, **2002**, *17*, 1071.
53. Tarasevich, M.R.; Bogdanovskaya, V.A.; Zagudaeva, N.M.; Kapustin, A.V. *Russian J. Electrochem.*, **2002**, *38*, 335.
54. Farneth, W.E.; D'Amore, M.B. *J. of Electroanalyt. Chem.* 2005, *581*, 197.
55. Barton, C.B.; Kim, H.-H.; Binyamin, G.; Zhang, Y.; Heller, A. *J. Am. Chem. Soc.* **2001**, *123*, 5802.
56. Pardo-Yissar, V.; Katz, E.; Willner, I.; Kotlyar, A. B.; Sanders, C.; Lill, H. *Faraday Discuss.* **2000**, *116*, 119.
57. Smolander, M.; Boer, H.; Valkiainen, M.; Roozemaana, R.; Bergelin, M.; Eriksson, J.-E.; Zhang, X.-C.; Koivula, A.; Viikari, L. *Enz. and Microb. Tech.* **2008**, *43*, 93.
58. Guiseppi-Elie, A.; Lei, C.; Baughman, R.H. *Nanotechnology.* **2002**, *13*, 559.
59. Shleev, S.; Jarosz-Wilkolazka, A.; Khalunina, A.; Morozova, O.; Yaropolov, A.; Ruzgas, T.; Gorton, L. *Bioelectrochemistry* **2005**, *67*, 115.
60. Vincent, K.A.; Cracknell, J.A.; Lenz, O.; Zebger, I.; Friedrich, B.; Armstrong, F.A. *Proc. Natl. Acad. Sci. U.S.A.* **2005**, *102*, 16951.
61. Ivniński, D.; Artyushkova, K.; Atanassov, P. *Bioelectrochemistry*, **2008**, *74*, 101.

62. Ivnitski, D.; Artyushkova, K.; Rincón, R. A.; Atanassov, P.; Luckarift, H. R.; Johnson, G. R. *Small*, **2008**, *4*, 357.
63. Gupta, G.; Rajendran, V.; Atanassov, P. *Electroanalysis*, **2003**, *15*, 1577.
64. Gupta, G.; Rajendran, V.; Atanassov, P. *Electroanalysis* **2004**, *16*, 1182.
65. Ivnitski, D.; Atanassov, P. *Electroanalysis*, **2007**, *19*, 2307.
66. Ivnitski, D.M.; Khripin, C.; Luckaift, H.R.; Johnson, G. R.; Atanassov, P. *Electrochimica Acta*. **2010**, *55*, 7385.
67. Wen, D.; Xuab, X.; Dong, S. *Energy Environ. Sci.* **2011**, DOI: 10.1039/c0ee00080a
68. Cole, J.L.; Tan, G. O.; Yang, E. k.; Hodgson, K.O.; Solomon, E. I. *J. Am. Chem. Soc.* **1990**, *112*, 2243.
69. Shleev, S.; Tkac, J.; Christenson, A.; Ruzgas, T.; Yaropolov, A.I.; Whittaker, J.W.; Gorton, L. *Biosens. And Bioelect.* **2005**, *20*, 2517.
70. Ivnitski, D.M.; Luckaift, H.R.; Ramasamy, R.; Artyushkova, K.; de la Iglesia, P.; Khripin, C. Apblet, C.; Johnson, G. R.; Atanassov, P. *Prep.Pap.-Am. Che. Soc. Div. Fuel. Chem.* **2009**, *54*, xx
71. Fernandez-Sanchez, C.; Tzanov, T.; Gubitz, G.M.; Cavaco-Paulo, A. *Bioelectrochemistry*. **2002**, *58*, 149.
72. Willner, I.; Katz, E; Patolsky, F. ; Buckmann A.F. *J Chem Soc, Perkin Transact 2, Phys Org Chem* **1981**, 817.
73. Katz, E.; Filanovsky, B.; Willner, I. *New J Chem*, **1999**, *23*, 481.
74. Mano, N.; Mao, F.; Heller, A. *J Am Chem Soc.* **2002**, *124*, 12962.
75. Moore, C.M.; Akers, N.L.; Hill A.D.; Johnson, Z.C.; Minteer, S.D. I. *Biomacromolec.* **2004**, *5*, 1241.
76. Chen, R.J.; Zhang, Y.; Wang, D; Dai, H. *J. Am. Chem. Soc.* **2001**, *123*, 3838.
77. Dunn, B.; Miller, J. M.; Dave, B. C.; Valentine, J. S.; Zink, J. I. *Acta Mater.* **1998**, *46*, 737.
78. Gupta, G; Rathod, S.B.; Staggs, K.W. ; Ista, L.K.; Oucherif, K.A.; Atanassov, P. ; Tartis, M.S.; Montañó, G.A.; López, G.P. *Langmuir*. **2009**, *25*, 13322.
79. Dai H. *Acc. Chem. Res.* **2002**, *35*, 1035.

80. Ivnitski, D.; Branch, B.; Atanassov, P.; Apablett, C. *Electrochem. Commun.* **2007**, *8*, 1204.
81. Yan, Y.; Zheng, W.; Su, L.; Mao, L. *Adv. Mater.* **2006**, *18*, 2639.
82. Yan, J.; Zhou, H.; Yu, P.; Su, L.; Mao, L. *Adv. Mater.* **2008**, *20*, 2899.
83. Li, X.; Zhou, H.; Yu, P.; Su, L.; Ohsaka T.; Mao L. *Electrochem. Communications* **2008**, *10*, 851.
84. Vichchulada, P.; Zhang, Q.; Duncan, A.; Lay, M.D. *App. Mat. And Interf.* **2010**, *2*, 467.
85. Dai, H.; Kong, J.; Zhou, C.; Franklin, N.; Tomblor, T.; Cassel, A.; Fan, S.; Chapline, M. *J. Phys. Chem.* **1999**, *103*, 11246.
86. Zhao, Z.; Gou, J.; Khan, A. *J. of Nanoscience* **2009**.
87. Wang, D.; Chen, L. *Nano Letters*, **2007**, *7*, 1480.
88. Seunghun, H.; Myung, S. *Nature Nanotech.* **2007**, *2*, 207.
89. Toray Industries Inc. *Toray Carbon Fiber Paper. Specifications "TPG-H"*.
90. Gou, J.; Liang, Z.; Wang, B. *Internat. J. of Nanoscience* **2004**, *3*, 293.
91. Gou J. *Polymer Internat.* **2006**, *55*, 1283.
92. Zhao, Z.; Gou, J.; Khan, A. *J. of Nanoscience* **2009**.
93. Penner, R. M. *J. Phys. Chem. B* **2002**, *106* (13), 3339.
94. Moehlenbrock, M.J.; Arechederra, R.L.; Sjöholm, K.H.; Minteer, S.D. *Anal. Chem.*, **2009**, *81*, 9538.
95. Gorton, L.; Domínguez, E., Electrochemistry of NAD(P)⁺/NAD(P)H. In *Bioelectrochemistry*, Bard, A. J.; Stratmann, M.; Wilson, G. S., Eds. Wiley-VHC: Weinheim, **2002**; Vol. 9, pp 67-143.
96. Svoboda, V.; Cooney, M.; Liaw, B. Y.; Minteer, S.; Piles, E.; Lehnert, D.; Barton, S. C.; Rincon, R.; Atanassov, P. *Electroanal.* **2008**, *20* (10), 1099.
97. Yan, Y.; Zheng, W.; Su, L.; Mao, L. *Adv. Mater.* **2006**, *18*, 2639.
98. Lau, C.; Atanassov, P.; Svoboda, V.; Singhal, S. *217th ECS Meeting*, **2009**, Abstract #441.
99. Barriere, F.; Kavanagh, P.; Leech, D. *Electrochimica Acta.* **2006**, *51*, 5187.
100. Penner, R. M. *J. Phys. Chem. B* **2002**, *106* (13), 3339.

101. Moehlenbrock, M.J.; Arechederra, R.L.; Sjöholm, K.H.; Minter, S.D. *Anal. Chem.*, **2009**, *81*, 9538.
102. Wedding, R.T.; Black, M.K.; Pap, D. *Plant Physiol.* **1976**, *58*, 740.